Theses and Dissertations

2015

Convective Assembly of Colloidal Monolayers: Mechanical and Chemical Approaches

Tanyakorn Muangnapoh
Lehigh University

Follow this and additional works at: http://preserve.lehigh.edu/etd

Part of the Chemical Engineering Commons

Convective Assembly of Colloidal Monolayers: Mechanical and Chemical Approaches

by

Tanyakorn Muangnapoh

Presented to the Graduate and Research Committee
of Lehigh University
in Candidacy for the Degree of
Doctor of Philosophy
in
Chemical Engineering

Lehigh University
May 2015

ii

Certificate of Approval

Approved and recommended for acceptance as a dissertation in partial fulfillment of the requirements of the degree of Doctor of Philosophy.

_____
Date

_____
James F. Gilchrist, Ph.D.
Dissertation Advisor

_____
Accepted Date

Committee Members:

_____
James F. Gilchrist, Ph.D.
Committee Chair

_____
Manoj K. Chaudhury, Ph.D.
Committee Member

_____
Raymond A. Pearson, Ph.D.
Committee Member

_____
Mark A. Snyder, Ph.D.
Committee Member

iii

Acknowledgements

First of all, I would like to express my deepest gratitude to my advisor, Professor James Gilchrist for his kind supervision, valuable discussion and warmest encouragement throughout my PhD study. He once mentioned that "the actual product of PhD study is the student not the research". He constantly encourages all students in the group to be creative, collaborative, and hard-working. I have learned a lot from him. Thank you very much. Also, I would like to thank Royal Thai government, the Department of Chemical and Biomolecular Engineering at Lehigh University, and all committee members: Professors Manoj Chaudhury, Raymond Pearson, Mark Snyder and Andrew Klein.

Special thanks go to Dr. Pisist Kumnorkaew and Dr. Alex Weldon who trained and helped me understand basic principles of convective deposition when I started my research. Moreover, I would like to thank Midhun Joy who works with me on making (100) fcc thin film colloidal crystals (Chapter 3) and MgO membranes (Chapter 6) as well as Kedar Joshi and Michael Stever who work with me on NaOH and EtOH projects (Chapter 4 and 5). This dissertation will not be possible without them. Big thanks go to all my lab mates, Dr. Bu Xu, Dr. Tharanga Perera, Dr. Eric Daniels, Dr. Xue Li and Naval Singh for their useful discussion, encouragement and friendship. Besides, I would like to acknowledge the Chaudhury lab, Snyder lab, Tansu lab, Cheng lab and McHugh lab for their help in this research.

Finally, I would like to thank my family, friends and girlfriend Chonchanok Theethakaew for their endless support and understanding.

iv

Table of Contents

List of Tables

viii

xiv

Abstract

The assembly of colloidal particles has drawn great attention due to its fascinating impact on various applications. One simple but effective method for the deposition of well-ordered particles microstructure is convective deposition. Convective deposition translates a meniscus of particle suspension across a substrate leaving behind a thin film. As the liquid phase of the suspension evaporates, primarily from the thin film, particles are deposited and order through capillary interactions. In this thesis, we develop novel techniques for enhancing the microstructure of evaporation-driven convective deposition. Confocal laser scanning microscopy and image analysis are used for quantifying the quality of deposited particle microstructure through number of nearest neighbors, packing density, and local bond order.

We have developed vibration-assisted convective deposition as an advanced technique for improving convective deposition. The original motivation for this work was to investigate how environmental disturbances would affect a deposition process in an industrial scale. With the application of lateral vibration of the substrate, drastic alterations of the interfacial liquid surface and the evaporation rate occur. Aqueous binary suspensions of colloidal microspheres and nanoparticles were used for studying effect of the amplitudes (0-250 μm) and the frequencies (0-50 Hz) of substrate vibration. This effect yields the unexpected result of opening the range of operating parameters from a single deposition velocity for a given set of conditions to a wide range of velocities that result in monolayer deposition. A large phase space of frequency and amplitude

1

demonstrates a region where at moderate conditions enhancement occurs. At low amplitudes and high frequencies the particles do not organize into well-ordered monolayers and at high amplitudes and low frequencies the substrate motion does not yield long range monolayers because of the pseudo-steady motion of the substrate. It is also noted that this technique can be further extended to fabricate partially aligned (100) fcc thin film colloidal crystals.

In two ways, the solution of the suspension has been manipulated to alter the dynamics of deposition. First, ionic strength of medium and particle surface charges are known as crucial parameters for understanding micro-scale mechanism of particle assembly. The presence of salt reduces the thickness of the electrical double layers (Debye length), which leads to pre-organized deposition and particle island formation. The electrostatic barrier as a function of the distance between particle and substrate as well as the effective separation distance as a function of the salt concentration are calculated using DLVO theory. On the contrary, the addition of NaOH provides additional electrostatic repulsion forces between particle-particle and particle-substrate, which results in the enhancement in particle deposition. Second, Marangoni flow, created by the surface tension gradient within binary liquid mixture of ethyl alcohol and water, offers the great promise in macro-scale defect suppression. Our preliminary results suggests significant enhancement of monolayer deposition at the concentration of ethyl alcohol between 30-50 %V. Droplet evaporation experiments give the detailed ideas of how surface tension-driven flow develops.

Chapter 1

Introduction

1.1 Dissertation Organization

This doctoral thesis presents research of novel techniques for enhancing evaporation-driven convective deposition of particle monolayers from suspension. Starting with fundamental understanding of convective evaporation and capillary force, previous studies on convective deposition is reviewed in Chapter 1. The experimental setup, material preparation and image analysis techniques are described in Chapter 2. Fundamental process enhancements using the application of lateral vibration of the substrate as well as the addition of nanoparticle to enhance microstructure order and packing density are presented in Chapter 3. With the addition of sodium hydroxide (NaOH) and sodium chloride (NaCl), we demonstrate the effect of the ionic strength and surface charge on convective deposition in Chapter 4. Preliminary investigations of Marangoni effect due to the surface tension gradient between water and ethyl alcohol (EtOH) are presented in Chapter 5. Applications and potential studies including areas of interest are discussed in Chapter 6. Finally, summary and future outlook are briefly discussed in Chapter 7.

1.2 Colloidal Self-Assembly

The self-assembly of colloidal particles into thin films has been widely studied due to the fascinating physics involved and the promise of use in applications ranging from photonics (Haes, Haynes, and Van Duyne 2001; Tessier et al. 2001; Im et al. 2002), lithography (Haes, Haynes, and Van Duyne 2001; Haynes and Van Duyne 2001; Zhang et al. 2008), ceramics (Harris et al. 2007), catalysis (Tessier et al. 2000), biocompatible surfaces (Koyama, Yamaguchi, and Miyasaka 1994; Zhang et al. 2005; Wang et al. 2011), sensors (Koyama, Yamaguchi, and Miyasaka 1994; Velev and Kaler 1999; Yi et al. 2006), membranes (Weldon et al. 2012), and fabrication of complex structures such as Janus particles (Pawar and Kretzschmar 2010) and ribbon-like structures (Kim et al. 2010). Typical methods used to fabricate particulate thin films include spin coating (Jiang and McFarland 2005), epitaxy (van Blaaderen et al. 2003; Lee et al. 2004), optical tweezers (Biancaniello and Crocker 2006), electrophoretic particle assembly (Hayward, Saville, and Aksay 2000) and vertical deposition (Dimitrov and Nagayama 1996; Diao et al. 2005; Shimmin, DiMauro, and Braun 2006). However, these methods are all limited, whether it be in their complexity or speed of the process which limits scale-up, difficulty in integrating feedback control, or insufficient control over particle layer characteristics. Convective deposition (Kumnorkaew et al. 2008; Prevo and Velev 2004; Dimitrov and Nagayama 1995; Yamaki, Higo, and Nagayama 1995) provides an alternative because it can be used to easily, inexpensively, and reliably create relatively large, periodically-ordered structures of spherical particles (Stebe, Lewandowski, and Ghosh 2009).

1.2.1 Convective Evaporation and Capillary Force

Convective deposition, the evaporation-driven flow and capillary-driven assembly of colloidal particles on a substrate, essentially combines two recently explained concepts. The first, commonly known as the "coffee ring" effect (Deegan et al. 1997), describes the phenomenon where particles flow to the contact line of a meniscus as a result of the evaporative flux (Figure 1.1). Convective deposition shares similar physics to these evaporating droplets as a suspension droplet is dragged across a substrate. This results in a trailing drawn-out thin film with enhanced evaporation. Particles are drawn into this region from the bulk and then are confined in a 2D thin film where they locally deform the liquid-air interface. Minimizing surface energy, the particles experience strong capillary-driven forces that result in particle-particle and particle-substrate attractive potential (Figure 1.2). The inter-particle interactions (Gifford and Scriven 1971) were recently coined the "cheerio effect" (Vella and Mahadevan 2004). This describes the macroscopic phenomena of particle attractions as a result of interface deflections coming from their contact lines, relative buoyancy, and/or vertical confinement. The inter-particle interactions are strong and pull particles into their maximum packing density within the thin film. Capillary forces are sufficiently strong to overcome particle-particle and substrate-particle electrostatic repulsion and bring particles into contact with each other and the substrate. These same experimental conditions can be used to deposit particle multilayers in the form of a colloidal crystal where the physics of assembly depends on confinement and flow steering (Brewer et al. 2008) as opposed to surface energy.
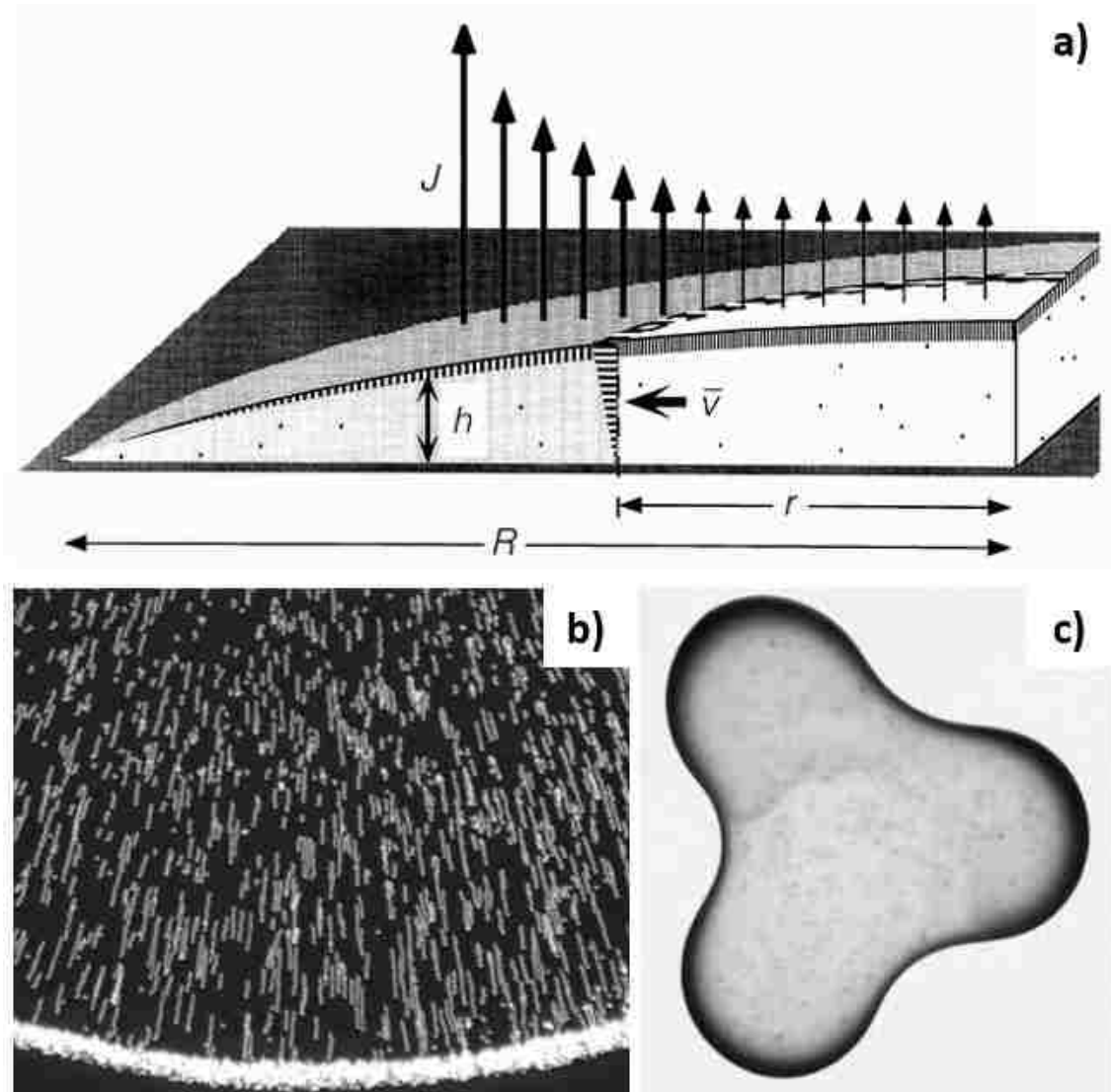
Figure 1.1: Demonstration of the "coffee ring" effect. (a) Diagram showing enhanced evaporation at the edge of a drying droplet. (b) Particles flow to the outside edge of a droplet as a result of enhanced evaporation. (c) 2-cm-diameter drop of coffee with high particle concentration at the outside edge. Reprinted from Deegan et al., 1997.

a)

particle convective flow

evaporation

water convective flow

b)

surface tension
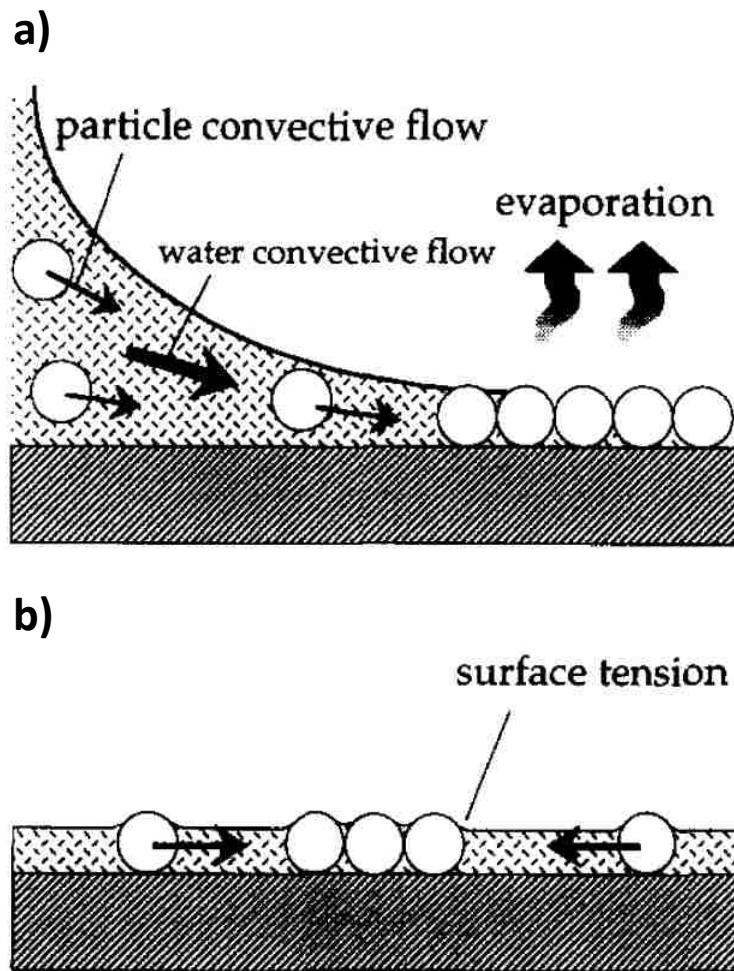
Figure 1.2: Schematic of convective deposition. (a) Particles are carried by water convective flow from meniscus to the particle array where evaporation occurred. (b) Strong capillary interaction due to the deformation of water surface results in 2D particle ordering. Reprinted from Nagayama, 1996.

Although it has been known that the cause of capillary forces is the deformation of the liquid surface owing to the presence of particles, Kralchevsky and Nagayama (1994) classified two different types of capillary forces: flotation and immersion capillary forces (Figure 1.3a) according to the physical location of particles on/in liquid surface. In case of floating particles, the flotation capillary forces originate from the particle weight and Archimedes force. This will not be applicable for particles of radii smaller than 10 μm since the interaction energy of these flotation capillary forces is smaller than thermal energy kT (Figure 1.3b). On the other hand, when particles are partially immersed in a liquid layer, the immersion capillary forces will exist even for 10-nm colloidal particles. The deformation of liquid surface in this case only depends on the wetting properties of the particle surface.
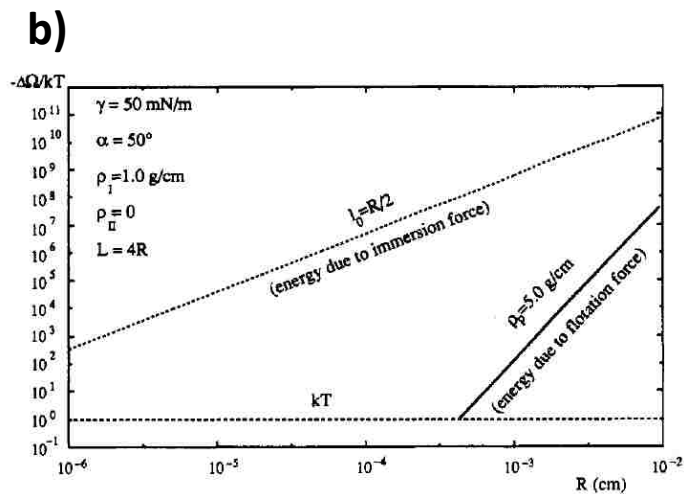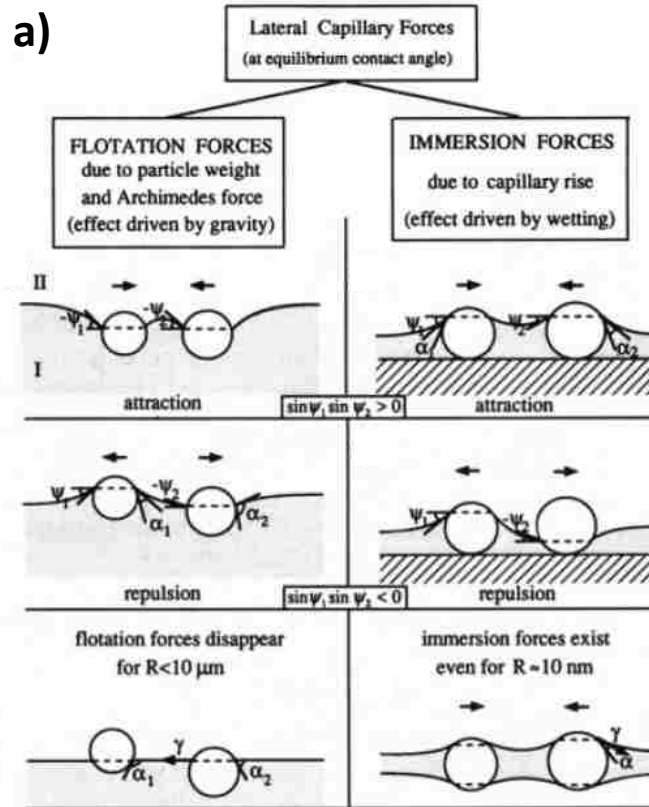
Figure 1.3: Capillary forces. (a) Comparison between the flotation and immersion capillary forces. (b) Immersion capillary forces exists even for 10-nm colloidal particles whereas flotation capillary forces are negligible for colloidal particles smaller than 10 μm. Reprinted from Kralchevsky and Nagayama, 1994.

1.2.2 Convective Deposition

Convective deposition has drawn the great attention of researchers due to its ability to scale up. With a vertical deposition (Dimitrov and Nagayama 1996), the withdraw velocity of 0.1-30 μm/s can be precisely controlled. Later Prevo and Velev developed an operational basis for rapid (up to 212 μm/s), controlled convective deposition of particles with wide size ranges (Prevo and Velev 2004). SEM and optical microscopy results show the microstructure change from a dilute submonolayer (Figure 1.4a) to a locally-ordered submonolayer (Figure 1.4b) to a monolayer (Figure 1.4c) and finally to a multilayer (Figure 1.4d) with decreasing deposition velocity. With fixed particle size, evaporate rate and particle volume fraction, monolayers of particle with hexagonal closed packed structure are obtained only at a single deposition velocity. Exceeding this monolayer deposition velocity results in submonolayer whereas slower deposition velocity leads to multilayer formation. Additionally changing environmental humidity has a minimal effect on the thin films produced. The primary parameters strongly affecting the process outcome are deposition velocity and particle volume fraction.

Previous work on convective deposition includes early work by Dimitrov and Nagayama (1995) who, through a simple material flux balances along with the geometric confinement of particles in a thin film, calculated the withdraw velocity v_d that matches the crystallization velocity v_c.

$$v_c = v_d = \frac{\beta J_e \varphi}{0.605 d (1-\varphi)}$$ (1.1)

10

The withdraw velocity v_d depends on particle volume fraction φ, evaporation flux of liquid J_e, particle size d and a deposition parameter, β. Here, β is a constant value between 0 and 1 that depends on particle-particle and particle-substrate interaction. For low volume fraction and electrostatically stable particles, β approaches 1. The value decreases with increasing particle-substrate interaction.

In addition to Prevo's work, Kumnorkaew et al. (2008) investigated the effects of the blade angle and the hydrophobicity of the deposition blade on the optimal monolayer deposition velocity. Through SEM and Confocal Laser Scanning Microscopy (CLSM), by increasing the deposition blade angle, the particle flux increases due to the change in radius of curvature, resulting in increased deposition velocity to maintain monolayers (Figure 1.5). Using the hydrophilic deposition blade, the monolayer deposition velocity is a weak function of deposition angle; on the contrary, the monolayer deposition velocity shows linear relationship with deposition angle in case of the hydrophobic blade. The transition region between monolayer and multilayer is always in the form of loose-square packed structure.
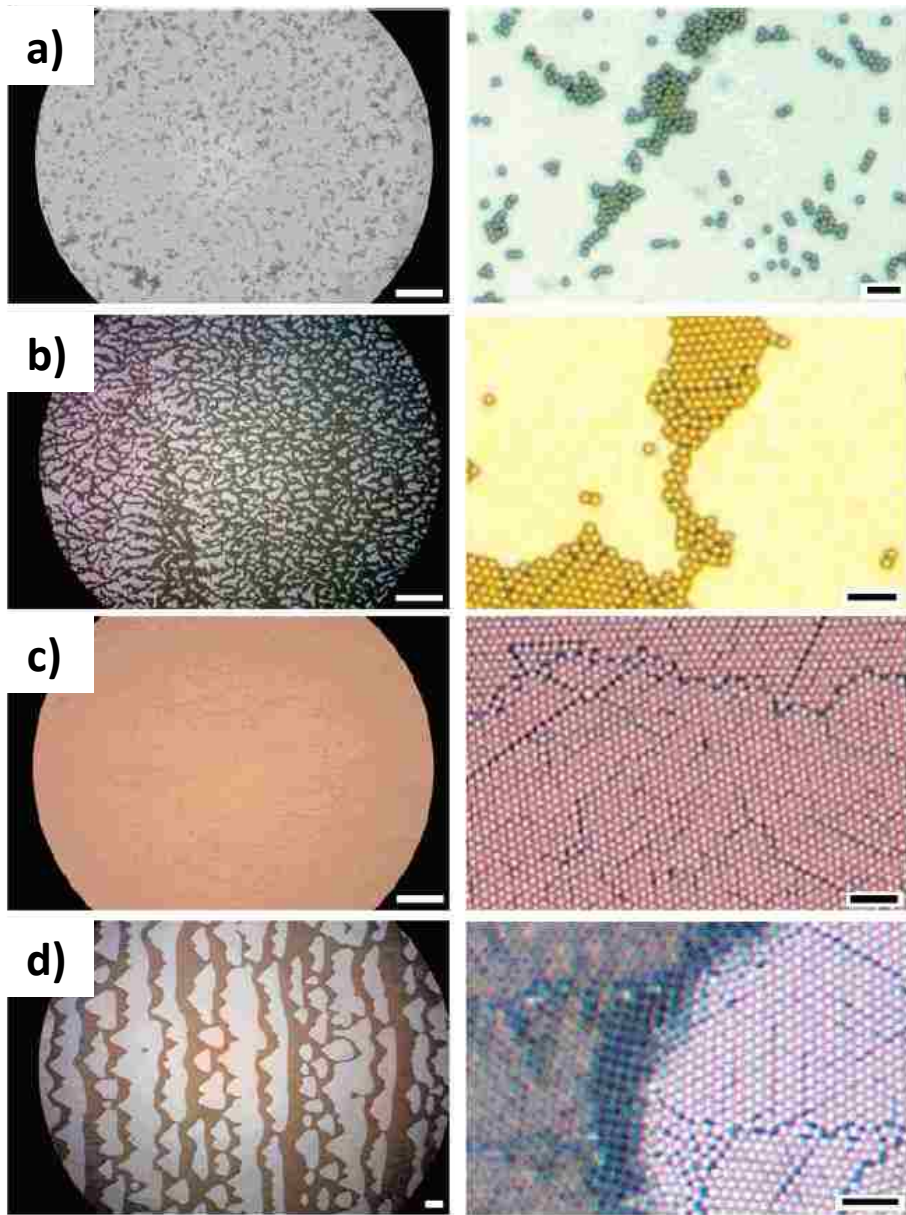
Figure 1.4: Microstructures deposited at decreasing velocities: (a) dilute submonolayer, (b) locally-ordered submonolayer, (c) monolayer, and (d) multilayer. Reprinted from Prevo and Velev, 2004.
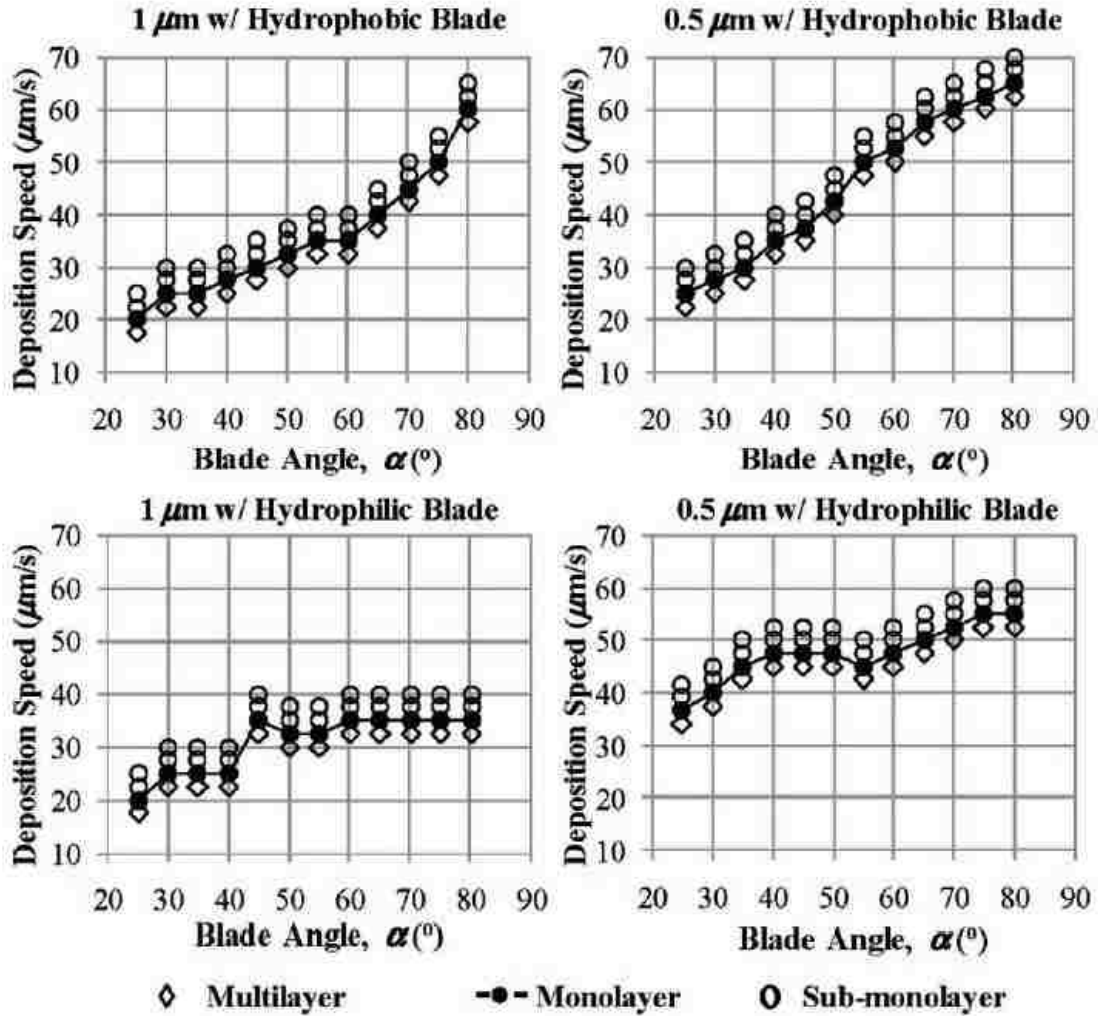
Figure 1.5: Four phase diagrams describe the dependence of the morphology on deposition velocity and blade angle, α for 1.0 and 0.5 μm SiO_2 particle with hydrophobic and hydrophilic blades. Summarizing the results from these phase diagrams, clearly the monolayer deposition velocity strongly depends on blade angle for hydrophobic blades and weakly depends on blade angle for hydrophilic blades. Reprinted from Kumnorkaew et al., 2008.

1.2.3 Convective Deposition of Binary Suspension

The addition of nanoparticles to suspension is a noteworthy enhancement in convective deposition. Not only instabilities and defects are significantly suppressed but also the improvement in particle packing density and extension of coating length are observed (Kumnorkaew and Gilchrist 2009). Using aqueous binary suspensions of 1 μm silica microspheres and 100 nm polystyrene (PS) nanoparticles, the effects of nanoparticle concentration ranging from 0 % to 16 % on the quality of the microsphere deposition was investigated. At low concentrations of nanoparticles, the deposition results in an instability that forms stripes parallel to the receding contact line. Optimum deposition occurs between 6 % and 8 % PS and forms a monolayer having the same high degree of uniformity as the monodisperse suspension is fabricated. For higher concentrations, the deposition is increasingly less uniform as a result of nanoparticle depletion destabilizing the microspheres. By considering relative species flux, the volume fraction ratio of smaller to larger constituents necessary for steady well-ordered deposition are predicted (Kumnorkaew, Weldon, and Gilchrist 2010). Theoretical optimum nanoparticle concentration is equal to 0.32 of microparticle concentration based upon a simple maximum packing argument for these two species.

Chapter 2

Materials and Methods

2.1 Materials Preparation

2.1.1 Suspension Preparation

The primary colloid suspension used in this work is prepared by dispersing silica microspheres (Fuso Chemical Co, Japan) having a density of 2.2 g/cm^3, an average diameter of $2a_{micro} = 1.01 \pm 0.02$ μm, and a zeta potential of -48 mV $\pm$ 1 mV in deionized (DI) water with a volume fraction ϕ_{micro}. The suspension is dispersed using a sonic dismembrator (model 550, Fisher Scientific, Pittsburgh, PA) for 10 min and is stirred for 30 min. (Fisher Scientific, model 550). In Chapter 3, a separate colloidal suspension of diameter $2a_{nano} = 75$ nm polystyrene (PS) having a zeta potential of -59 mV $\pm$ 1 mV prepared at $\phi_{nano} = 0.35$ in DI water (supplied by the Emulsion Polymer Institute at Lehigh University) is mixed with the silica suspension to achieve the desired suspension composition. Coupled with the application of lateral oscillatory vibration, the addition of nanoparticles is used as packing aids for obtaining maximum microstructure order and packing density. In Chapter 4, the freshly prepared solution of sodium hydroxide (NaOH) and sodium chloride (NaCl) ranged from 10^{-7} to 10^{-3} mol/dm^3 are added into the silica

15

suspension to investigate the influences of suspension ionic strength and particle surface charge. In Chapter 5, ethanol (EtOH), 200 proof, and DI water are mixed into different EtOH:H_2O volumetric ratio to use as the base solvent for the silica suspension.

2.1.2 Substrate Preparation

Plain glass microslides ($76 \times 25 \times 1$ mm^3, Fisher PA) are used as deposition blades, and glass coverslips ($40 \times 24 \times 0.25$ mm^3, Fisher PA) are used as substrates for all samples. All glassware is cleaned by immersion in Piranha solution, 5:1 v/v sulfuric acid/hydrogen peroxide, for 30 min. The cleaned glassware is rinsed with DI water until no residual acid remains and is then immersed in DI water until use. Deposition blades are hydrophobilically treated with the addition of parafilm (Fisher PA) to their bottom edge. The contact angles on bare glass and on the hydrophobic surface are measured to be 10 and 105°, respectively, by imaging a 10 μl stationary droplet on the surface.

2.2 Experimental Methods

The experimental setup is shown in Figure 2.1. This apparatus is contained within a humidity-controlled environment where all experiments are performed at constant 20% relative humidity and 24 °C. The deposition blade angle α is placed at a set angle of $20° \leq \alpha \leq 80°$ approximately 10 μm above the substrate and observed directly using a digital camera (Dinolite AM311S). Next 10 μl of the colloid suspension is injected into the wedge between the substrate and deposition plate. A suspension meniscus is pinned atop a glass substrate, by a hydrophobically-treated deposition blade. The substrate is then translated at a specified deposition velocity using a linear motor (Harvard Instruments Co. Ltd.).

In Chapter 3, the modified setup is used. The motion of the substrate is controlled through a linear motor while a mechanical driver (PASCO SF-9324) and a waveform generator (Agilent 3320A) is used to control periodic oscillation. This setup is calibrated using high speed camera (Prof. Manoj Chaudhury's lab, Lehigh) at the capture rate of 500 frames per second. The amplitude calibration graph (Figure 2.2, raw data is shown in Table 2.1) shows the linear relation between input amplitude ($V_{peak-peak}$) and output amplitude (μm) for all frequencies of vibration. The schematic diagram, shown in Figure 2.3a, is similar to that for traditional convective deposition except for the added ability to oscillate the substrate along the deposition direction (Figure 2.3b).The position of the substrate is given by $x = v_w t + A_0 \sin\omega t$, where v_w is the apparent deposition velocity of the substrate and A_0 and ω are the amplitude and frequency of vibration. The relative velocity and acceleration of the sinusoidal motion scale as $A_0\omega$ and $A_0\omega^2$, respectively.

17
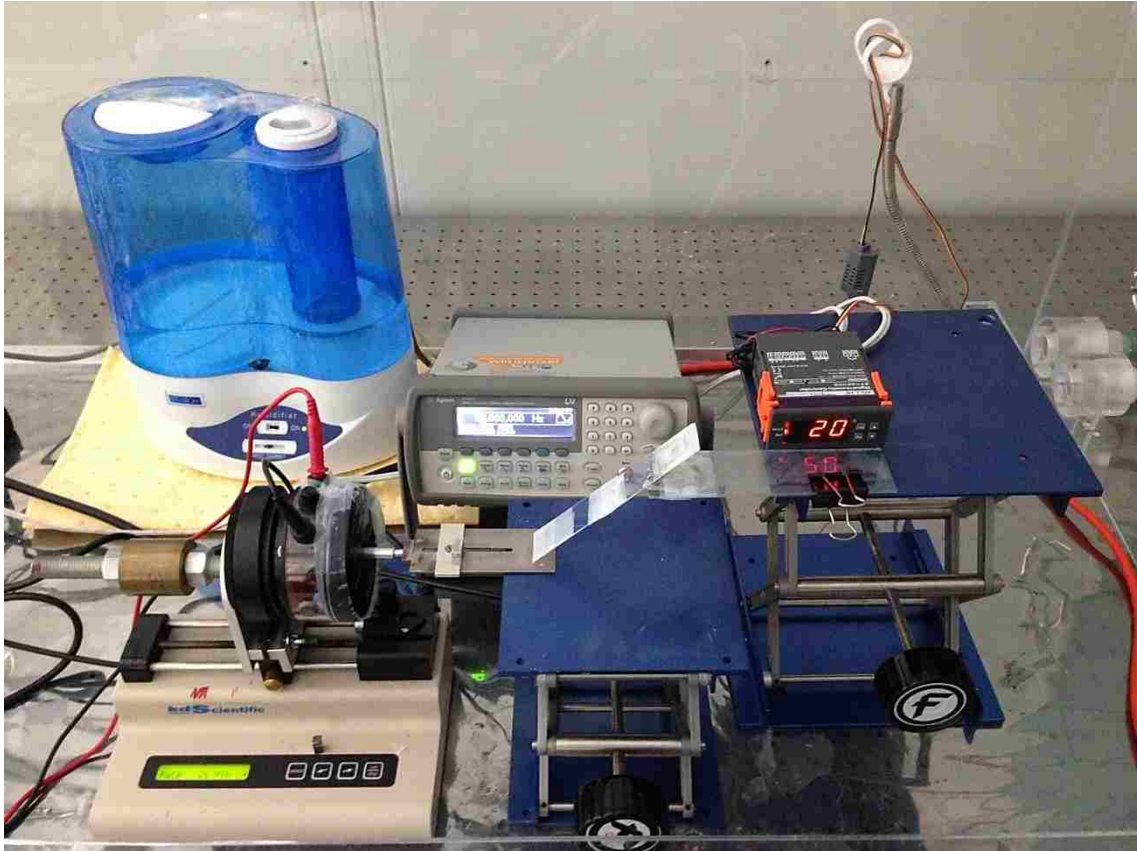
Figure 2.1: Experimental setup is in a humidity-controlled environment. All experiments are performed at constant 20% relative humidity and 24 °C.
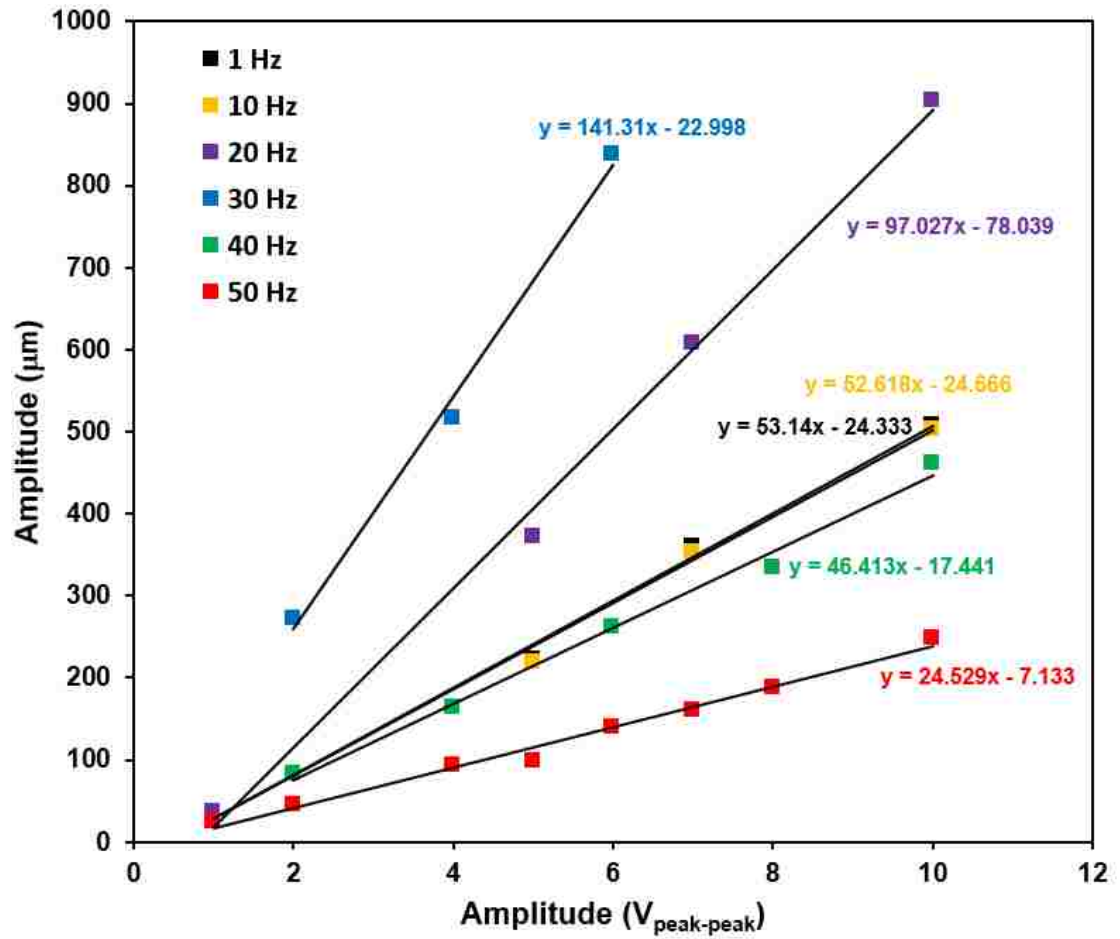
Figure 2.2: Amplitude calibration graph showing the linear relation between input amplitude ($V_{peak-peak}$) and output amplitude (μm) at frequency of vibration between 1-50 Hz.

Table 2.1: Raw Data of the Amplitude Calibration at the Vibration Frequency between 1-50 Hz

Frequency (Hz)	Input Amplitude ($V_{peak-peak}$)	Output Amplitude (µm)
1	1.0	35
	5.0	223
	7.0	359
	10.0	508
10	1.0	35
	5.0	219
	7.0	354
	10.0	503
20	1.0	37
	5.0	371
	7.0	607
	10.0	904
30	2.0	272
	4.0	517
	6.0	837
40	2.0	84
	4.0	163
	6.0	262
	8.0	335
	10.0	462
50	1.0	24
	2.0	45
	4.0	93
	5.0	99
	6.0	140
	7.0	161
	8.0	188
	10.0	248
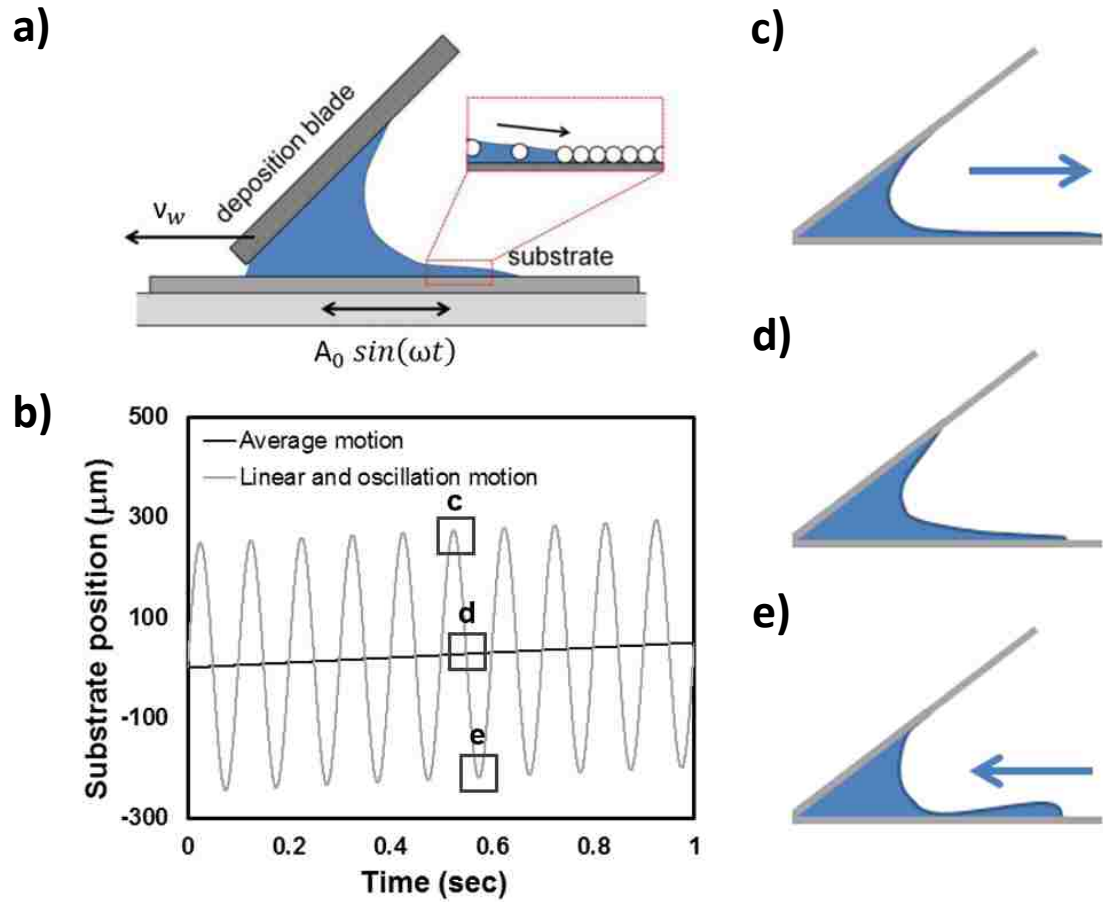
Figure 2.3: (a) Schematic diagram of experimental setup showing deposition apparatus with a substrate motion highlighted. (b) A graph of substrate motion showing (c) extended meniscus, (d) meniscus at normal position and (e) shortened meniscus with a small bump.

2.3 Microstructural Analysis

Deposited monolayers are observed directly using SEM (Hitachi 4300) after iridium coating and through confocal laser scanning microscopy after rewetting the layer with an aqueous solution of 8 mM Rhodamine B. Optical imaging of the sample is automated along the deposition length sampling ~60,000 microspheres. The relative microsphere substrate coverage, ρ, and the local bond order, Ψ_6, are evaluated. ρ is defined as the ratio of the projected area covered by microspheres to total sample area. The long-range microsphere substrate coverage is qualitatively reported. The maximum theoretical value of surface coverage for monosized microspheres deposited as a two-dimensional hexagonally-close packed (HCP) crystal is $\rho = \frac{\pi}{(12)^2} = 0.907$. In case of multilayers, the square-close packed structures are observed in the transition region between hexagonally-closed packed layers (Prevo and Velev 2004). The maximum theoretical value for these square-close packed structures is $\rho = \frac{\pi}{4} = 0.785$. This suggests that overall microsphere substrate coverage of multilayers is slightly lower than monolayers due to the presence of square-close packed structures. Ψ_6 is a parameter describing the relative crystallinity of particles. It is calculated using angles θ between each the particle of interest i and their nearest neighbors j. Vectors r_{ij} are determined for all nearest neighbors N and Ψ_6 is defined as:

$$\Psi_6(r_{ij}) = \frac{1}{N}\sum_{j=1}^{N}\exp[6i\theta(r_{ij})] \tag{2.1}$$

where $\Psi_6 = 1$ describes particles oriented in a perfect hexagonally close-packed crystal. A monolayer is seen as having $\rho \geq 0.8$ and $\Psi_6 \geq 0.575$. Submonolayers have densities $\rho < 0.8$ and identification of multilayer depositions are identified through direct imaging of multiple layers or through increased light reflectance.

Chapter 3

Enhanced Colloidal Assembly via Vibration-Assisted Convective Deposition

3.1 Introduction

Here, a substantial enhancement of the convective deposition process is presented in the addition of periodic vibration in the direction of substrate motion. The schematic diagram, previously shown in Figure 2.3a, is similar to that for traditional convective deposition except for the added ability to oscillate the substrate along the deposition direction (Figure 2.3b). The original motivation for this work was to investigate how perturbations would affect convective deposition and whether vibration would thwart efforts to scale up this process in a commercial setting.

Investigation into the stability of a vibrating film is a classic problem (Yih 1968; Baikov, Listrov, and Shabunina 1982; Or 1997; Shklyaev, Alabuzhev, and Khenner 2009; Benilov and Chugunova 2010; Porter et al. 2012; Bestehorn 2013). The first theoretical study was by Yih (1968). Thin liquid film on a horizontal and completely wetting substrate is considered. The substrate is oscillated in a horizontal direction. The flat

surface can become unstable only for long waves under a critical condition. The film instability happens only for a certain range of initial film thickness, depending on the oscillatory frequency and the fluid parameters. A sufficiently high oscillation frequency is required to excite the instability, for example, at least 300 MHz for a water layer with the thickness of 1 μm (Shklyaev, Alabuzhev, and Khenner 2009). Similarly, later studies from other researchers (Or 1997; Bestehorn 2013), using different mathematical analysis, shows a good agreement with Yih's result. Baikov and coworkers (1982) introduced the length, $\delta = \left(\frac{v}{\omega}\right)^{1/2}$, where v is the liquid kinematic viscosity and ω is the frequency of oscillating wall, to characterize the oscillating flow. This is also the characteristic length scale associated with Stokes' 2nd problem, often known as the 'Stokes Layer'. For high oscillation frequency the velocity pulsations decay with increasing distance from the wall. On the other hand, for low frequencies of oscillations the velocity changes slowly with time. The flow can be assumed stationary. In the case of the frequency $\omega \sim \frac{v}{d^2}$ where d is the liquid thickness, the vibrations of the wall are most favorable for the loss of stability. However, to introduce an instability in our system, the oscillation frequency required is about 1 MHz (where $v = 10^{-6}$ m^2/s and $d = 1$ μm) which is much higher than our scope of experiment ($0 \leq \omega \leq 100$ Hz).

Additionally, more recent studies have used vibration was used to influence colloidal assembly (Alvarez, Friend, and Yeo 2008; Rudenko et al. 2010). Notably, work by Wei and coworkers (2000) demonstrate that vibration of a monolayer of particles confined in a vertical soap film can anneal defects with a logarithmic coarsening profile;

however, the time scales in this work are inappropriately long for convective deposition due to the short particle residence time in the thin film and their scale-up limitations.

In this chapter we present intriguing results showing enhanced convective deposition through increased viable deposition velocities, enhanced robustness of the deposition process through transition to a monolayer-deposition window, and higher resultant packing and order of deposited monolayers. These enhancements occur over a large range of vibration frequencies and amplitudes. Toward the end of this chapter we present a simple and promising technique to assemble tunable square-packing structures by the introduction of external oscillatory motion of the substrate during convective deposition of multilayer colloidal crystals.

3.2 Experimental Results and Discussion

Glass substrates were coated using variable deposition velocity, $0 \leq v_w < 90$ µm/s, vibration amplitude, $0 \leq A_0 < 800$ µm, and frequency $1 \leq \omega \leq 100$ Hz. Similar to traditional convective deposition (effectively where $A_0 = 0$, Kumnorkaew and Gilchrist 2009), relatively large areas are easily coated with a small amount of solution in a uniform fashion, shown on a coated glass slide, under optimum conditions (Figure 3.1a). At the macroscopic scale, three qualitative observations are apparent with even the smallest vibration amplitudes sampled ($A_0 = 1$ µm). First, the quality of coated substrates appears more uniform and over a larger area versus those coated with constant velocity convective deposition. Second, buildup of particles along coating edges and the formation of multilayer streaks in the deposition direction are minimized with the vibration frequencies sampled. Third, although not investigated thoroughly for this study, substrates of variable hydrophobicity can be coated easily. Traditionally, convective deposition is limited to highly wettable substrates. Already, vibration-assisted convective deposition has been used to coat substrates with water contact angles up to 80°, including Fluorine-doped Tin Oxide (FTO), polyethylene terephthalate (PET), and GaN as shown in Figure 3.2. Although these effects are not quantified, they are readily apparent when using this technique in application.

Similar to traditional convective deposition, three surface morphologies are observed: particle submonolayers, monolayers, and multilayers (Figure 3.1b-3.1d). Depending on experimental conditions, samples may be comprised of a single morphology or may exhibit all three, deposited in a periodic manner in the direction of

deposition. Locally, microspheres are in contact with one another and the interstitial regions between particles are filled with nanoparticles (Figure 3.1e). Experimental conditions are tuned such that microspheres and nanoparticle are codeposited; neither component will be deposited alone and void spaces have neither microspheres nor nanoparticles (Kumnorkaew and Gilchrist 2009; Kumnorkaew, Weldon, and Gilchrist 2010).
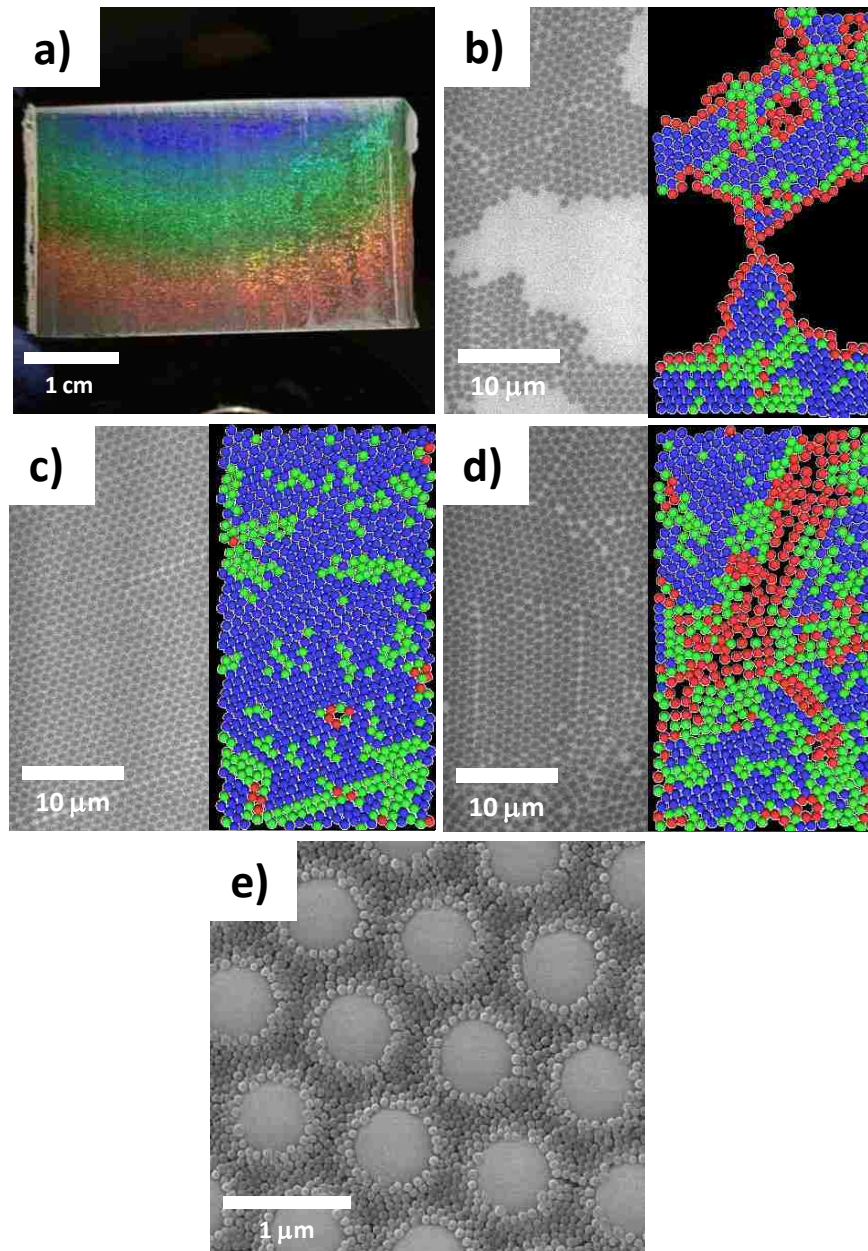
Figure 3.1: Examples of coatings at $\omega = 50\,\text{Hz}$ and $A_0 = 248\,\mu\text{m}$. Typical macroscopic coating using vibration-assisted convective deposition is shown in (a). The morphologies that result are (b) submonolayer, (c) monolayer, and (d) multilayer depositions, shown as optical images partnered with analysis where blue particles are ordered, red particles have fewer than 6 nearest neighbors, and green particles have 6 nearest neighbors with asymmetric neighbor locations. (e) SiO_2 microspheres are surrounded by and packed within polystyrene nanoparticles.
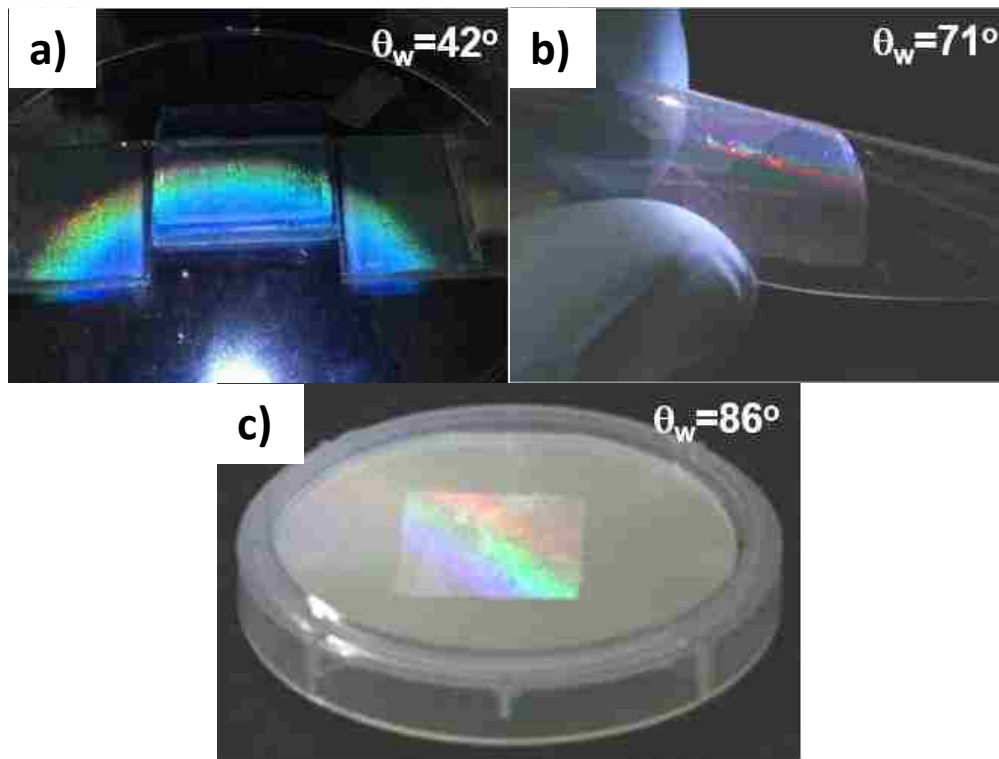
Figure 3.2: Samples showing successful coatings using vibration-assisted convective deposition on (a) Fluorine-doped Tin Oxide (FTO), (b) Polyethylene terephthalate (PET), and (c) GaN.

3.2.1 Overall Phase Diagram of Deposition

Figure 3.3 is the overall phase diagram of vibration-assisted deposition, which summarizes the effect of the amplitude (A_0) and the frequency of vibration (ω). Three distinguishable regions of operation are clearly noticeable. In the first region, the "Enhanced monolayer deposition" represents the operating conditions, which monolayer depositions over a range of deposition speeds are observed. Each datum is represented by shaded square. Darker squares mean wider range of monolayer deposition velocity ranging up to 25 μm/s. The packing and order of deposited monolayers within this region is apparently enhanced. In the second region, the "Phase separation" represents the operating conditions, which the lateral separation of microparticles and nanoparticles is observed across the whole area of deposition. Monolayer depositions cannot be achieved at any operating condition. This region is represented by open diamonds. In the third region, "Pseudo-steady" represents the operating conditions, which all three morphologies (submonolayers, monolayers, and multilayers) are deposited in a periodic manner in the direction of deposition. This region is represented by triangles. The transparent grey shade outside experimental data shows the conditions, which are not able to operate due to equipment's limitation.
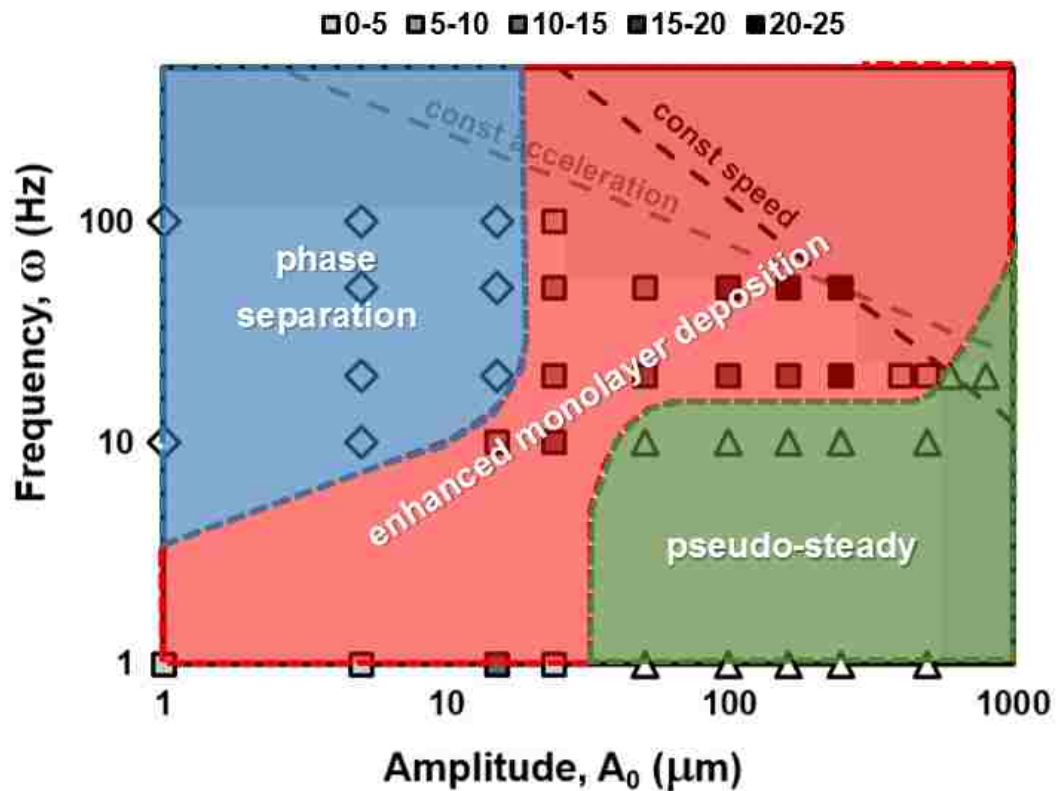
Figure 3.3: Overall phase diagram of vibration-assisted deposition, which summarizes the effect of the amplitude (A_0) and the frequency of vibration (ω). Open diamonds represent "phase separation" region. Squares represent "enhanced monolayer deposition" region. Each square is shaded with its respective range of monolayer deposition velocities. Triangles represent "pseudo-steady" region. Each region is shaded in color to guide the eye. The transparent grey shade outside experimental data shows the conditions, which are not able to operate due to equipment's limitation. Constant acceleration ($A_0\omega^2$) and constant velocity ($A_0\omega$) are shown in grey dash and black dash lines respectively.

3.2.2 Detailed Phase Diagram of Deposition

Significant enhancements resulting from the addition of vibration are exhibited in the detailed phase diagram (Figure 3.4). Non-vibrated samples, exactly replicating traditional convective deposition, show that a single monolayer condition exists at v_w = 47 μm/s (not shown in Figure 3.4). The addition of vibration yields two primary effects. First, for all A_0 sampled, the monolayer deposition velocity is increased. It can be interpreted that the effective length, l, of the thin film is increased similar to that seen in laterally vibrated evaporating droplets of water, where the evaporation is enhanced near the contact line. Experimental results are shown in Figure 3.5. Second, there is a wide monolayer deposition range of conditions. For ω = 1 Hz, a small region spanning less than 15 μm/s results in monolayer coatings at $1 \leq A_0 \leq 25$ μm; at high amplitude, no long range monolayer deposition condition exists. At ω = 10 Hz, the separation of microparticles and nanoparticles (Figure 3.6) is observed under confocal and scanning electron microscopy at low amplitude ($A_0 < 15$ μm) regardless of deposition velocity. At $15 \leq A_0 \leq 25$ μm, the range of monolayer deposition rates is roughly similar to ω = 1 Hz. At $A_0 > 25$ μm, all three morphologies are deposited in a periodic manner in the direction of deposition as shown in Figure 3.7. For higher frequencies, results are similar to ω = 10 Hz, but the range of conditions resulting in monolayer depositions increases drastically. With ω = 20 Hz and ω = 50 Hz, increases/decreases to deposition velocity by as much as ~50% do not necessarily transition deposition conditions beyond the monolayer regime, suggesting the mode of deposition has drastically changed. At ω = 100 Hz (not shown in Figure 3.4), similar to ω = 20 and 50 Hz, the separation of microparticles and nanoparticles is

33

observed at $A_0 < 25$ μm. At $A_0 = 25$ μm, the single monolayer deposition is noticed at v_w

$= 54$ μm/s. However, due to the limitation of experimental equipment, larger amplitude

of vibration cannot be examined.
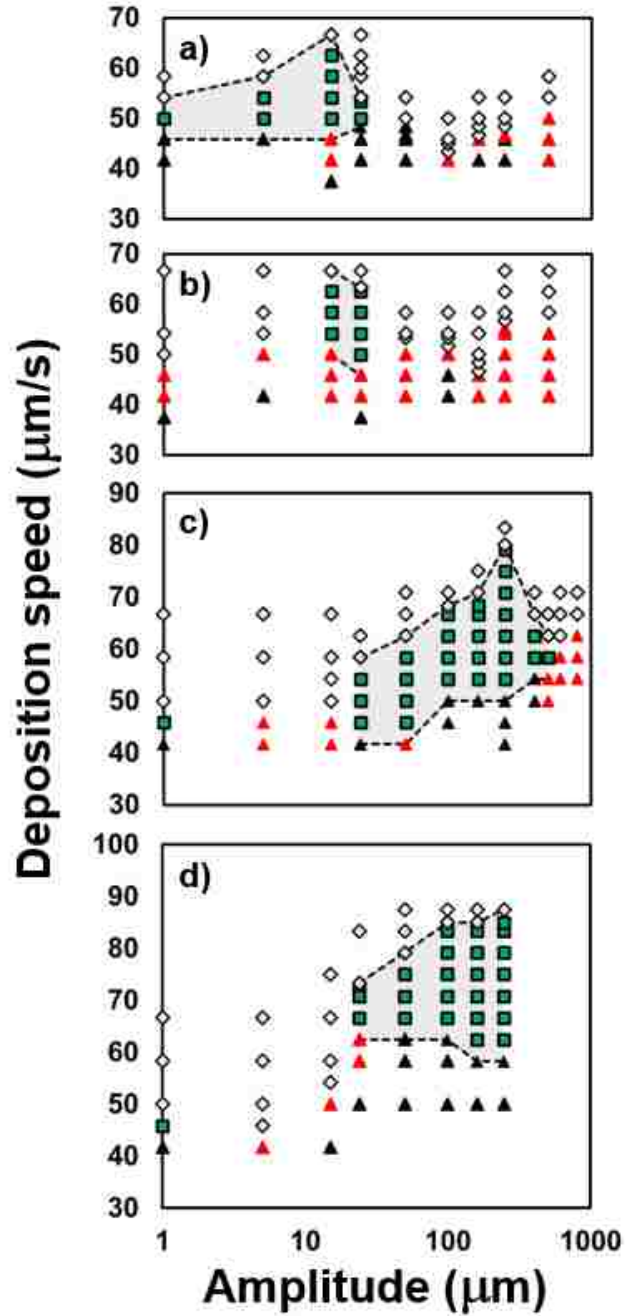
Figure 3.4: Phase diagrams show the resulting morphology as a function of changing amplitude, A_0, and deposition velocity for (a) $\omega = 1$ Hz, (b) $\omega = 10$ Hz, (c) $\omega = 20$ Hz, and (d) $\omega = 50$ Hz. Open diamonds represent submonolayer deposition, green squares are monolayer conditions, black triangles are multilayer depositions, and red triangles are combined three morphologies. The operating conditions for monolayer deposition are shaded in grey to guide the eye.
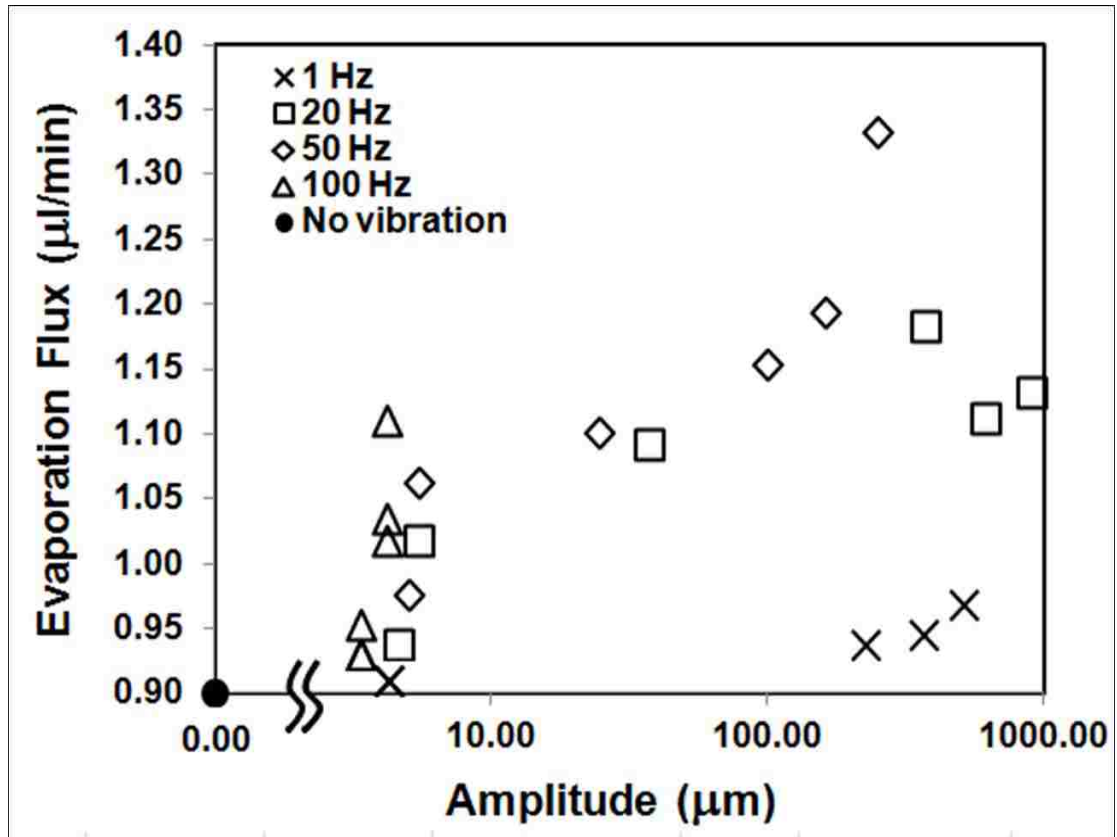
Figure 3.5: Evaporation flux of a 10 μl sessile drop of DI water on a vibrated substrate. Note that the x-axis, amplitude is plotted on a log scale. Through motion of the thin film near the contact line, evaporation rate is enhanced.
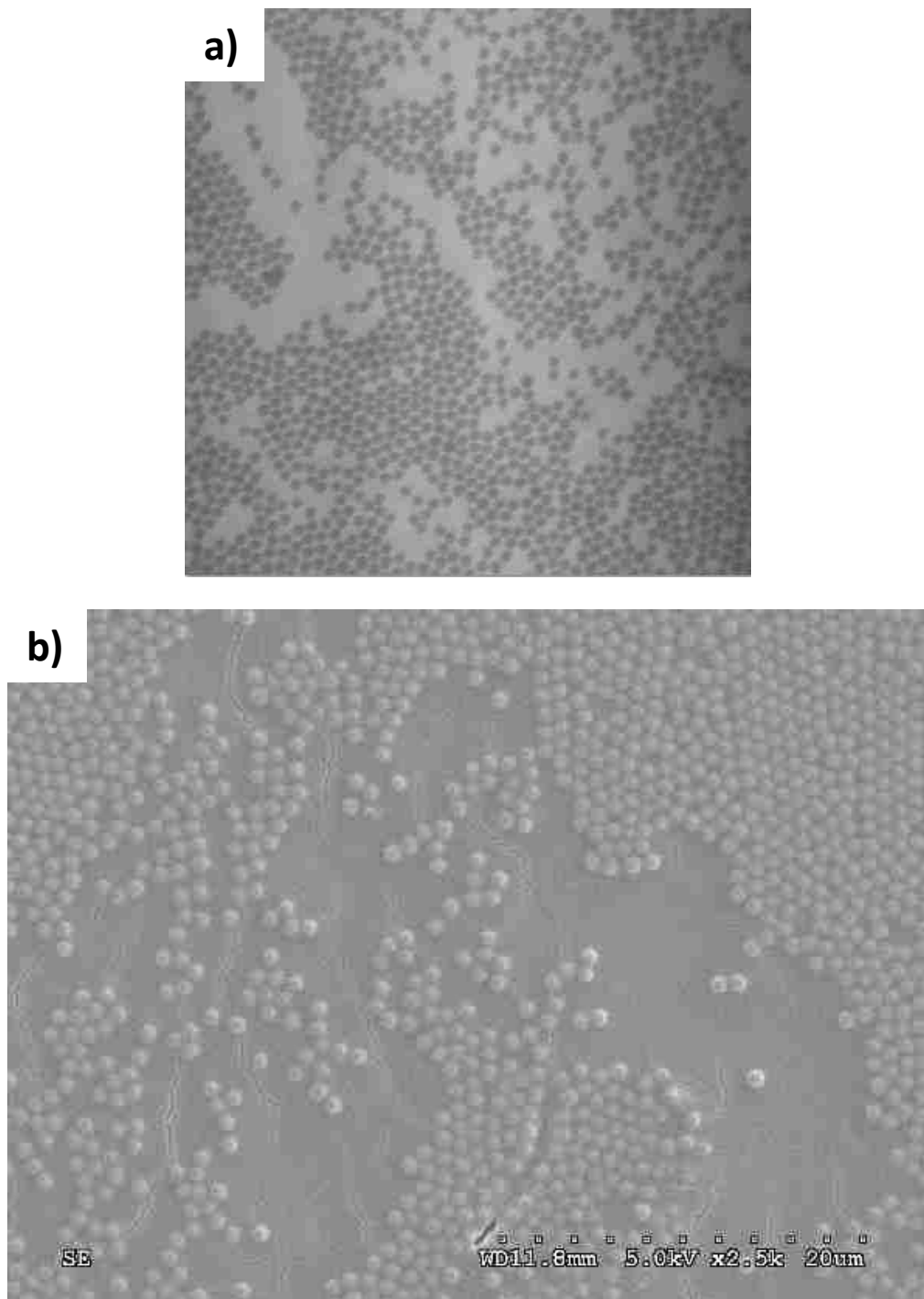
Figure 3.6: (a) Confocal and (b) scanning electron microscopy images show the separation of microparticles and nanoparticles deposited at $v_w = 46$ μm/s, $\omega = 10$ Hz and $A_0 = 1$ μm. It is noted that nanoparticles are invisible through confocal microscopy.
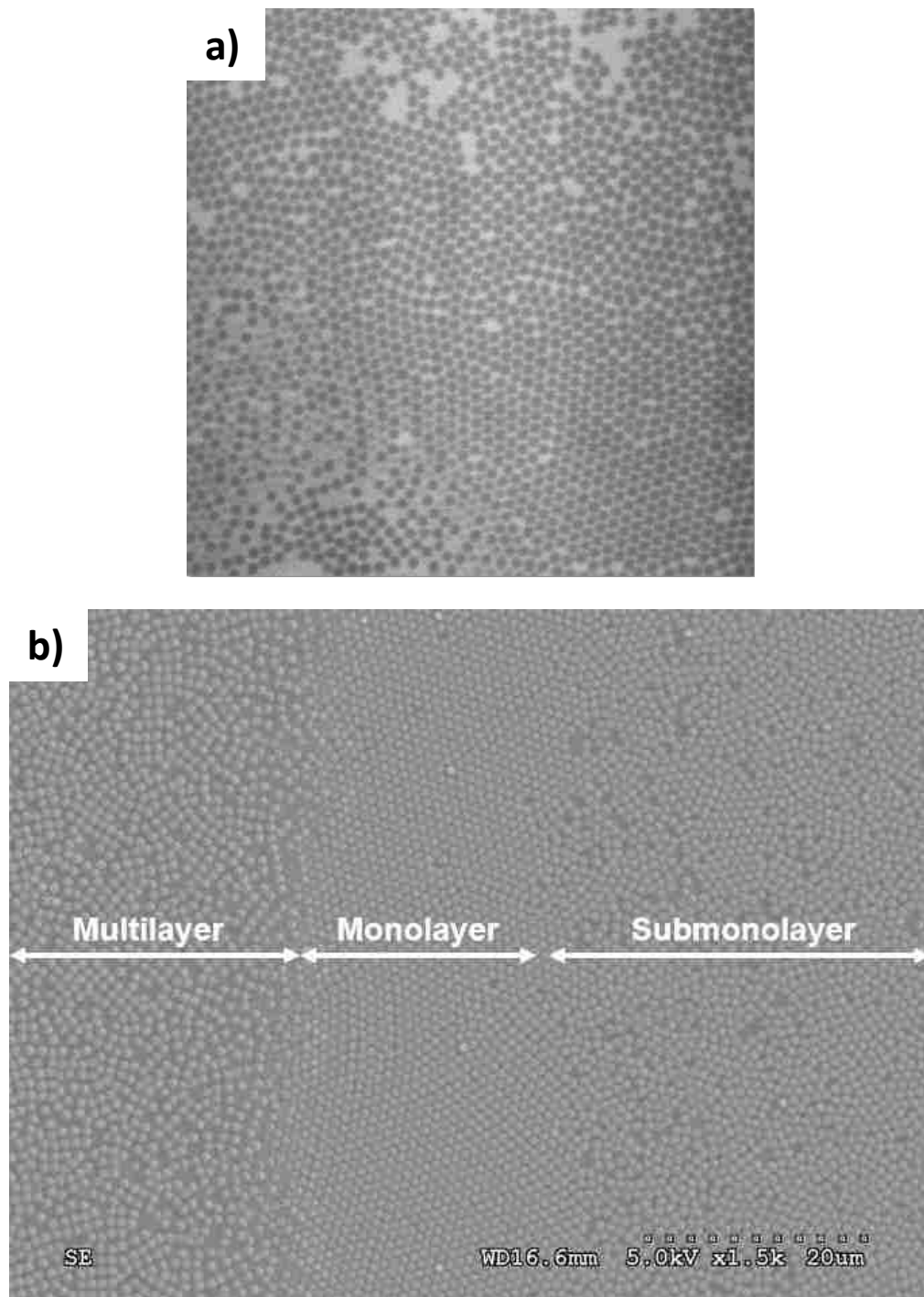
Figure 3.7: (a) Confocal and (b) scanning electron microscopy images show all three morphologies (submonolayers, monolayers, and multilayers) deposited in periodic manner at $v_w = 50$ µm/s, $\omega = 10$ Hz and $A_0 = 500$ µm.

3.2.3 Enhanced Monolayer Deposition

Through dimensional analysis (Table 3.1), one can consider the relative effects of inertia, surface tension, and viscosity. The Reynolds number, $Re = \dfrac{\rho A_0 \omega L}{\mu}$, relating inertial to viscous forces increases roughly 100-fold with vibration addition. However, it is still no more than $O(10^{-2})$ and thus is far below instability conditions for thin film flow. The capillary number, $Ca = \dfrac{\mu A_0 \omega}{\gamma}$, relating viscous to surface force also increases by roughly 100-fold; however, it also remains extremely small at $O(10^{-4})$. The Péclet number, $Pe = \dfrac{6\pi\mu a^3 \dot{\gamma}}{kT}$ (Brady and Bossis 1985), relating rate of convection to diffusion increases roughly 100-fold to $O(10^3)$ when based on the micrometer scale of silica particles. This suggests our system is dominated by the convection. The Weber number, $We = \dfrac{\rho A_0^2 \omega^2 L}{\gamma}$, increases to $O(10^{-3})$ when based on the millimeter scale radius of curvature of the droplet between the blade and substrate (We is $O(10^{-8})$ in case of traditional convective deposition). Although drop breakup is associated with We roughly $O(1)$, this amount of inertia is sufficient to alter the shape of a droplet (Dimitrakopoulos and Higdon 1997). Here, the suspension interface likely deforms due to lateral acceleration as evidenced by the increase in Bond number, $Bo = \dfrac{\rho A_0 \omega^2 L^2}{\gamma}$, to $O(10^{-3})$. This deformation would create pressure variations within the thin film that significantly alter the flow profile. Particles sliding over the substrate may sustain lubrication with

respect to the substrate, increasing the time which they can assemble before being brought into contact with the substrate through capillary force.

The two-dimensional packing density and local order in monolayer depositions are enhanced by vibration as well. Figure 3.8 shows compiled microstructural analyses. There is little variation in sample quality within the monolayer regime. In all samples, this vibration-induced reduction of deposition speed sensitivity results in smaller error bars. Particles likely have more relative time within the thin film to assemble before capillary forces pin the particles to the substrate. Further investigation is necessary to determine the specific changes in self-assembly within the thin film.

Table 3.1: Dimensionless Analysis

Dimensionless Number	Traditional Convective Deposition ($v_w = 50$ μm/s)	Vibration-Assisted Convective Deposition ($\omega = 50$ Hz, $A_0 = 248$ μm)
$Re = \dfrac{\rho v_w L}{\mu} = \dfrac{\rho A_0 \omega L}{\mu}$	1.0×10^{-4}	2.5×10^{-2}
$Ca = \dfrac{\mu v_w}{\gamma} = \dfrac{\mu A_0 \omega}{\gamma}$	6.9×10^{-7}	1.7×10^{-4}
$Pe = \dfrac{6\pi\mu a^3 \dot{\gamma}}{kT}$	14	3600
$We = \dfrac{\rho v_w^2 L}{\gamma} = \dfrac{\rho A_0^2 \omega^2 L}{\gamma}$	3.5×10^{-8}	2.2×10^{-3}
$Bo = \dfrac{\rho \Gamma L^2}{\gamma} = \dfrac{\rho A_0 \omega^2 L^2}{\gamma}$	0	8.6×10^{-3}

Note: $a =$ particle radius

$$\dot{\gamma} = \frac{v_w}{L} = \frac{A_0 \omega}{L}$$
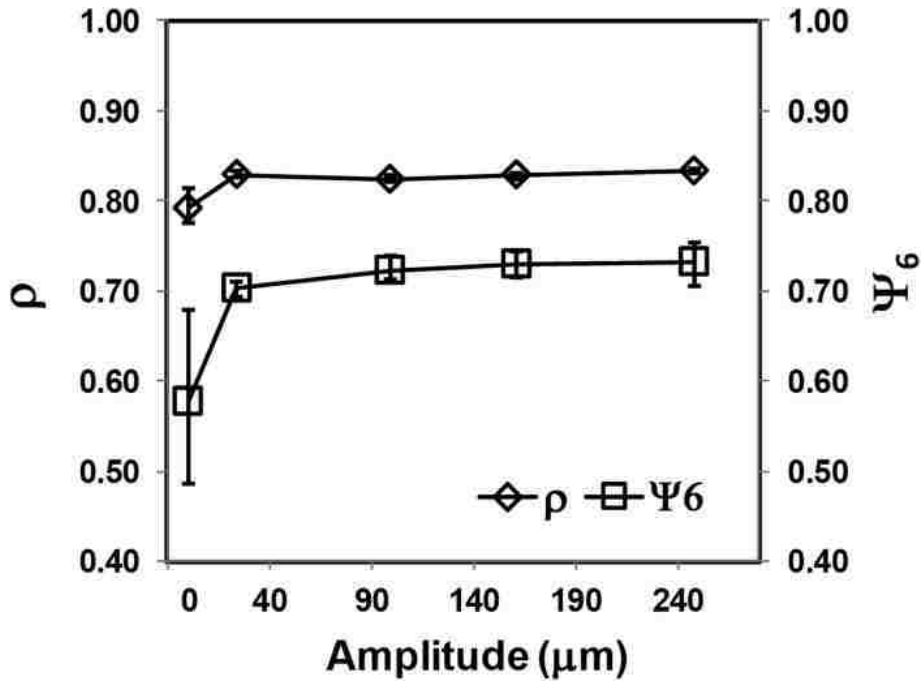
Figure 3.8: Surface density, ρ, and local order parameter, Ψ_6, as a function of vibration amplitude for $\omega = 50\,\text{Hz}$. Surface density and order increase as compared to traditional convective deposition, $A_0 = 0\,\mu\text{m}$, and smaller error bars indicate less variability between samples.

3.2.4 Phase Separation

As seen in Figure 3.3, the separation of microparticles and nanoparticles takes place at moderate frequency ($10 \leq \omega \leq 100$ Hz) and small amplitude of substrate vibration ($A_0 \leq 15$ μm). Considering near crystal front where liquid film thickness is slightly larger than microparticle diameter, incoming microparticles may experience a lift within thin film by vibration-induced lubrication forces while nanoparticles continuously flow along the direction of deposition and form layers at crystal front. The nanoparticle flux exceeds that necessary to fill the microparticle interstitial region, nanoparticles force this region to expand. It is important to note that the Péclet number when based on the nanoparticle diameter is equal or less than 1 for all operating conditions with this region, for example, $Pe_{nano} \sim 0.1$ when $\omega = 20$ Hz and $A_0 = 5$ μm. This suggests that nanoparticles are dominated by diffusion. However, the interaction of microparticles and nanoparticles in a motion is complicated. Figure 3.9 depicts confocal images of particle morphologies deposited at $10 \leq \omega \leq 100$ Hz and $1 \leq A_0 \leq 15$ μm. All experiments are performed at monolayer deposition velocity ($v_w = 58$ μm/s at $\omega = 10$ and 20 Hz; $v_w = 67$ μm/s at $\omega = 50$ and 100 Hz). With increasing amplitude of vibration, higher disorder of microparticles is seen at every ω.
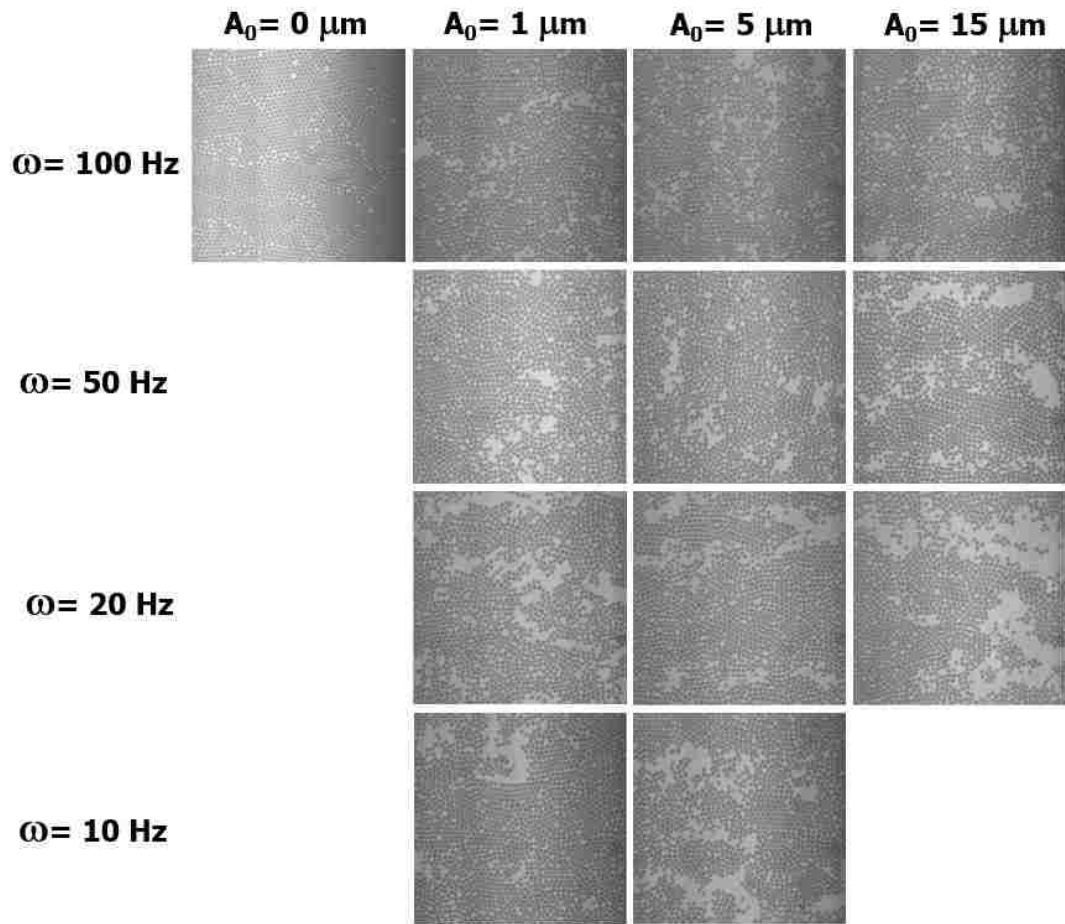
Figure 3.9: Confocal images of particle morphologies deposited at $10 \leq \omega \leq 100$ Hz and $1 \leq A_0 \leq 15$ μm. All experiments are deposited at monolayer deposition velocity.

3.2.5 Pseudo-Steady

As previously mentioned, "Pseudo-steady" represents the operating conditions, which all three morphologies (submonolayers, monolayers, and multilayers) are deposited in a periodic manner in the direction of deposition. This periodic variation of morphologies is a result of the slow and gradual change in deposition speed. This result will take place only at low frequency ($\omega \leq 20$ Hz) and moderate to long amplitude of substrate vibration ($A_0 \geq 50$ μm).

3.2.6 Effect of Blade Angle

Figure 3.10 presents the phase diagram identifying monolayer deposition resulting from different deposition velocities and blade angles. All experiments are performed at $\omega = 50\,\text{Hz}$ and $A_0 = 248\,\mu\text{m}$. At $\alpha = 20°$, monolayer deposition velocities are ranging between 38-58 μm/s. With increasing deposition angle, faster deposition velocity is required to maintain monolayer deposition. This increased monolayer deposition velocity is due to the increasing of evaporation rate and pressure gradient along liquid thin film (Kumnorkaew et al. 2008). At $\alpha = 45°$, the range of monolayer deposition velocities is roughly similar to $\alpha = 20°$ but the average monolayer deposition velocity is roughly 1.5 times faster. However, at $\alpha = 70°$, the range of monolayer deposition velocities is only 40% of those smaller angles. The average monolayer deposition velocity is nearly similar to $\alpha = 45°$. This result suggests that the addition of substrate vibration has less effect at high blade angle.

Looking into submonolayer deposition results, all depositions are performed at v_w = 108 μm/s and $\omega = 50\,\text{Hz}$. Figure 3.11 shows confocal images of the microstructure deposited at different blade angles ($20° \leq \alpha \leq 70°$) and amplitudes of vibration ($0 \leq A_0 \leq 248\,\mu\text{m}$). Here the characteristics of submonolayers (Figure 3.12) are identified by the ratio of the number of particles on the boundary of islands to total number of particles, $\dfrac{N_{boundary}}{N_{total}}$, and the ratio of the number of particles with $NN = 6$ and $\Psi_6 > 0.8$ within islands to total number of particles, $\dfrac{N_{(NN=6\,\&\,\Psi_6>0.8)}}{N_{total}}$. At $\alpha = 20°$, in case of non-vibrated samples

46

($A_0 = 0$ µm), $\dfrac{N_{boundary}}{N_{total}}$ and $\dfrac{N_{NN=6\,\&\,\Psi_6>0.8}}{N_{total}}$ are 0.12 and 0.19, respectively. At $1 \leq A_0 \leq$

15 µm, we observed the enhancement in particle packing as evidenced by the decrease in

$\dfrac{N_{boundary}}{N_{total}}$ to 0.02 and the increase in $\dfrac{N_{NN=6\,\&\,\Psi_6>0.8}}{N_{total}}$ to 0.48. On the other hand, at $25 \leq A_0 \leq$

248 µm, we observed the formation of particle islands. As increasing A_0, more particle

islands are observed as seen by dramatic increase in $\dfrac{N_{boundary}}{N_{total}}$ to 0.25. However, the order

of deposited particles within islands remains fairly constant. One possibility of the

particle island formation is that the deformation of liquid film by substrate vibration

causes temporary shifting of the crystal front to a new location. This shifting creates a

gap between the primary crystal front and the incoming particles. Liquid film thickness

is less than a particle diameter between this gap. The incoming particles stop at a liquid

thickness equal to the particle diameter and create particle clusters at secondary crystal

front. Since $v_w \gg v_{mono}$, each particle cluster is deposited separately. Particles within each

crystal domain may experience the rearrangement among themselves into well-ordered

particle islands by capillary forces. Next, at $\alpha = 45°$, $\dfrac{N_{boundary}}{N_{total}}$ and $\dfrac{N_{NN=6\,\&\,\Psi_6>0.8}}{N_{total}}$ are 0.08

and 0.21 in case of $A_0 = 0$ µm. At $1 \leq A_0 \leq 15$ µm, we observed the separation of

microparticles and nanoparticles, which results in the decrease of 25% in $\dfrac{N_{NN=6\,\&\,\Psi_6>0.8}}{N_{total}}$.

The mechanism is previously described in section 3.2.4. At $A_0 \geq 25$ µm, we observed

tremendous improvement of particle packing. $\dfrac{N_{boundary}}{N_{total}}$ decreases to 0.03 while

$\dfrac{N_{NN=6\,\&\,\Psi_6>0.8}}{N_{total}}$ increases to 0.71. Finally, at $\alpha = 70°$, $\dfrac{N_{boundary}}{N_{total}}$ and $\dfrac{N_{NN=6\,\&\,\Psi_6>0.8}}{N_{total}}$ remain

fairly constant at any A_0. Even though we observed slight decrease of 8% in $\dfrac{N_{boundary}}{N_{total}}$ and

increase of 5% in $\dfrac{N_{NN=6\,\&\,\Psi_6>0.8}}{N_{total}}$ at $A_0 = 248$ µm, the effect of substrate vibration is still not

conclusive.
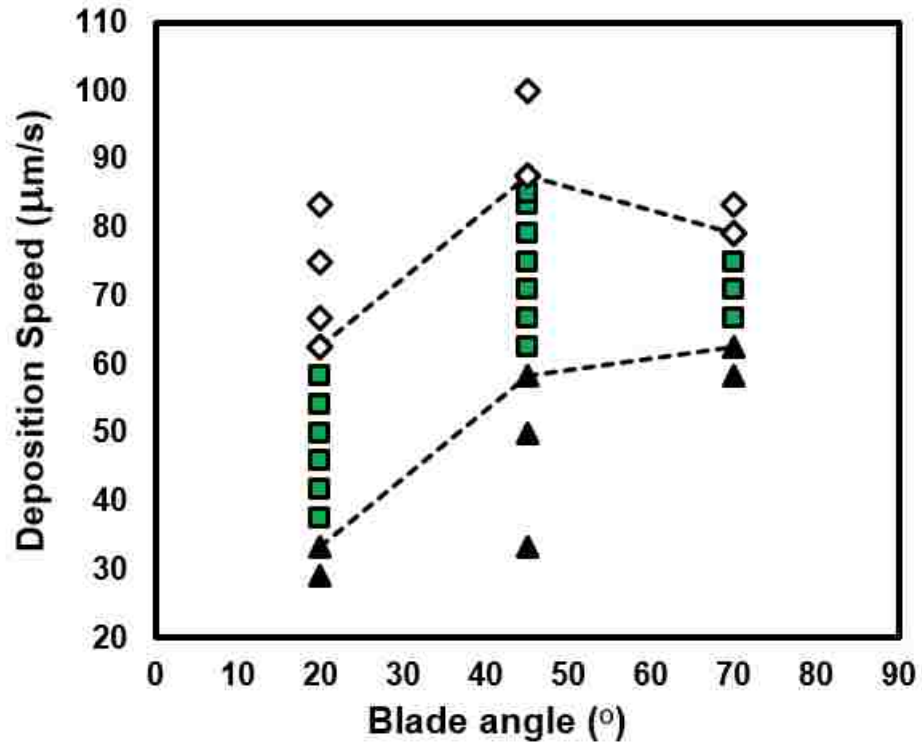
Figure 3.10: Phase diagram identifying monolayer deposition resulting from different deposition velocities and blade angles. All experiments are performed at $\omega = 50\,\mathrm{Hz}$ and $A_0 = 248\,\mu\mathrm{m}$.

$\alpha = 20°$

$\alpha = 45°$

$\alpha = 70°$

$A_0 = 0\ \mu m$ $A_0 = 1\ \mu m$ $A_0 = 5\ \mu m$ $A_0 = 15\ \mu m$ $A_0 = 24\ \mu m$ $A_0 = 99\ \mu m$ $A_0 = 161\ \mu m$ $A_0 = 248\ \mu m$
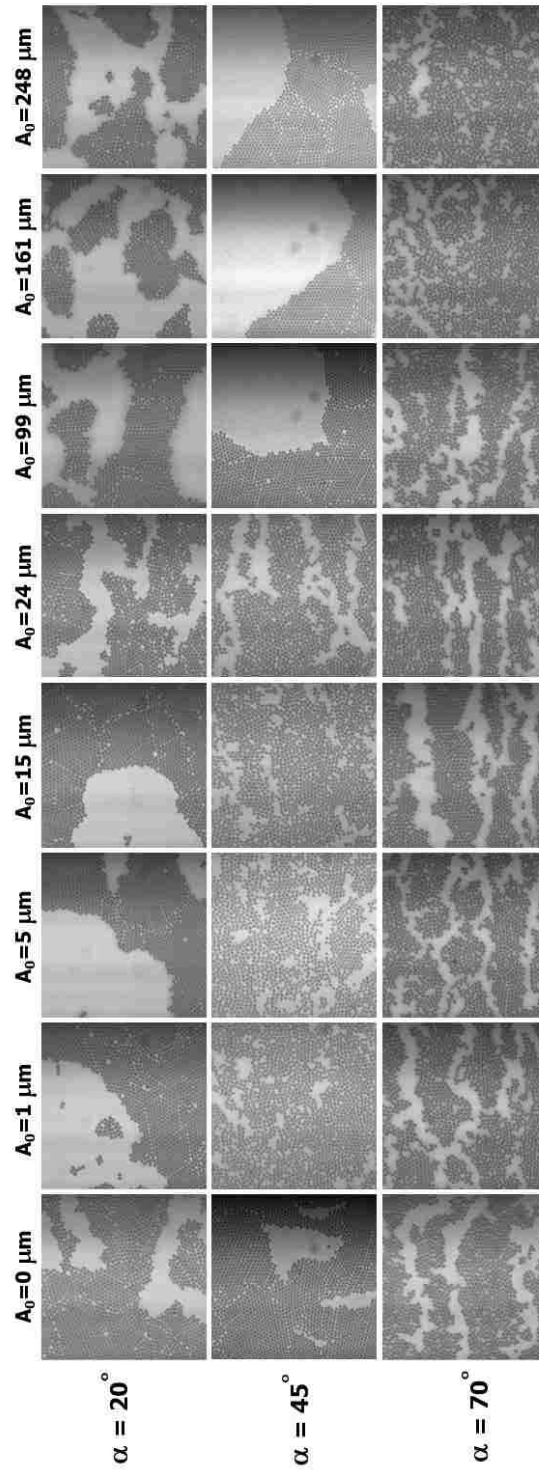
$0 \le A_0 \le 248\ \mu m$ $\mu m/s$ for all experiments $\omega = 50$ Hz, α

50
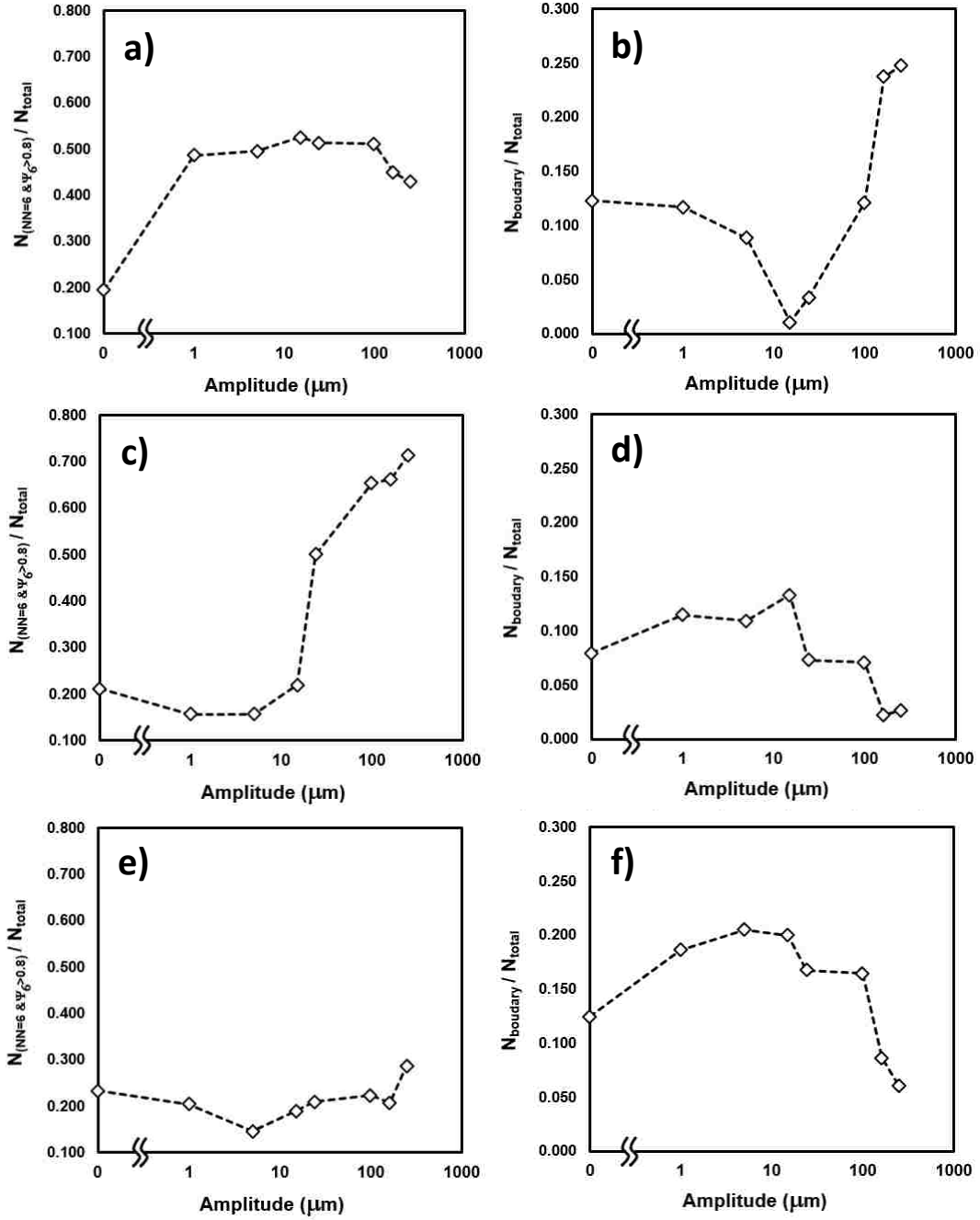
Figure 3.12: Graphs show an analysis of the samples in Figure 3.11. The left-hand column shows $N_{(NN=6\,\&\,\Psi_6>0.8)}/N_{total}$ while the right-hand column shows $N_{boundary}/N_{total}$. Blade angles are set at $\alpha = 20°$ for parts (a) and (b), $\alpha = 45°$ for parts (c) and (d), and $\alpha = 70°$ for parts (e) and (f).

51

3.3 Conclusions and Impact

We demonstrate a purely mechanical technique for enhancing evaporation-driven convective deposition of particle monolayers from suspension. Lateral vibration in the deposition direction results in monolayer deposition at faster speeds, over a wider range of withdraw rates, and with higher degree of order versus traditional convective deposition. These enhancements and phenomena are a result of variation in the thin film where capillary interactions result in self-assembly by dynamically changing the air-liquid interface. This enhancement in fabricating ordered particle thin films may enable development of optical and biological applications and efforts to scale-up this process for commercial application.

3.4 Template-free fabrication of partially aligned (100) fcc thin film colloidal crystals

The assembly of monosized colloidal particles into long-range spatial crystalline order has long been the focus of fundamental studies for several decades owing to their characteristic properties and applications in material engineering, optics and coatings (Pusey and Megen 1986). In contrast to natural particle assembly (Philp and Stoddart 1996) governed by intermolecular and interparticle forces (Min et al. 2008; Bishop et al. 2009), colloidal assembly (Whitesides and Grzybowski 2002) can be efficiently controlled through gravitational (Park, Qin, and Xia 1998), shear (Jiang and McFarland 2004; Ruhl, Spahn, and Hellmann 2003; Shereda, Larson, and Solomon 2010), as well as electromagnetic (Hayward, Saville, and Aksay 2000; Smoukov et al. 2009) forces. Among these techniques, convective assembly (Dimitrov and Nagayama 1996; Prevo and Velev 2004; Ghosh, Fan, and Stebe 2007; Kumnorkaew et al. 2008), the evopration-driven assembly of colloidal particles on a substrate, generates colloidal crystal films with fine control over film thickness and particle order over large sample areas.

The research on convective colloidal assembly is mainly focused on self-assembly of monosized particles into single continuous crystal domain. This approach although yields ordered crystalline assemblies, however results in a combination of hexagonally close packed (hcp) and face centered cubic (fcc) structures, which have negligible variation in free energies (0.005 RT/mole, Woodcock 1997). The presence of these dual structures results in defects in overall packing, which limits their use in applications demanding highly ordered crystals. Here, a mixture of these hexagonal symmetries can

53

be referred as "random hexagonally close packed" or rhcp arrangements. Additionally, photonic (Vlasov et al. 2001; Jin et al. 2006; Yang et al. 2009), magnetic (Sun et al. 2000; Kazakova et al. 2004), and structural (An and Yu 2013) applications require non-close packed structures, which has been unable to realize without an application of external forces or utilization of complex templates. Although non-close packed colloidal structures such as body centered cubic (bcc) have been studied in addition to hexagonally close packed (hcp) structures for specific particle volume fractions and charge screening in concentrated suspensions of charge stabilized particles (Sirota et al. 1989), a separation of these structures from solution is still complicated.

The spontaneous formation of square-packed domains by particle self-assembly, the (100) facets of fcc crystals, has been reported in confined transition regions between subsequent number of layers of hexagonal domains (Dimitrov and Nagayama 1996; Prevo and Velev 2004; Pieranski, Strzelecki, and Pansu 1983; Meng et al. 2006). However, the area of these transition regions is usually small and limited to only several particle diameters. Structures with (100) oriented colloidal-crystal planes has been reported successfully performed on pre-patterned substrates for many years (Blaaderen, Ruel, and Wiltzius 1997; Zhang et al. 2002; Yi, Seo, and Kim 2002; Lee et al. 2004; Hoogenboom et al. 2004; Jin et al. 2005; Yin, Li, and Xia 2003; Tanaka et al. 2006).

In this section, we report the utilization of substrate vibration during convective assembly of multilayer colloidal crystals to fabricate extensive and tunable square-packing structures. This substrate motion alters flow-patterns of the colloidal particles confined within the liquid film during convective assembly. Besides forming large (100)

fcc crystalline domains with relatively few defects, this technique is also able to control the crystal thickness and the proportion of hexagonal and square-packed arrangements.

Vibration assisted convective deposition was employed to assemble particles from aqueous solutions into multi-layer colloidal crystal films. The experimental setup described previously (Muangnapoh, Weldon, and Gilchrist 2013) employs a glass microscope slide as a coating blade, fixed at an angle of 45° and ~1 mm above an underlying substrate. The bottom edge of the blade was made hydrophobic through attachment of Parafilm so as to confine small volumes (200 µl) of colloidal solutions in the angle between the blade and substrate. Continuous convective deposition of colloidal crystalline films was achieved by particle convection to and pinning at the contact line of the meniscus with the substrate during translation of the latter. In addition to linear translation of the substrate, characteristic of conventional convective deposition processes (Prevo and Velev 2004), colloidal crystalline depositions in this work were carried out with the addition of controlled in-plane vibrations imposed in the same direction as that of the meniscus withdrawal. This was achieved through combination of a linear mechanical driver (kdScientific) and a mechanical driver (PASCO SF-9324) coupled with a waveform sinusoidal signal generator (Agilent 33220A).

Colloidal crystalline films were prepared in an enclosed chamber under controlled temperature (24°C) and humidity condition (20 %). Nominal depositions were prepared from a 10 % w/w suspension of 0.93 µm or 1.5 µm polystyrene (PS; Thermo-scientific) or silica particles (Fiber Optic Center Inc.) in water on 45 mm x 50 mm microscope cover-glass (Fisherbrand) or glass-supported PS substrates. The latter was prepared by

convective deposition of 0.30 µm PS particles (10 % w/w) into ca. 2 µm films (14 µm/s

at a humidity of 20 %) followed by melting at 240ºC for 45 min. In all cases, glass

substrates were pre-treated with piranha solution and subsequently rinsed with distilled

water and dried prior to deposition. Colloidal crystalline film thickness, N, was tuned by

controlling the rate of linear translation of the substrate, v_w (2–10 µm/s), and relative

humidity (i.e., evaporative solvent flux, j_e) according to the Equation 3.1 proposed by

Dimitrov and Nagayama (1996).

$$N = \frac{\beta l \, J_e \varphi}{0.605 v_w d (1 - \varphi)} \qquad (3.1)$$

where βl is a constant, φ is the suspension concentration and d is the diameter of particles

in the suspension. Nominal waveform generation, $A_0 \sin(\omega t)$, was carried out at a

frequency of $\omega = 40$ Hz and amplitude of ca. $A_0 = 1200$ µm.

Colloidal crystalline films were analyzed using white light irradiation and

scanning-electron microscopy (SEM) on a Hitachi 4300 instrument to assess particle

packing at the top-most layer of the film, and by laser scattering ($\lambda = 532$ nm, 15 mm^2 spot

size) by the films supported on glass substrates for insight into the bulk crystallinity and

crystal symmetry. The colloidal crystal samples were also analyzed using laser scanning

confocal microscopy (CLCM, Visitech) after wetting samples with 8 mM Rhodamine-B

dye in DMSO. CLSM scans were taken at sequential axial positions along the direction

of coating as well as through the thickness of the colloidal crystal film.

Figure 3.13 presents a comparison of multi-layered polystyrene colloidal crystals prepared on glass substrates by conventional convective deposition (Figure 3.13a-d) and vibration-assisted convective deposition (Figure 3.13e-h). White light irradiation (Figure 3.13a,e) of each colloidal crystal shows differences in the size of crystal domains. Especially, vibration-assisted assembly appears to increase the size of the single crystal domains (Figure 3.13e). Laser diffraction through these samples, carried out using a 532 nm wavelength laser with a 15 mm^2 spot size, confirms the large single crystalline domains prepared through vibration-assisted assembly (Figure 3.13f,g). On the other hand, Figure 3.13b shows the circular diffraction pattern in polycrystalline colloidal crystals assembled by conventional method due to lattice mismatch of smaller grains between hexagonal symmetries (Figure 3.13c). Laser diffraction from samples prepared by vibration-assisted assembly reveals two different crystalline symmetries. The first one is hexagonal symmetry (Figure 3.13f), commonly observed in colloidal crystals assembled by conventional method (Figure 3.13c,d). Second, the square/cubic symmetry (Figure 3.13g) refers to square-packed domains or (100) fcc as shown in the SEM image in Figure 3.13h.
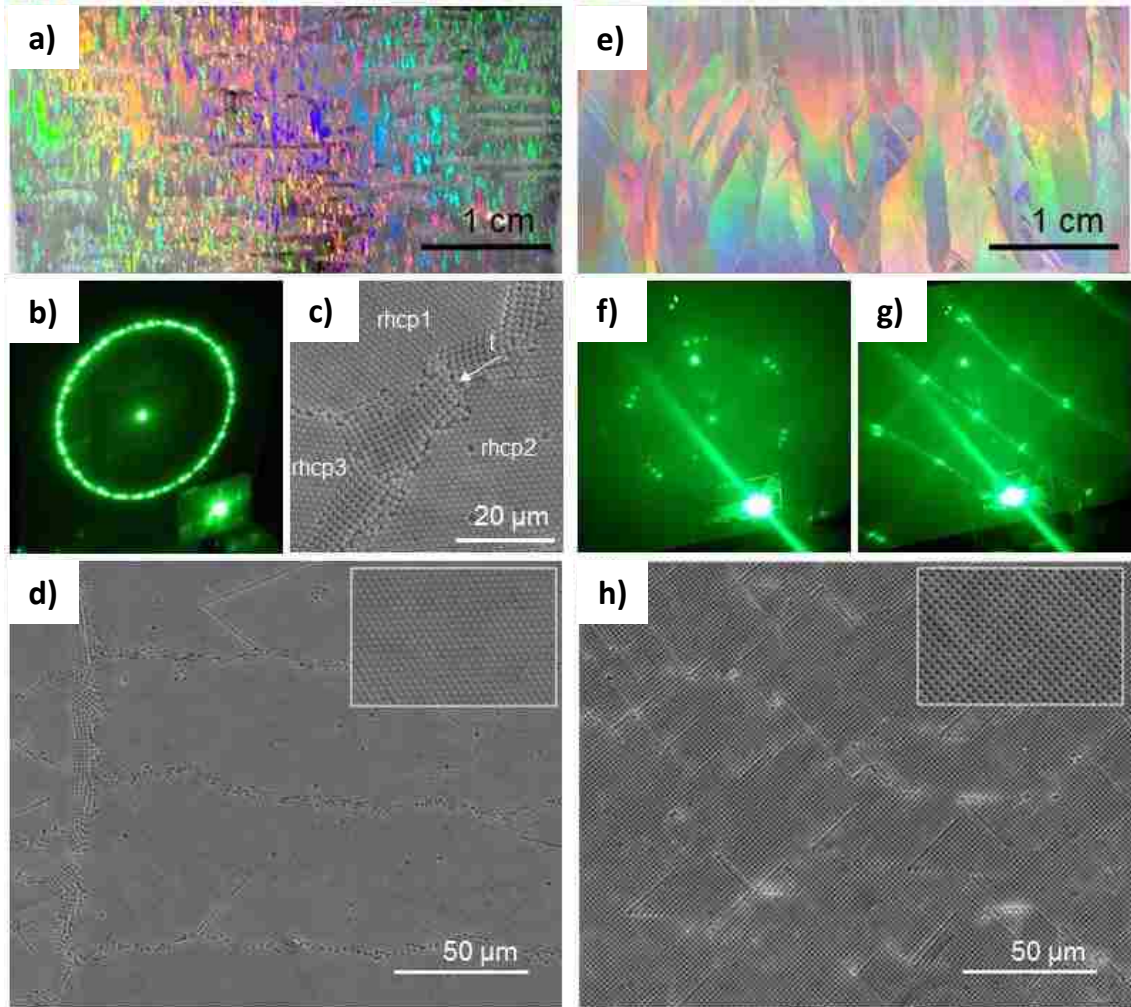
Figure 3.13: Comparison of colloidal-crystals assembled by conventional (a-d) and vibration-mediated (e-h) convective deposition (a,e) White light irradiation of representative colloidal crystals comprised of 1.5 µm polystyrene particles on glass substrates reveals differences in characteristic scales of polycrystallinity, with laser diffraction (15 mm² spot size) through the sample and corresponding SEM images of the colloidal crystal surface, indicating (b-d) micron-scale lattice-mismatched domains of rhcp symmetry with localized transition (shown as 't' in (c)) regions of square/cubic symmetry in the case of conventionally assembled colloidal crystals. The laser-diffraction experiments for samples obtained by vibration-mediated assembly shows a decidedly enlarged mm-scale domains of (f) hexagonal and (g,h) square/cubic symmetries. SEM images in (d,h) indicate the extent of the single crystallinity, with insets showing magnified views of the respective rhcp and square/cubic symmetries.

Further investigation of rhcp and square/cubic symmetries is explored under scaning electron microscopy and confocal laser scanning microscopy. Top-viewed SEM image (Figure 3.14a) of colloidal crystals prepared by vibration-assisted convective deposition of 0.93 μm polystyrene (PS) particles shows two distinct domains with differences in brightness. Darker regions possess a hexagonal arrangement of the close-packed structure (rhcp) while brighter regions possess a square-arrangement as shown in the inset to Figure 3.14a. Moreover, the quality of colloidal crystals can be quantified by confocal laser scanning microscopy (Figure 3.14b), a technique enabling collection of optical slices through the thickness of the colloidal crystal and its subsequent 3D-reconstruction (Figure 3.14c). The transition between the (100) fcc domains and rhcp domains occurred along well-defined sharp boundaries (Figure 3.14c), with the grain boundary extending vertically down across all the layers to the bottom-most layer of the assembly (Figure 3.14b). These vertical boundaries occur in contrast to (100) fcc assemblies obtained by epitaxy (Lee et al. 2004), primarily demonstrating 45º planar boundaries between domains, greatly reducing the effectiveness of the imposed surface structure.
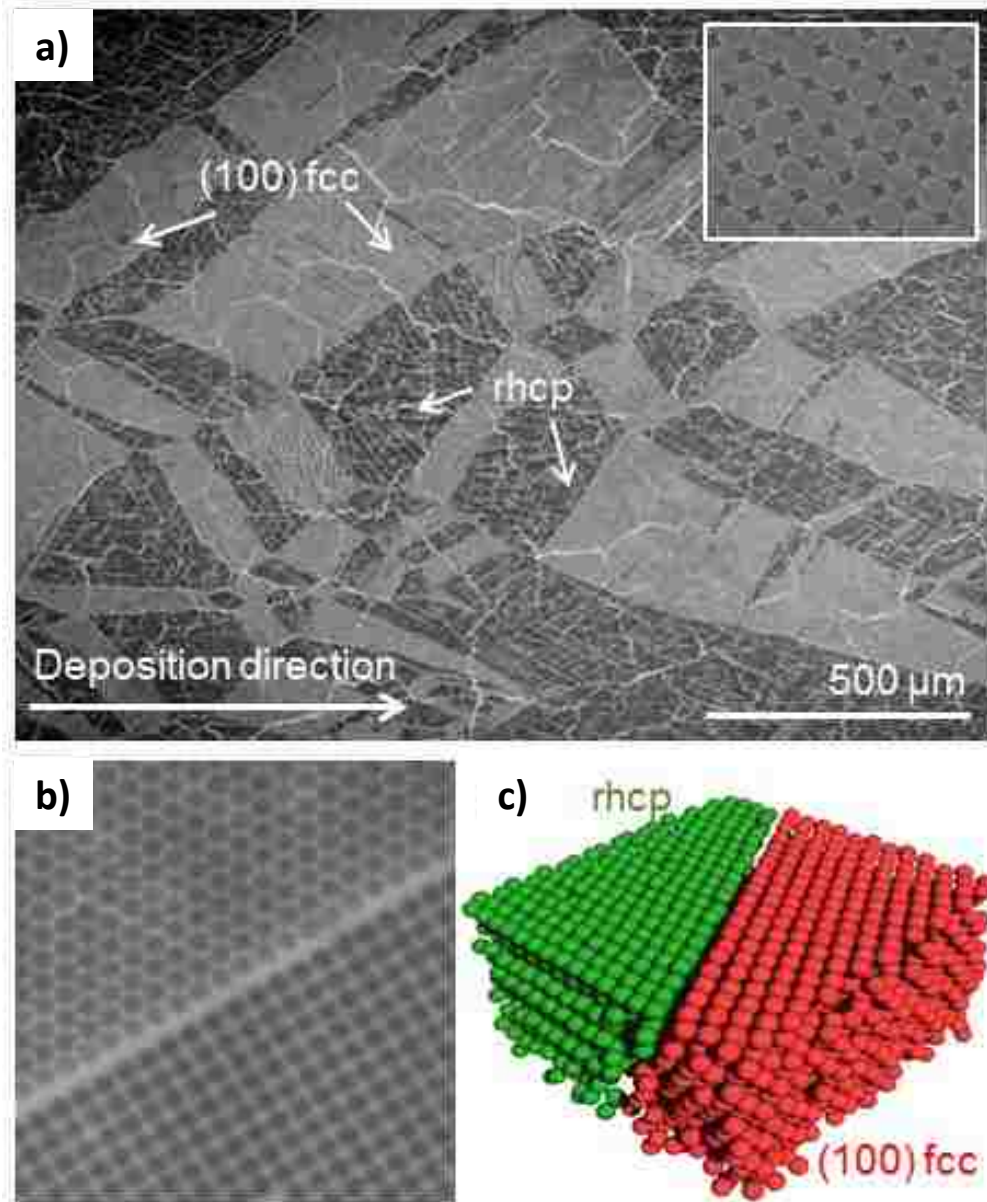
Figure 3.14: Structural analysis of multi-layer cubic colloidal-crystals achieved by vibration-assisted convective assembly carried out by (a) SEM analysis of the top surface of the colloidal crystal (square packing of '(100) fcc' domains shown in inset), (b) CLSM imaging of adjacent single crystalline domains at the crystal-substrate interface, and (c) 3D reconstruction of the colloidal crystalline structure at a representative grain boundary. Analysis is shown for representative assemblies of 0.93 µm polystyrene (PS) particles.

The introduction of substrate vibration creates a back-and-forth movement of the meniscus (Figure 3.15a), resulting in a dynamic meniscus shape, as illustrated in Figure 3.15b,c. One possible mechanism for the formation of (100) fcc crystalline domains could be the result of shearing of particle suspensions. There has been reported many studies on simple sheared colloidal systems (Dozier and Chaikin 1982; Ackerson and Clark 1983; Chen et al. 1992; Chen et al. 1994) as well as order induced by flow in Couette devices (Ackerson 1990) as well as planar geometries (Stancik et al. 2004) and Poiseuille flow (Sawada et al. 2001). Under oscillatory shear, the resulting structure depends on the direction of shear forces as well as the relative magnitudes of shear and inter-particle forces (Haw, Poon, and Pusey 1998; Panine et al. 2002; Besseling et al. 2012). In all of these systems, they observed only a formation of hexagonal symmetry, which is parallel to the boundaries of the system. However, in this work, the dynamic meniscus shape arising from substrate vibration might generate clusters with both hexagonal and square symmetry, which act as nucleates for the addition of incoming particles (Figure 3.15d). Moreover, this external shear might rotate generated clusters depending on the amplitude and frequency of substrate vibration. This can be observed in Figure 3.15d in which the large (100) fcc domains have a preferential orientation of 30$^{\text{o}}$ with respect to the deposition direction.
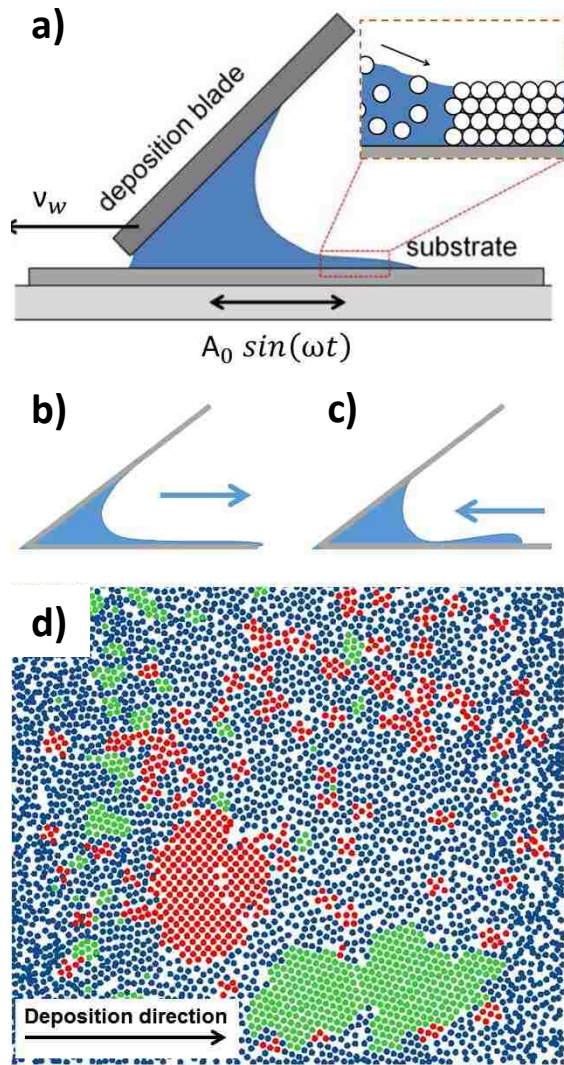
Figure 3.15: Schematic of vibration-assisted convective assembly and image analysis of in situ structure during assembly. (a) Schematic of the experimental setup for the vibration-assisted convective assembly procedure wherein the deposition blade is advanced at a velocity, v_w, while the substrate undergoes oscillatory in-plane vibrations, $A_0 sin(\omega t)$, leading to periodic (b) elongation and (c) compression of the liquid meniscus during each cycle of the vibration. (d) Simultaneous formation of square and hexagonally packed regions through a nucleation-growth mechanism demonstrated by a color-rendered in-situ confocal image. The image obtained using 0.93 μm PS particles and at 40 Hz and amplitude of ~10 μm, comprises of both hexagonal (green) and square (red) packed nucleates being generated in the suspension (blue), suggesting a nucleation-growth mechanism during convective assembly.

The self-arrangement of colloidal particles into non-hexagonal arrangement under the influence of flow fields has been suggested as a viable alternative to epitaxial approaches to engineer the packing structure in colloidal crystals. This approach adds vibration to the convective deposition process, inducing variations in solvent flow characteristics and meniscus properties, thereby resulting in spontaneous arrangement of particles in an oriented fcc (100) pattern parallel to the substrate and at a preferential angle $\alpha \sim 30°$ relative to the mean flow direction. This spontaneous ordering has been achieved in the absence of thickness variations, with an increasing trend for the phenomena observed with an increase in the number of layers of the colloidal crystal assembly. The possibility that variations of flow characteristics can organize the particles into various packing arrangements opens up new avenues to obtain tailored crystal structures tuned to the desired optical and structural requirements.

Chapter 4

Effect of Ionic Strength and Surface Charge on Convective Deposition

4.1 Introduction

This chapter focuses on a fundamental understanding in particle-particle and particle-substrate interactions as well as impacts of ionic strength of medium and particle surface charge on convective deposition. Considering Nagayama's equation (Eq. 1.1), β is a value representing particle-particle and particle-substrate interactions (Dimitrov and Nagayama 1995), which is assumed to be between 0-1. β approaches 1 for low volume fraction and electrostatically stable particles. However, β is a function of many parameters such as capillary force, ion strength of medium, or particle surface charge, which are simply hidden within this parameter. Previous studies have shown that other parameters such as the deposition blade angle (Kumnorkaew et al. 2008), the hydrophobicity of the deposition blade (Kumnorkaew et al. 2008), the introduction of nanoparticle (Kumnorkaew and Gilchrist 2009; Kumnorkaew, Weldon, and Gilchrist 2010), or the external mechanical vibration (Muangnapoh, Weldon, and Gilchrist 2013) have a big impact on the final morphology of deposited particles. Here in this work we

aim to investigate effects of ionic strength of medium and surface charge of particles on convective deposition by simply controlling the concentration of NaCl and NaOH added into particle suspension. Coupled with DLVO theory, an electrostatic barrier and an effective separation distance can give better ideas of how particles interact with other particles and substrate.

4.2 Experimental Results and Discussion

A surface charge of silica particles in aqueous phase is acquired by the dissociation of silanol group, SiOH (Iler 1979). This equilibrium is sensitive to surrounding conditions. An addition of electrolyte can drive new dissociation equilibrium resulting in more surface charge of silica particles as equilibrium shifts (Papirer 2002). In this study the surface charge of silica particles is controlled by an addition of NaOH until achieving desirable concentration of OH⁻. The reaction is shown below.

$$SiOH + OH^- \rightleftharpoons SiO^- + H_2O$$
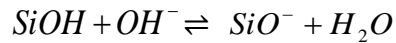
Zeta potential (ξ) measurement gives an idea of surface charge on colloidal particle. Figure 4.1 depicts the zeta potential of silica particles as a function of OH⁻ (open symbols) and NaCl (close symbols) concentration. Without an addition of NaOH, [OH⁻] $= 10^{-7}$ mol/dm^3, ξ of silica particle is -22 mV. The zeta potential of silica particles linearly decreases with respect to increasing concentration of adding NaOH. At [OH⁻] = 10^{-3} mol/dm^3, ξ of silica particle is -110 mV which suggests strong repulsion forces among silica particles. On the other hand, ξ of silica particle remains fairly constant with any addition of NaCl. ξ of silica particle remains roughly constant at -40 mV at [NaCl] $\leq$ 10^{-4} mol/dm^3, and slightly increases to -25 mV at higher salt concentration. These measurements suggest that the addition of NaOH alters both ionic strength and surface charge while the addition of NaCl alters only in ionic strength (Kershner, Bullard, and Cima 2004).
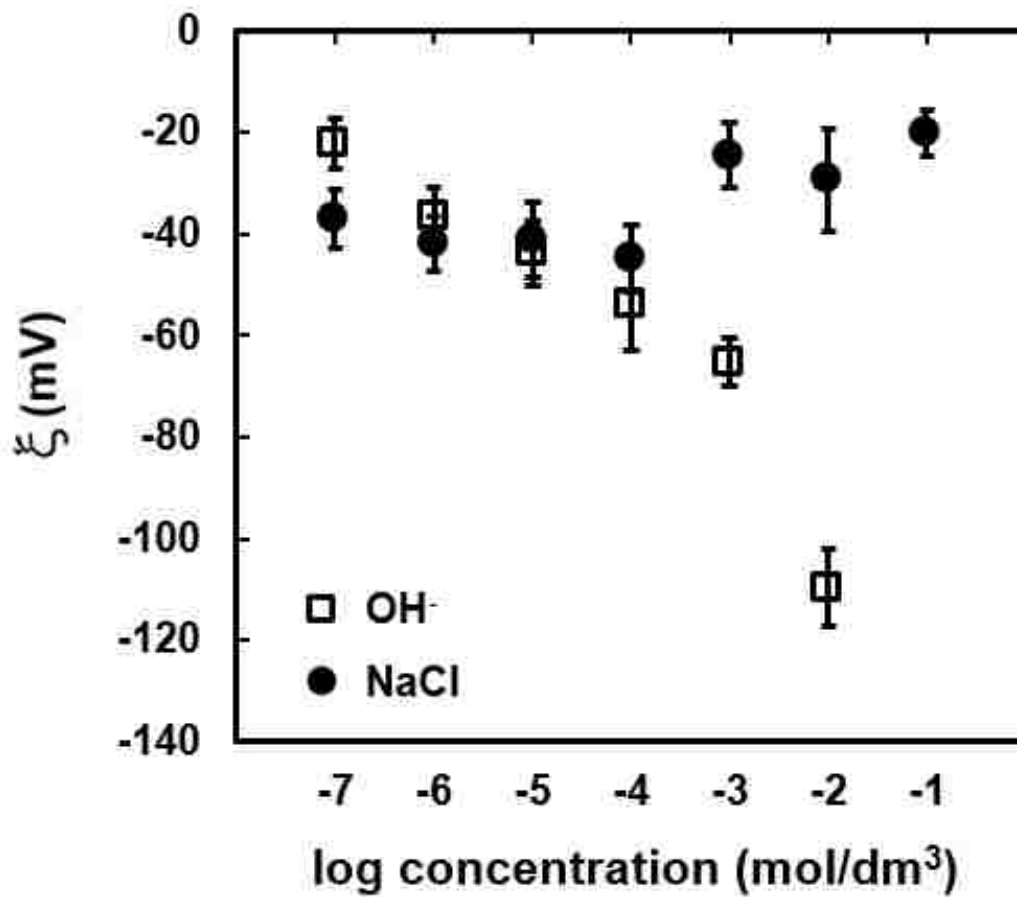
Figure 4.1: Zeta potential (ξ) as function of concentration of NaCl and OH$^-$ (mol/dm^3).

4.2.1 Effect of Ionic Strength on Convective Deposition

An ionic strength of medium depends on number of ions and ionic charge. Adding either NaOH or NaCl results in changing in the ionic strength. Here to observe effects of only ionic strength on convective deposition, [NaCl] ranged from 10^{-7} to 10^{-3} mol/dm^3 is added. The two-dimensional packing density (ρ) and local order of deposited particles (Ψ_6) are analyzed using confocal imaging. As shown in Figure 4.2, particle morphology can be categorized into 4 groups: (a) multilayer, (b) monolayer with $0.70 < \rho < 0.75$ and $\Psi_6 \geq 0.575$, (c) monolayer with $\rho \geq 0.75$ and $\Psi_6 \geq 0.575$ and (d) submonolayer. The effect of ionic strength on monolayer deposition is displayed in Figure 4.3. Similar to traditional convective deposition, the range of monolayer deposition velocity spans less than 10 μm/s. However, ρ and Ψ_6 of monolayer deposition are dramatically depressed even with little addition of NaCl (noted that $\rho = 0.80$ and $\Psi_6 = 0.75$ for monolayer deposition in traditional convective deposition). Red squares in Figure 4.3 represent monolayers with $0.70 < \rho < 0.75$ and $\Psi_6 \geq 0.575$. Although, at $10^{-7} \leq$ [NaCl] $\leq 10^{-5}$ mol/dm^3, the monolayer deposition velocity matches with traditional convective deposition, it decreases about 17% at [NaCl] $= 10^{-4}$ mol/dm^3 and further decreases to about 35% at [NaCl] $= 10^{-3}$ mol/dm^3. One possible reason of this depreciation in monolayer deposition velocity could be due to the difference in particle flux in thin film. Without an addition of NaCl, particles could not exist in vicinity of substrate due to electrostatic repulsion. As Debye length decreases, the effective area for particle flow increases which might slow down overall particle velocity, thus effective flux.

69
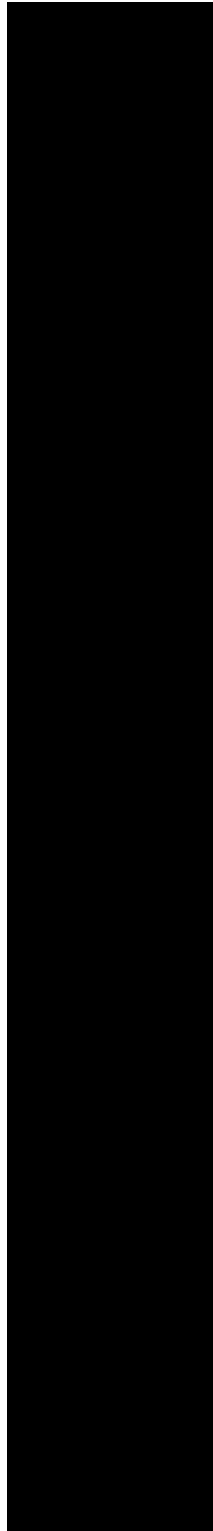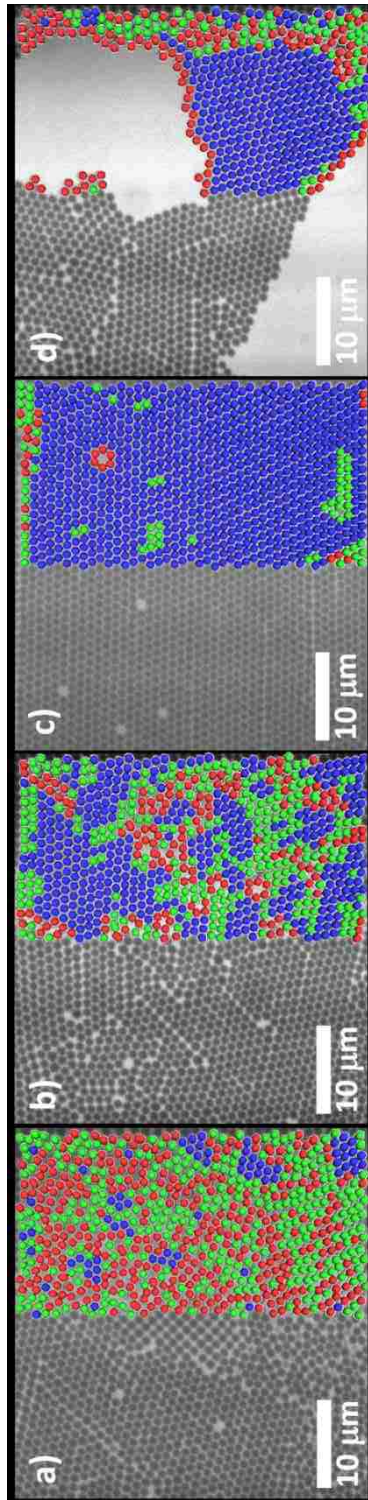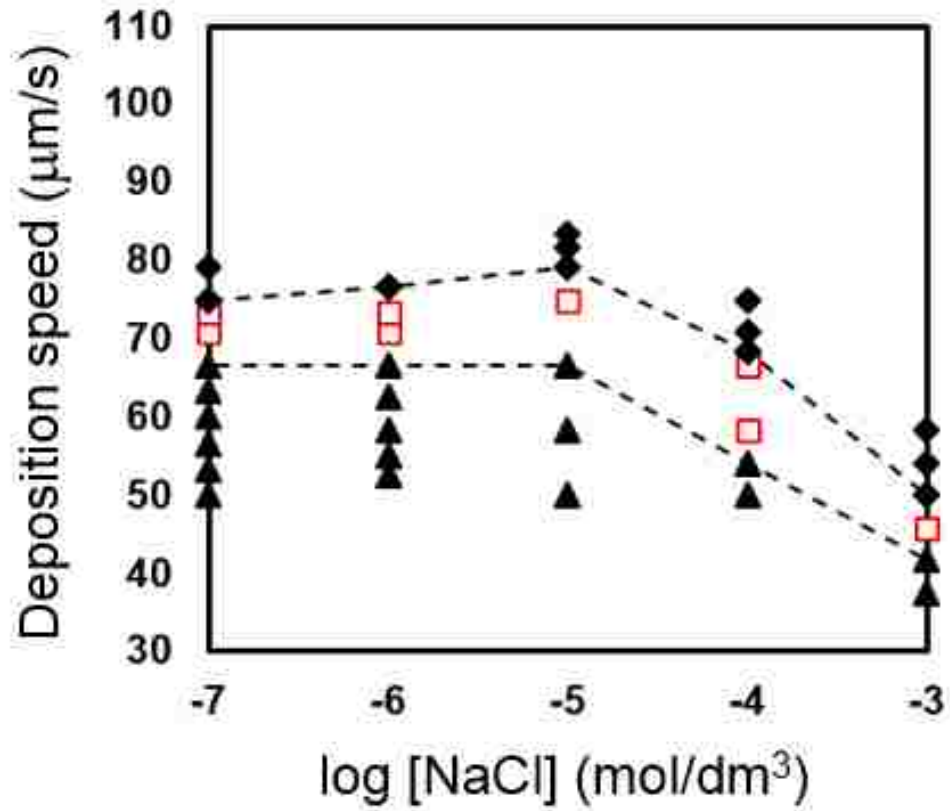
Figure 4.3: Phase Diagram showing monolayer deposition velocity (μm/s) as a function of log of concentration of NaCl (mol/dm^3). Triangles represent multilayer deposition. Diamonds represent submonolayer deposition. Red rectangles represent monolayer deposition with $0.70 < \rho < 0.75$ and $\Psi_6 \geq 0.575$.

The electrostatic barrier as a function of distance between particle and substrate as well as the effective separation distance as function of concentration are calculated from mathematical simulation using DLVO theory (Zeng 2013). In case of $[NaCl] \leq 10^{-5}$ mol/dm^3, Debye length strongly depends on volume fraction because particles screen themselves. The effect of high particle volume fraction on Debye length was taken into account using following equation (Papirer 2002; Lebovka 2014).

$$\lambda_D(\phi) = \lambda_D^0 \sqrt{\frac{1-\phi}{1+1.5\sigma\phi/(e\rho r)}}$$
(4.1)

Where ϕ = Volume fraction of suspension

$\lambda_D(\phi) =$ Debye length at a volume fraction of ϕ (m)

$\lambda_D{}^o$ = Debye length at infinite diluted suspension (m)

σ = Surface charge density on silica particle (C/m^2)

ρ = Ionic density (m^{-3})

e = Primary charge on single electron (C)

r = Radius of colloidal particle (m)

At $[NaCl] \leq 10^{-5}$ mol/dm^3, the electrostatic repulsions (Figure 4.4a) overlap, which suggests that the particles volume fraction dominates. However, this repulsion starts decreasing when added [NaCl] reaches 10^{-4} mol/dm^3. At $[NaCl] = 0.1$ mol/dm^3, suspension becomes unstable and particles start to aggregate, which is confirmed by our sedimentation experiment (Figure 4.5) and previous work (Rödner, Wedin, and Bergström 2002). Similarly, minimum repulsion distance (D) calculated by DLVO theory

71

(Figure 4.4b) remains constant until $[NaCl] = 10^{-5}$ mol/dm^3 and decreases with further

NaCl addition ($D = 89$ nm at $[NaCl] = 10^{-4}$ mol/dm^3 and $D = 37$ nm at $[NaCl] = 10^{-3}$

mol/dm^3). At this small distance, other forces like disjoining pressure act more strongly

over electrostatic repulsion. If disjoining pressure is strong enough water film will break

(Sharma 1993; Sharma 1998) and particles might collapse on substrate before they reach

crystal front. To get better understanding, submonolayer deposition at various [NaCl] is

investigated. We observed the clear transition in submonolayer deposition from locally

ordered submonolayer at $[NaCl] \leq 10^{-5}$ mol/dm^3 to randomly packed submonolayer,

formed by separate clusters of particles at $[NaCl] = 10^{-4}$ mol/dm^3 (Figure 4.6). The locally

ordered submonolayer suggests the particles have approached crystal front by ballistic

deposition. On the other hand, random islands of particles suggest aggregation of particles

in thin film. These big clusters increase effective diameter of particle and cannot be pulled

to the crystal front as effectively as single particles by capillary forces, which leads to the

reduction of monolayer deposition velocity. Also these separate clusters form monolayers

with small domain sizes and increase the number of grain boundaries which result in

lower ρ and Ψ_6.
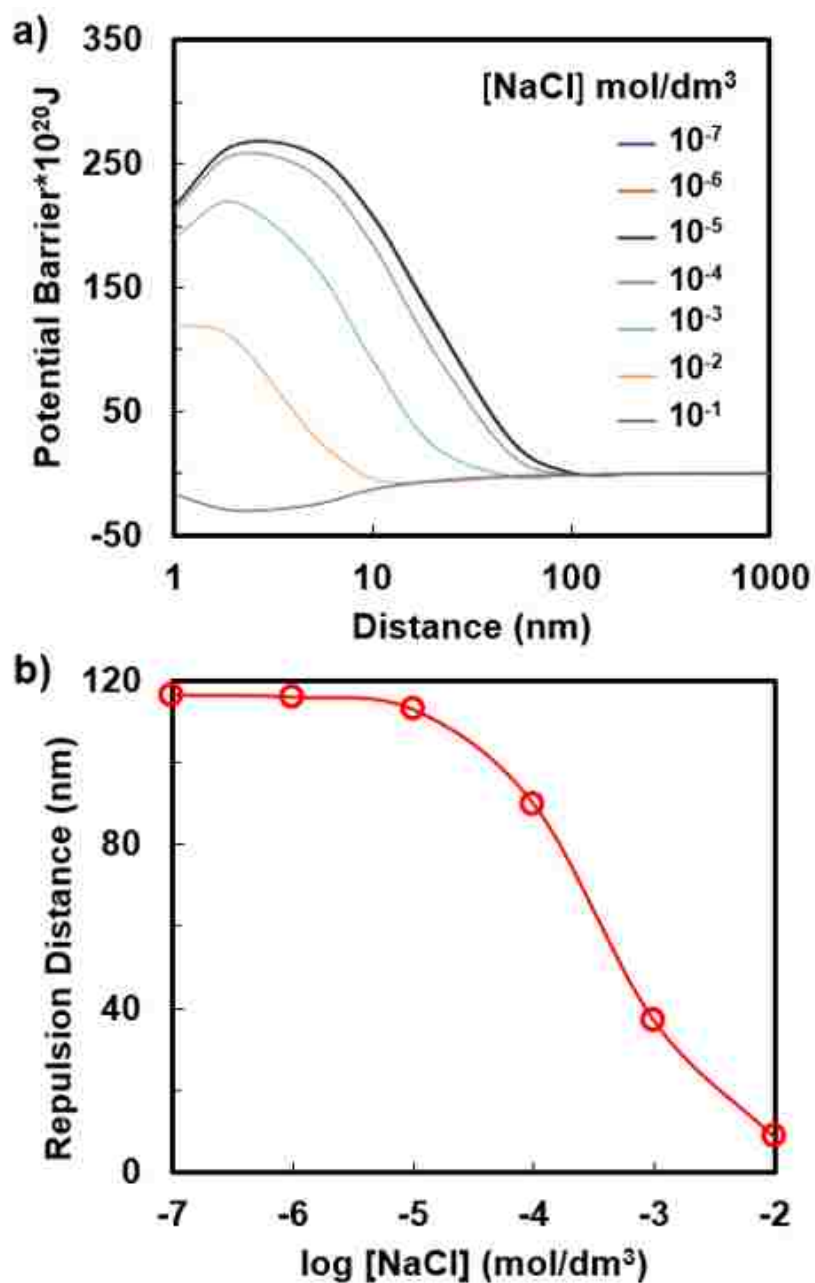
Figure 4.4: (a) Electrostatic barrier due to repulsive forces between particle-substrate interactions as a function of distance (nm). (b) Minimum separation distance (nm) due to electrostatic repulsion as a function of NaCl concentration (mol/dm^3). The calculation is courtesy of Kedar Joshi.
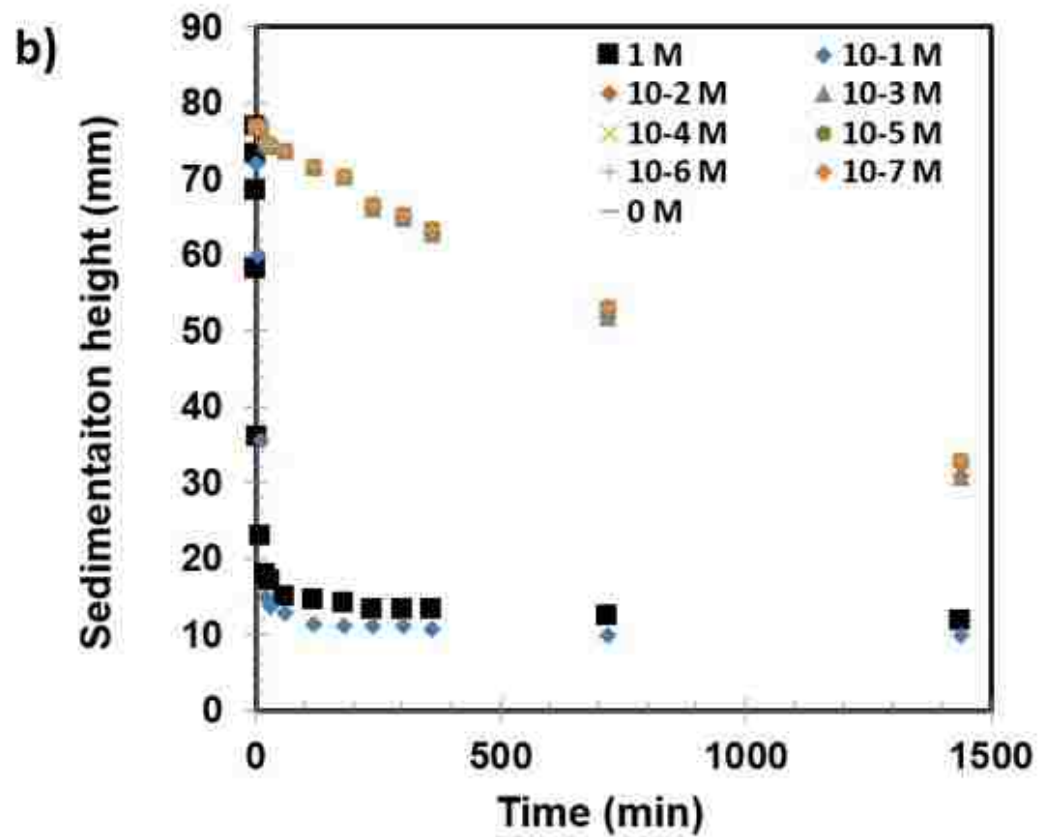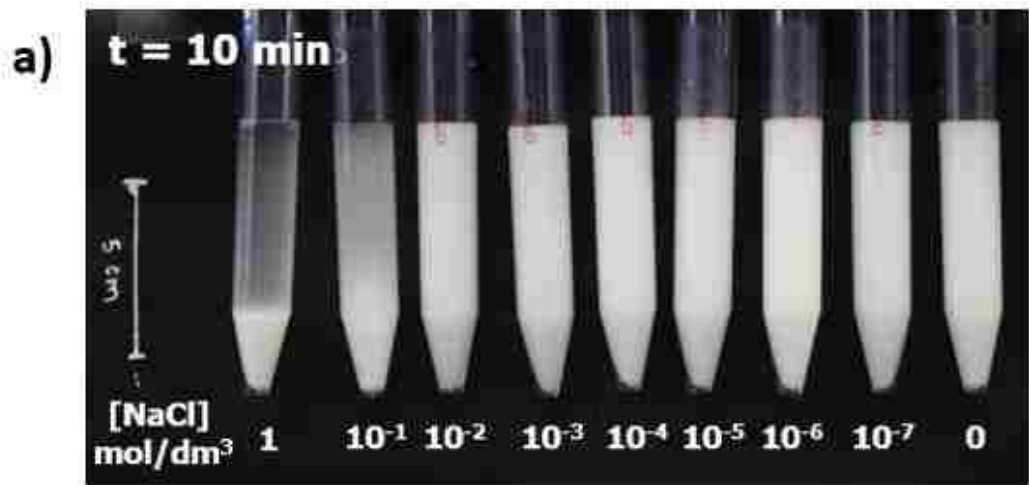
Figure 4.5: Sedimentation experiments showing (a) images of the suspension at different [NaCl] at t = 10 min, and (b) sedimentation height with respect to sedimentation time.
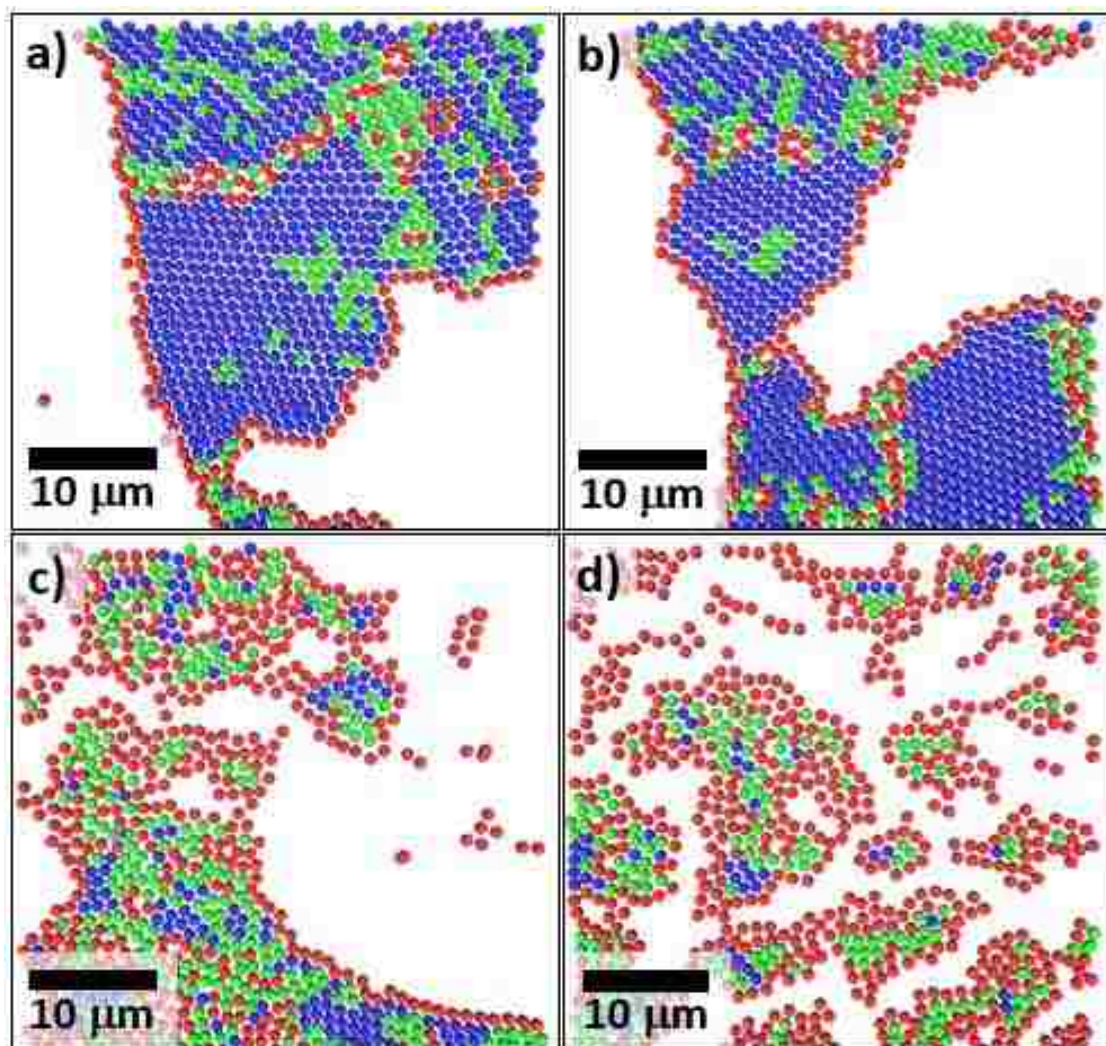
Figure 4.6: Rendering images of submonolayer deposited at (a) $[NaCl] = 10^{-7}$ mol/dm^3, (b) $[NaCl] = 10^{-6}$ mol/dm^3, (c) $[NaCl] = 10^{-5}$ mol/dm^3, and (d) $[NaCl] = 10^{-4}$ mol/dm^3.

4.2.2 Effect of Surface Charge on Convective Deposition

      Unlike an addition of salt, the addition of NaOH simultaneously alters both ionic strength and surface charge. With an increase in surface charge, as expected, we observe the enhancement of monolayer deposition. As depicted in Figure 4.7a, at $[OH^-] = 10^{-7}$ mol/dm^3 (no NaOH added), the monolayer condition exists at $v_w = $ 75-78 μm/s. The range of monolayer deposition velocity increases by 700% at $[OH^-] = 10^{-5}$ mol/dm^3. However, this range again decreases at higher $[OH^-]$. Here surface charge plays an important role in a stability of colloidal particles. With an increase in $[OH^-]$, surface charge increases as previously described in the zeta potential measurement (Figure 4.1). At $[OH^-] \leq 10^{-5}$ mol/dm^3, minimum repulsion distance remains constant (Figure 4.4) as particles screening themselves; however, additional surface charges from OH$^-$ leads to stronger repulsion force between particles and substrate. Particles may have extra time to rearrange themselves within the liquid thin film resulting in higher ρ and Ψ_6. At $[OH^-] > 10^{-5}$ mol/dm^3, although particles gain additional surface charge, minimum repulsion distance decreases which brings particles closer to each other. This results in the shrinkage of monolayer region.

      In this study the expansion of monolayer deposition region is mainly found on slower velocity side (Figure 4.7a). At the lower deposition velocities, the particle flux from the meniscus to thin film is more than the particle flux needed for monolayer deposition which is governed by water evaporation rate. In order to get monolayers at such speed the thin film length has to be reduced by changing deposition blade angle

(Kumnorkaew et al. 2008), which will decrease the evaporation flux, or particles have to suspend in the thin film longer by additional electrostatic repulsion forces.

Figure 4.7b presents experiments performed at fixed ionic strength $[I] = 10^{-3}$ mol/dm^3 and varied [OH$^-$]. With increasing surface charge, not only the expansion of monolayer region but also the improvement in the order of monolayer is noticeable. Again, in order to identify the effect of particle surface charge, microstructure analysis of submonolayer deposition is examined. As expected, we observed the transition from random to locally ordered submonolayer as confirmed in Figure 4.8.
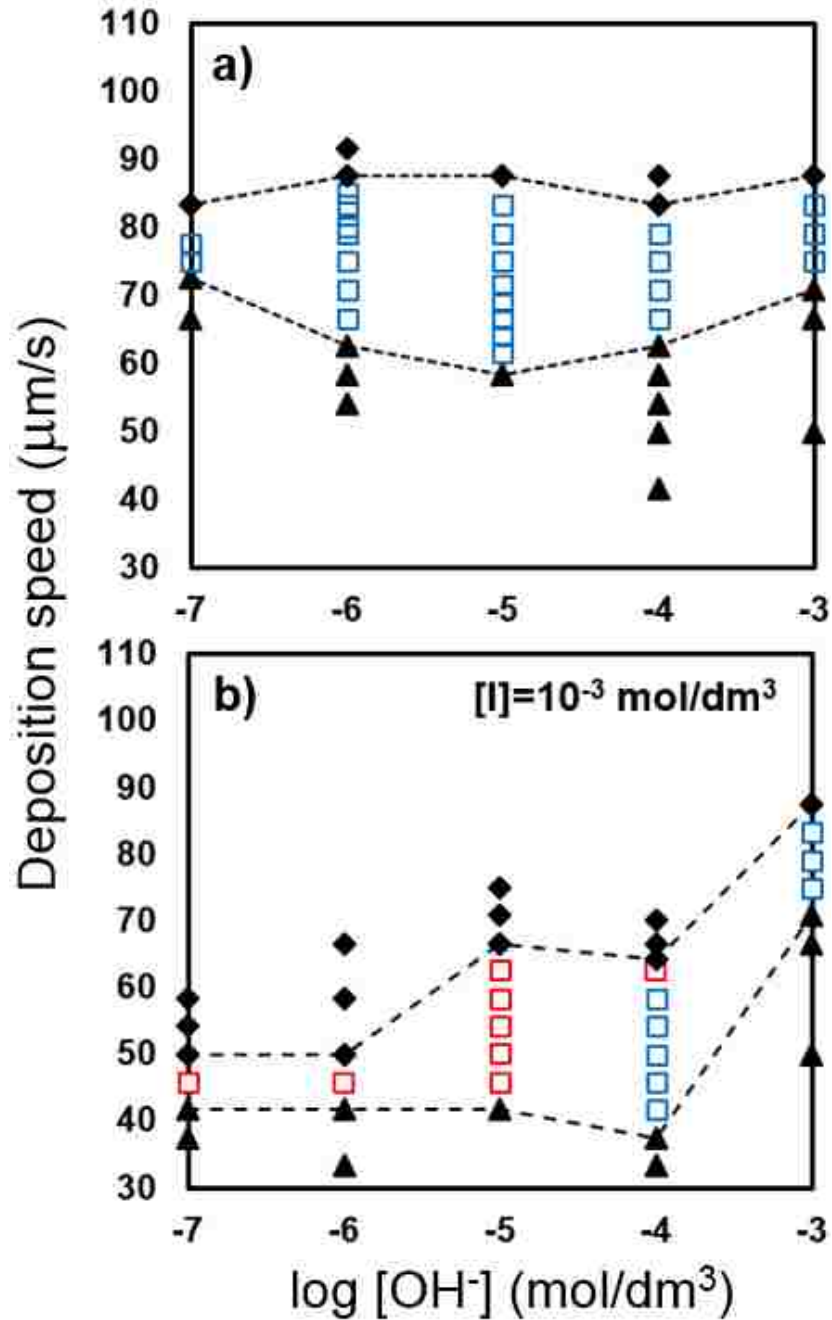
Figure 4.7: Phase diagrams showing (a) monolayer deposition velocity (μm/s) as a function of [OH⁻], and (b) monolayer deposition velocity (μm/s) as a function of [OH⁻] at fixed ionic strength $[I] = 10^{-3}$ mol/dm³. Triangles show multilayer deposition. Diamonds show submonolayer deposition. Red rectangles show monolayer deposition with $0.70 < \rho < 0.75$ and $\Psi_6 \geq 0.575$. Blue rectangles show monolayer deposition with $\rho \geq 0.75$ and $\Psi_6 \geq 0.575$.
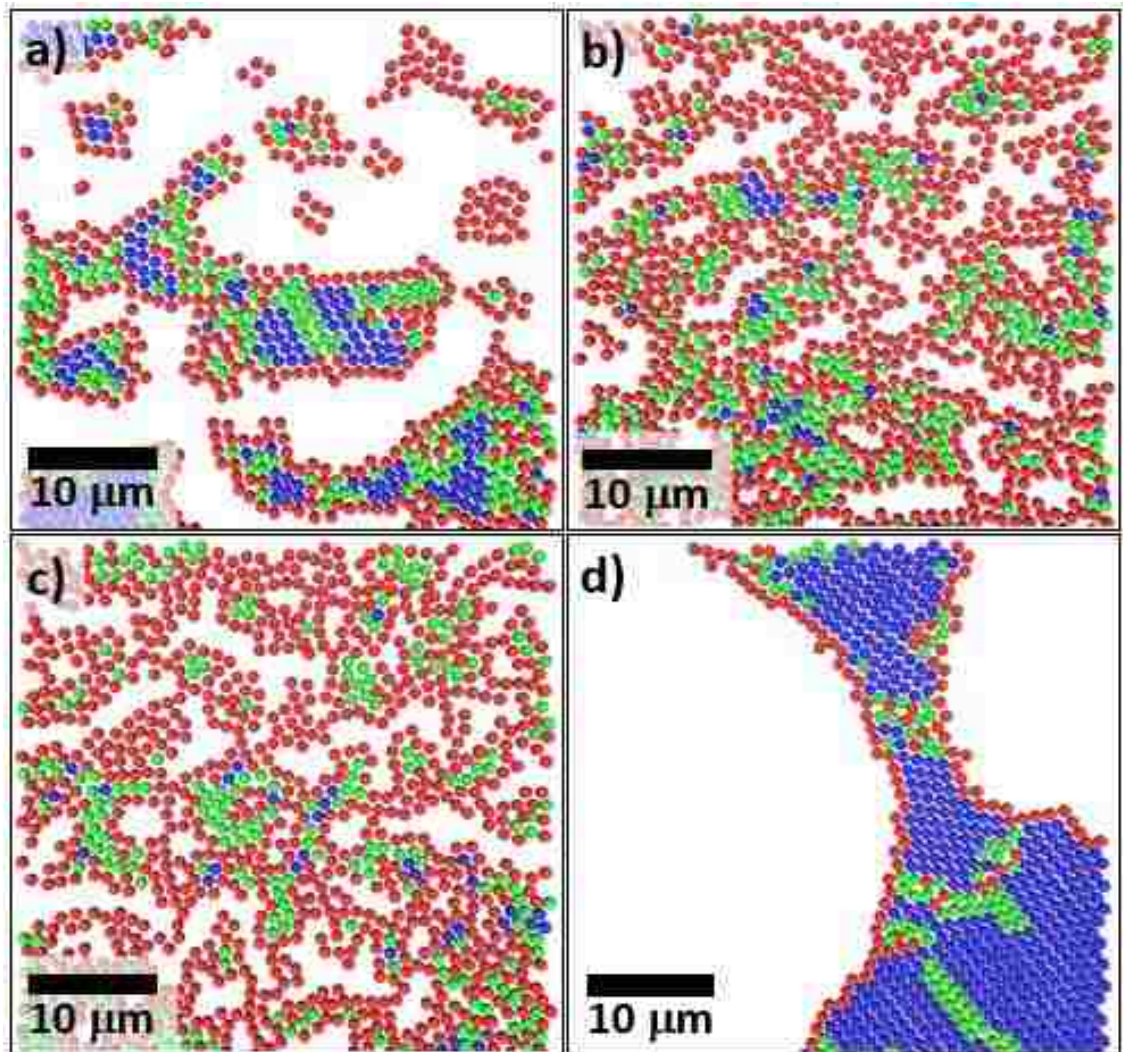
Figure 4.8: Rendering images of submonolayer deposited at constant $[I] = 10^{-3}$ mol/dm^3 and (a) $[OH^-] = 10^{-7}$ mol/dm^3, (b) $[OH^-] = 10^{-6}$ mol/dm^3, (c) $[OH^-] = 10^{-5}$ mol/dm^3, and (d) $[OH^-] = 10^{-4}$ mol/dm^3.

4.3 Conclusions

   Ionic strength and surface charge play vital role in determining nature of particle morphology in convective assembly. The basic mechanism of particle deposition at micro-level is governed by particle-particle and particle-substrate interactions. Presence of salt brings particles closer due to increasing in ionic strength, which results in pre-organized deposition and particle island formation. These particle islands lead to lower packing density and local order in monolayer depositions. On the other hand, an increase in surface charge results in the enhancement in monolayer depositions due to additional electrostatic repulsion forces.

Chapter 5

Preliminary Investigations of Marangoni Effect on Convective Deposition

5.1 Introduction

Two-dimensional (2D) colloidal crystals obtained from the convective deposition (Kumnorkaew et al. 2008; Prevo and Velev 2004; Dimitrov and Nagayama 1995; Yamaki, Higo, and Nagayama 1995) of colloidal silica particles are formed through capillary force and convective evaporation. Silica monolayers achieved via convective deposition have great usages as coatings on optical technologies, including LEDs (Ee et al. 2007; Kumnorkaew et al. 2008) and DSSCs, as well as biological technologies, including immunoaffinity diagnostic tools (Wang et al. 2011) and viral filtration membranes (Weldon et al. 2012). However, these depositions are prone to imperfections that cannot be controlled during the deposition process. This causes many issues during scale-up and creates inefficiencies.

Instability-driven "streaks" can nucleate and progress through the sample length (Figure 5.1). In this chapter "streaks" is defined as multilayers with more than 7 layers.

These macroscale defects are most likely a product of surface tension-driven flow (Brzoska, Shahidzadeh, and Rondelez 1992; Bertozzi and Brenner 1997; Kataoka and Troian 1997). Unless treated with a form of stabilization such as surfactants (Kleinert, Kim, and Velev 2010), nanoparticles (Kumnorkaew and Gilchrist 2009; Kumnorkaew, Weldon, and Gilchrist 2010) or applied mechanical vibration (Muangnapoh, Weldon, and Gilchrist 2013), random, uncontrollable multilayer streaks will form during the deposition process. The location, size, and thickness of these streaks have no modeled pattern and are believed to be caused by micro-level evaporating conditions not being uniform across the entire substrate.

The Marangoni effect is observed in surface transport when there exists a surface tension gradient. This surface tension gradient will cause a flow of the fluid from lower surface tension to higher surface tension. In this study, the concentration gradient is caused by the difference in surface tension between the region with higher ethyl alcohol concentration (meniscus) and lower ethyl alcohol concentration (thin film); a similar case exists in many wines causing wine to flow up the sides of the glass in the direction of the surface tension gradient causing rings around the glass, hence "tears of wine" (Thomson 1855; Hosoi and Bush 2001). Here this study focuses on solving the inherent problem of uncontrollable multilayer streaks that form during normal convective deposition of silica particles by the addition of ethyl alcohol (EtOH) as well as studying the Marangoni effect that persists in this EtOH-water system.
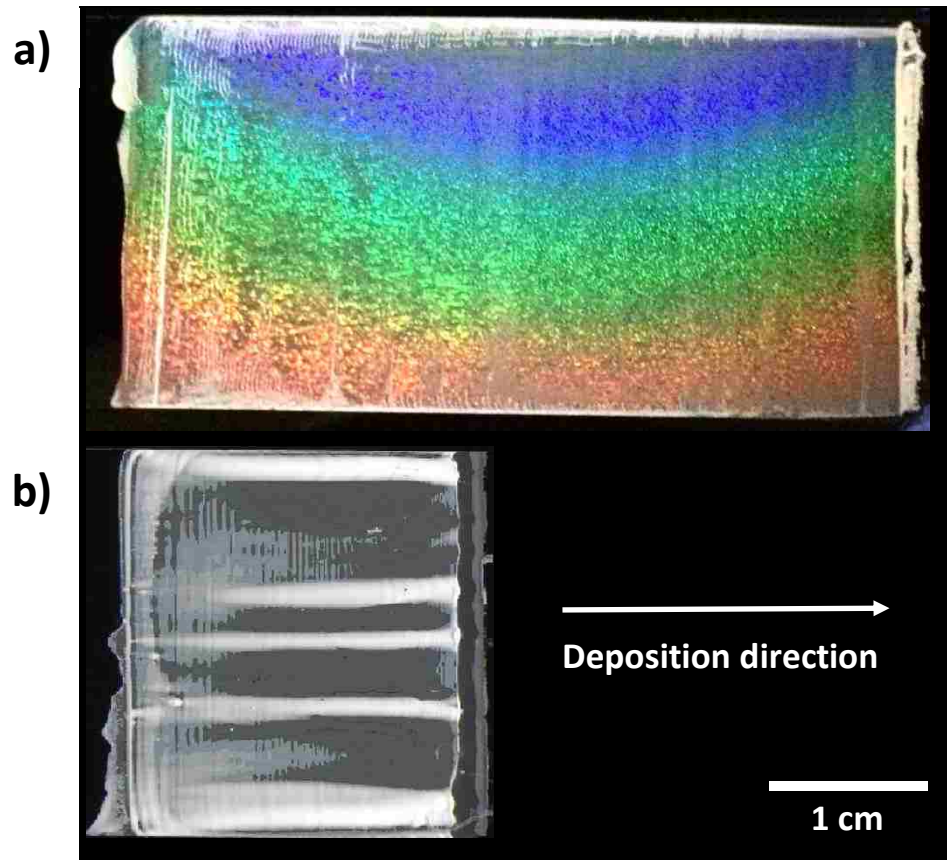
Figure 5.1: (a) Successfully deposited silica monolayer with no instabilities or streaks. (b) Silica coating that exhibits random, uncontrollable multilayer streaks.

5.2 Experimental Results and Discussion

5.2.1 Marangoni Flows in EtOH-Water Based Silica Suspension: Droplet Experiments

The driving forces behind Marangoni flows are, for the purposes of this study, temperature and EtOH concentration generating surface tension gradients. As shown in Figure 5.2, untreated silica suspension droplets illustrate the "coffee ring effect" (Deegan et al. 1997) in which the silica particles will collect at the edge of the droplet during evaporation causing the greatest concentration at the edge of the dried ring and a very low concentration in the middle. Across all temperatures, this was observed without much deviation. Once EtOH was added, significant drop spreading occurred due to the presence of Marangoni flows. Fingering instabilities (Troian, Wu, and Safran 1989) were observed especially when the concentration of EtOH is between 30-50 %V. At lower temperatures the droplet retained its circular shape, however at higher temperatures the shape of the droplet became highly irregular as a result of the combination of Marangoni-driven spreading and fingering instabilities at the edge of the advancing meniscus. At high concentration, the evaporation again dominates over the Marangoni flow resulting in the dried ring with higher concentration at the edge.

Figure 5.3 represents three distinct phases of evaporating EtOH-water based silica suspension at 30 %V EtOH. This result shares some similarities to previous studies (Hamamoto, Christy, and Sefiane 2012; Innocenzi et al. 2008) where three distinct phases of evaporation were investigated. However, in their work, no fingering instability was observed. It is noted that they studied the flow characteristics of evaporating EtOH-water

84

droplet only at 5 %V EtOH. In our work, at initial condition (Figure 5.3a), t = 0 s, the 3-μl droplet of suspension is placed onto a piranha-treated glass substrate resulting in the circular droplet with a diameter of 0.4 cm. In the first phase, significant drop spreading and fingering instabilities occurred all around the droplet as a result of Marangoni flow (Figure 5.3b). This results in an expansion of the drop to roughly 1.7 cm. In the second phase, starting from the edge to the center, the first drying boundary suggesting the evaporation of EtOH is noticeable (Figure 5.3c). This phase takes place around 12 seconds. In the last phase where water evaporates (Figure 5.3d), the rate of water evaporation is roughly 2 times slower than the second phase.
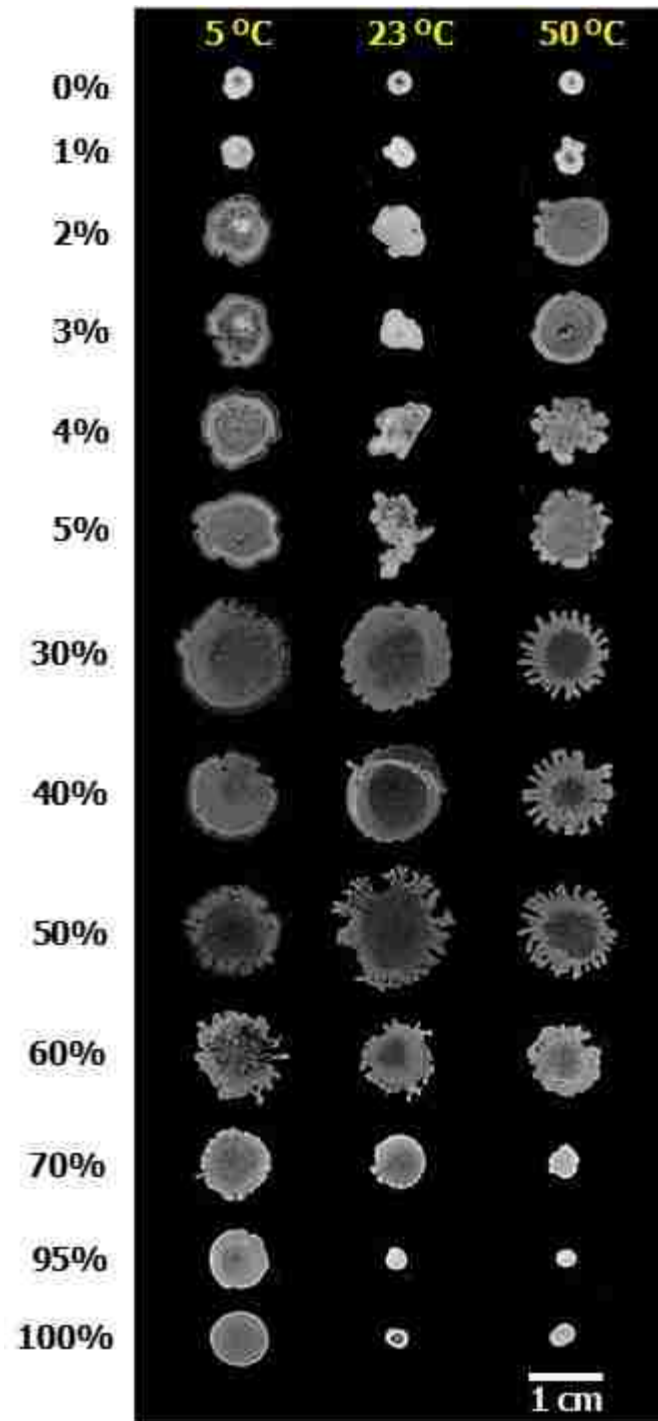
Figure 5.2: Photograph showing the effects of temperature and concentration of EtOH on suspension droplet spreading.
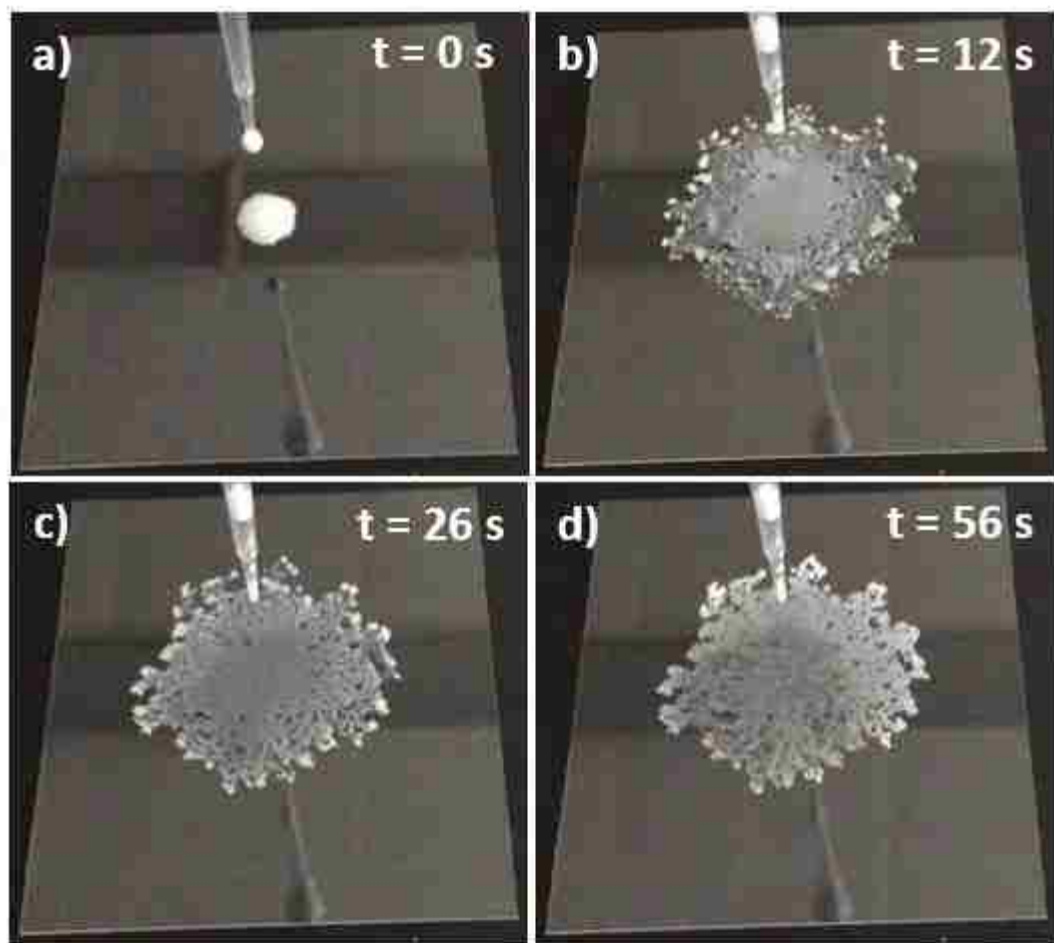
Figure 5.3: Three distinct phases of evaporating EtOH-water based silica suspension: (a) initial droplet, (b) Phase I: droplet spreading due to Marangoni flow and fingering instability, (c) Phase II: EtOH evaporation, and (d) Phase III: water evaporation.

5.2.2 Effect of EtOH Concentration on Convective Deposition

In this set of experiments, the deposition velocity is manipulated at $v_w = 400\text{-}700$ μm/s which is roughly 10 times faster than traditional convective deposition (water-based suspension). The area of monolayers (%) is plotted with respect to EtOH concentration (%V) as depicted in Figure 5.4. For all of these experiments, no streak has been observed in the middle of sample. For low EtOH concentration, 1-5 %V (not shown in Figure 5.4), the suspension is pulled toward the beginning part of deposition due to the surface tension gradient resulting in thick multilayer deposition (more than 7 layers) on the beginning part of sample. Moreover, wavelike patterns, which are double or triple layers, are commonly observed throughout the whole sample (Figure 5.5). At 10 and 20 %V EtOH, the results are similar to those samples of 1-5 %V EtOH. The thick multilayer deposition (more than 7 layers) in the beginning part are occupied around 15% of the whole sample area. Monolayers are less than 10%. The rest of sample is a combination of submonolayers and multilayers (less than or equal to 7 layers). Interestingly, between 30-50 %V EtOH, the significant increase in monolayers is noticed. The obtained monolayers are at least 45% regardless of deposition velocity. Periodic stripes (Figure 5.6) within submonolayer region suggest a strong influence of Marangoni flows on a convective deposition. At higher EtOH concentration (more than 50 %V), due to high evaporation rate of EtOH, more than 90% of the whole sample area is multilayers.
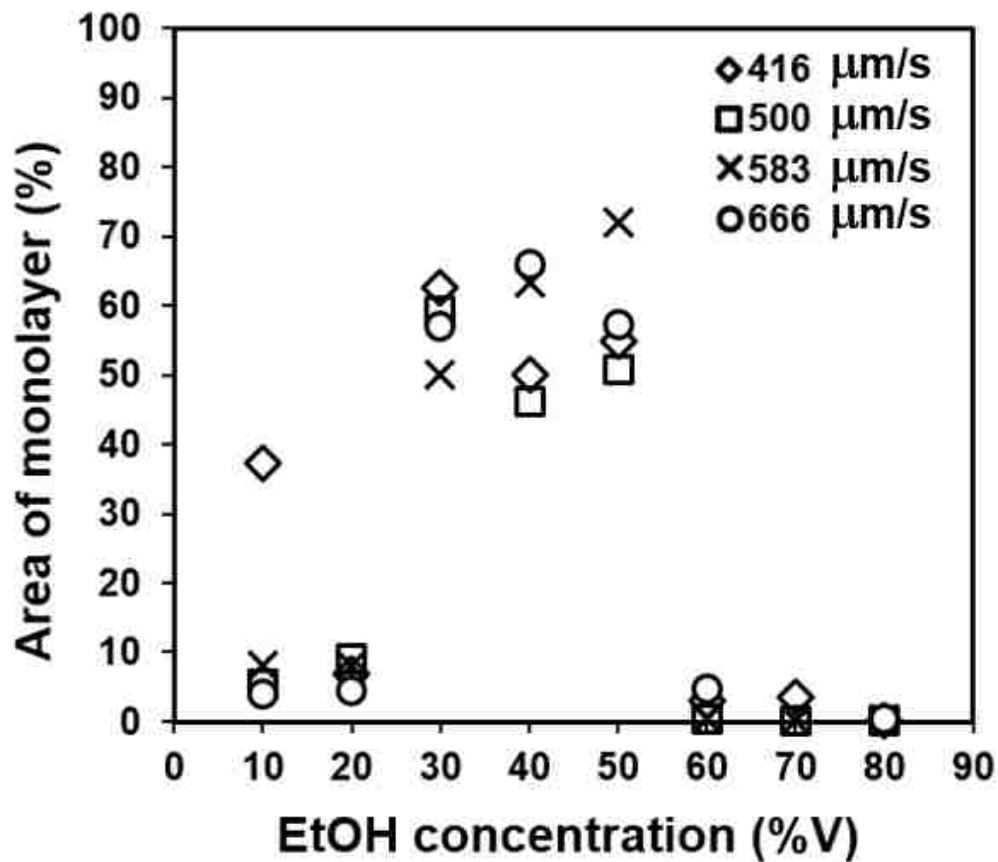
Figure 5.4: Graph showing the area of monolayer (%) as a function of EtOH concentration (%V).
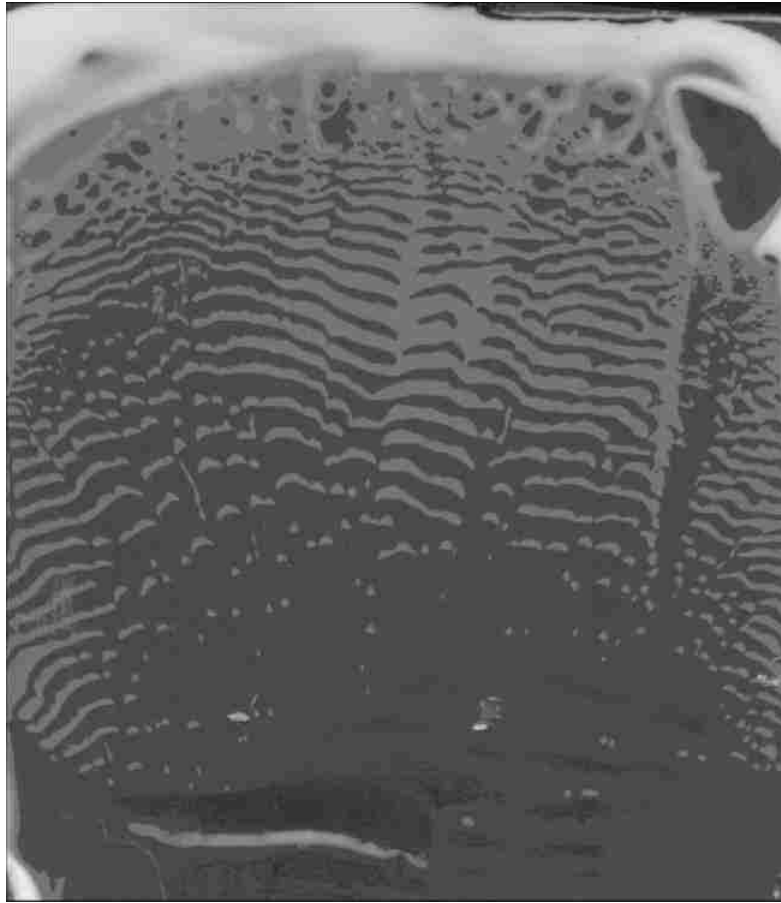
Figure 5.5: Photograph of the deposited sample using 3% EtOH suspension. Thick region at the beginning of sample is due to Marangoni flow. Wavelike patterns are observed throughout the whole sample.
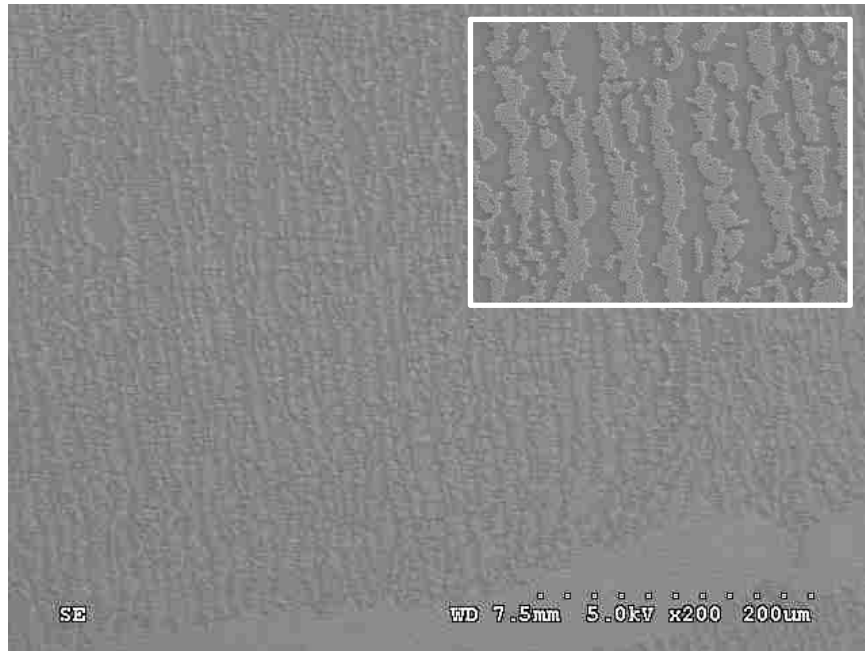
Figure 5.6: Scanning electron microscopy images showing periodic stripes within submonolayer region. The sample is deposited at $v_w = 583$ μm/s using 40% EtOH suspension.

5.3 Conclusions

This study focuses on controlling instabilities via manipulating the meniscus flow by adding ethyl alcohol (EtOH) into the silica microsphere and water suspension. Nonuniform evaporation of EtOH results in a flow similar to that which is attributed to the formation of "tears of wine". This phenomena had been shown by our data to have an appreciable impact on these instabilities and thus can be employed in scale-up procedures to achieve better coatings of silica monolayers.

Chapter 6

Applications and Potential Studies

6.1 Chapter Overview

This chapter presents applications and potential studies which have considerably utilized vibration-assisted convective deposition (previously described in Chapter 3) in their processes. First, we present a simple method of making colloidal microlens arrays from binary suspension of silica (SiO_2) and polystyrene (PS) particles. PS thickness can be precisely controlled using either oxygen reactive ion etching (RIE) or additional deposition of PS suspension (section 6.2). These microlens arrays can be used in many applications including enhancing the light extraction efficiency of InGaN quantum-well light-emitting diodes (section 6.3) as well as making Iradium-capped Janus particles (section 6.4). Second, we demonstrate a potential application using uniform PS multilayers assembled by vibration-assisted convective deposition. These PS multilayers can be used as templates to make magnesium oxide (MgO) membranes for battery separator layers (section 6.5).

6.2 Development of Colloidal Microlens Arrays with Various Aspect Ratios

In this study we demonstrate a use of vibration-assisted convective deposition to fabricate SiO_2/PS microlens arrays with various aspect ratios. Binary suspension of 1-μm SiO_2 particles ($\phi_{SiO_2} = 0.2$) and 75-nm PS particles ($\phi_{PS} = 0.08$) is used in all experiments. First, the deposition of well-ordered microsphere monolayers from binary suspension is performed at $v_w = 70$ μm/s, $\omega = 50$ Hz, $A_0 = 248$ μm, and blade angle of 45°. Next, the sample is heated at 240 °C for 5 minutes to melt PS particles. The initial thickness of PS layer is 650 nm as illustrated in Figure 6.1a. The thickness of the PS layer can be manipulated by two methods:

1) Oxygen reactive ion (plasma) etching

2) Additional deposition of PS suspension

Reactive ion etching (RIE) is commonly utilized in colloidal lithography (Choi et al. 2004; Cong et al. 2009; Ji et al. 2011). Recently, RIE has been reported to use for size-reduction of colloidal spheres (Cong et al. 2009). Here in this study, we use oxygen RIE in order to precisely reduce the thickness of PS layer. Figure 6.2 presents the thickness of PS layer as a function of time of oxygen RIE. The oxygen RIE is performed in oxygen plasma generator (Prof. Xuanhong Cheng's lab, Lehigh) at radio frequency (RF) power of 50 W. The thickness of PS layer is reduced to 580, 480, 260 and 0 nm under oxygen RIE time of 1.5, 2.5, 5.0, and 7.0 minutes, respectively (Figure 6.1 b-e).
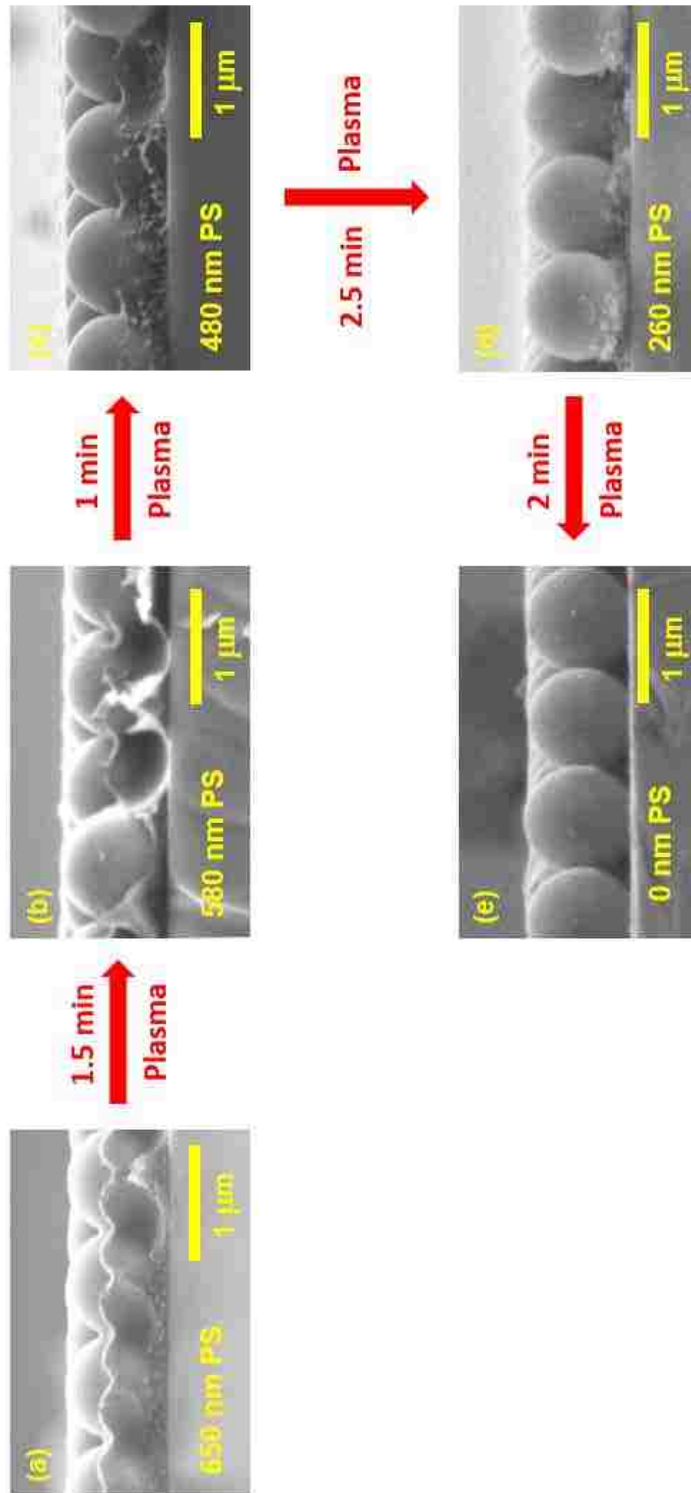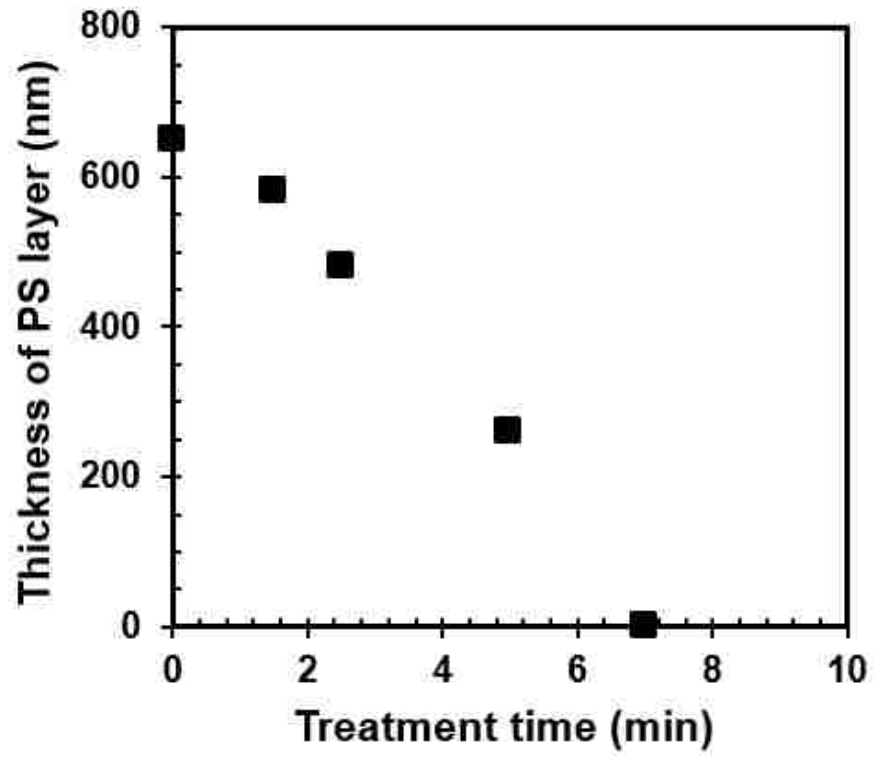
Figure 6.2: Thickness of PS layer as a function of oxygen RIE time.

On the other hand, to increase the thickness of PS layer, the additional deposition of PS suspension is required. First, SiO_2/PS microlens arrays with PS thickness of 650 nm is prepared as described above. Next, the sample is put into a furnace at 500 °C for 30 minutes to completely burn PS off (Figure 6.3b). Then the additional deposition of 4 %V PS suspension is performed at v_w = 50 μm/s on top of SiO_2 monolayers. After deposition, the sample is again heated at 240 °C for 5 minutes. The resultant PS thickness is 1 μm (Figure 6.3c). It is important to note that PS thickness can be accurately manipulated by either varying deposition velocity or concentration of PS suspension.
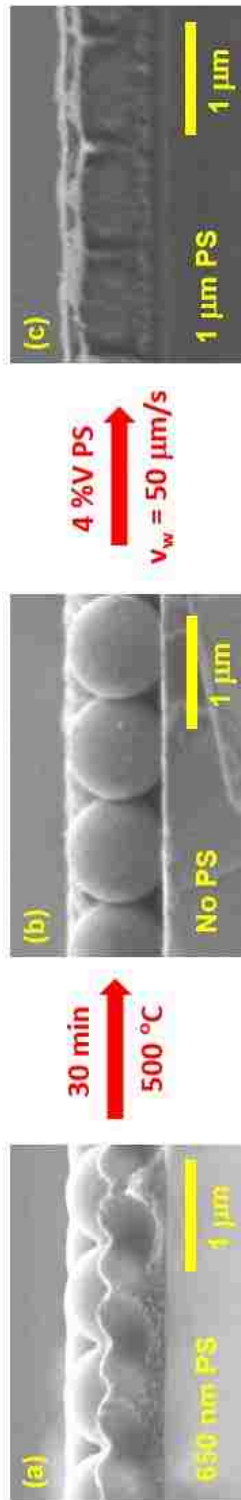
6.3 Application: Enhancement in light extraction efficiency of InGaN quantum-well light-emitting diodes (LEDs)

In collaboration with Prof. Nelson Tansu (Lehigh), SiO_2/PS microlens arrays with various aspect ratios are deposited on top of InGaN quantum-well light-emitting diodes (LEDs). The electroluminescence (EL) measurements performed by Tansu group are shown in Figure 6.4. At $\theta = 0^{\circ}$ (normal direction) and current density of 80 A/cm^2, the microlens LEDs with PS thicknesses of 0 nm, 250 nm, 650 nm, and 810 nm show 2.40, 2.60, 2.03, and 1.96 times improvement in the integrated power, respectively. Additionally, at $\theta = 45^{\circ}$ (oblique direction) and same current density, the microlens LEDs with PS thicknesses of 0 nm, 250 nm, 650 nm, and 810 nm show 2.19, 2.80, 3.27, and 3.18 times improvement in the integrated power. The light extraction efficiency of LEDs is increased due to the reduced Fresnel reflection, enlarged photon escape cone and enhanced photon scattering (Li et al. 2011).
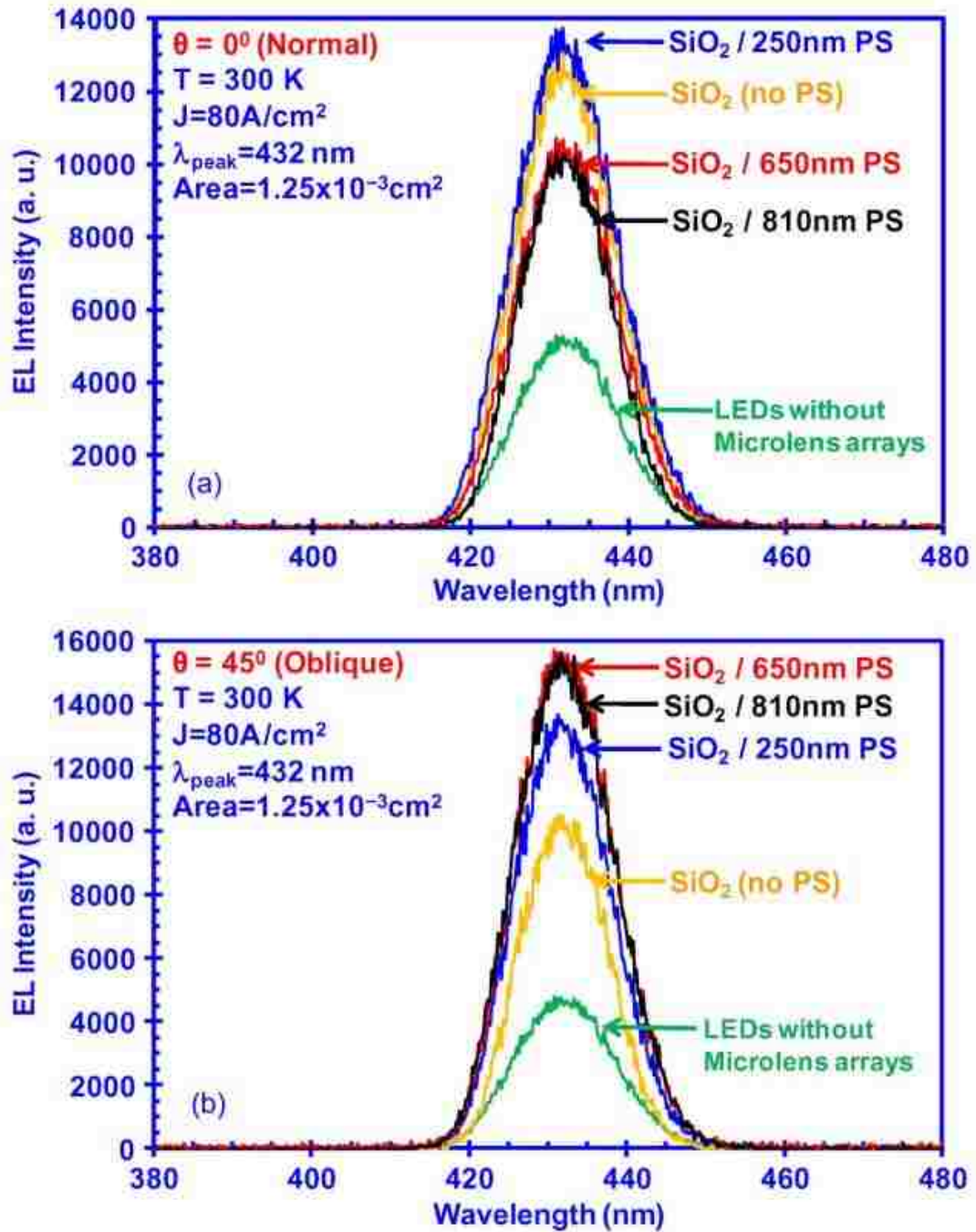
Figure 6.4: EL spectra of InGaN QW LEDs emitting at 432 nm of SiO_2/PS microlens arrays with various PS thickness measured at (a) $\theta = 0°$, and (b) $\theta = 45°$ (Li et al. 2011).

6.4 Potential Study: Convective Deposition for Making Janus Particles

Here we demonstrate a potential application using SiO_2/PS microlens arrays for making Janus particles. Similarly, SiO_2/PS microlens arrays with desired PS thickness is firstly prepared using methods in section 6.2. Next, sputter coating of Iridium (Ir) is performed. Finally, the sample is put into a furnace at 500 °C for 30 minutes to completely burn PS off. SEM image of Iridium-capped silica particles and X-ray energy-dispersive spectroscopy (XEDS) analysis are shown in Figure 6.5.
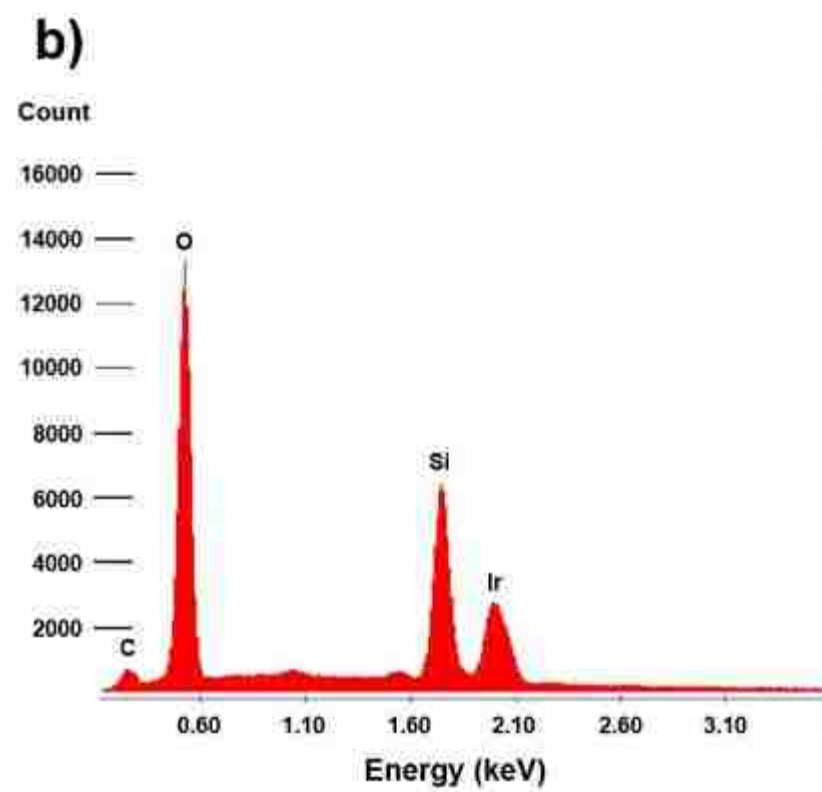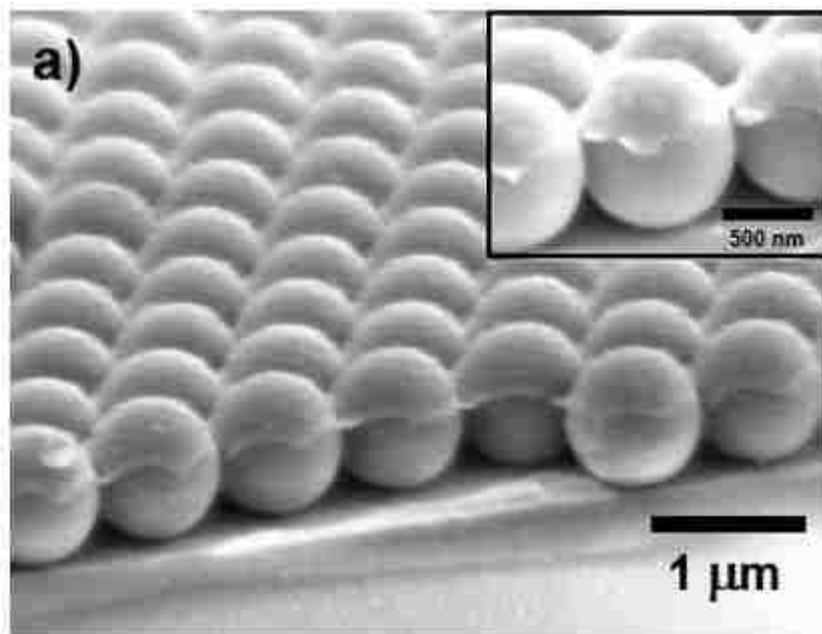
Figure 6.5: (a) SEM images of Iridium-capped silica particles and (b) XEDS analysis.

6.5 Potential Study: Magnesium Oxide Membrane for Battery Separator Layers

The goal of this study is to produce magnesium oxide (MgO) membrane to carry electrolytes and separate anode and cathode layers in batteries. Desired properties of membrane are listed: (1) Porous (small pore size to hold electrolyte), (2) Permeable to ion flow (minimal ionic resistance), (3) Mechanically strong, (4) Chemically stable, and (5) Easy to scale up. However, handling MgO is a challenging task since the density of MgO is high (ρ_{MgO} = 3.6 g/cm^3). Moreover, MgO is not stable and preferably reacted with water to become Mg(OH)$_2$ as shown Figure 6.6. The reaction of MgO and water is described in the following reaction.

$$MgO + H_2O \rightarrow Mg(OH)_2$$
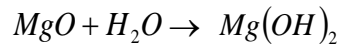
Here in this study 35-nm MgO particles (Inframat Advanced Materials) are dispensed in EtOH (200-proof). Alkali lignin (Sigma-Aldrich) is used as a stabilizing agent. Agglomerated MgO particles are separated using sedimentation. The liquid part is used as stock suspension for all experiments. Two approaches of making MgO membranes have been studied. First, a separate colloidal suspension of 600-nm polystyrene spheres (Thermo Scientific) is mixed with stock MgO suspension to achieve the desired suspension composition. This suspension is deposited onto piranha-treated glass substrate using vibration-assisted convective deposition. After deposition, the sample is put into a furnace at 500 ˚C for 30 minutes to completely burn off PS nanospheres and alkali lignin. MgO layers with randomly distributed pores are observed under scanning electron microscopy (Figure 6.7). However, these pores are not interconnected and MgO layers are loosely stuck to the substrate.

For the second approach, the multilayers of 600-nm PS particles prepared by vibration-assisted convective deposition are used as a scaffold for the infiltration of MgO suspension. The stock MgO suspension is deposited on top of PS multilayers. We noticed that MgO particles cannot penetrate through PS multilayers (regardless of deposition velocity) and form a layer on PS multilayers (Figure 6.8). Also, positively-charged PS particles have been used in this experiment; however, the result is similar.

In summary, the fabrication of MgO membrane for battery separator layers is not yet completed due to a problem in the infiltration process. In the future, magnesium nitrate hexahydrate will be used as magnesium precursor for infiltration into PS multilayers. MgO products will be generated by calcination at 600 $^{\circ}$C for 8 hours (Li et al. 2004).
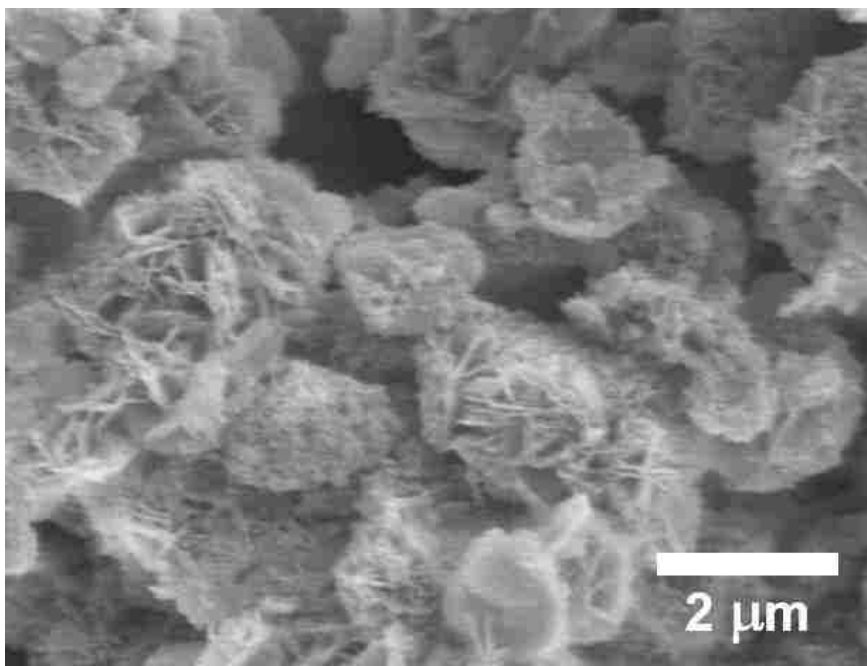
Figure 6.6: SEM image of Mg(OH)$_2$ particles formed by the reaction of MgO and water.
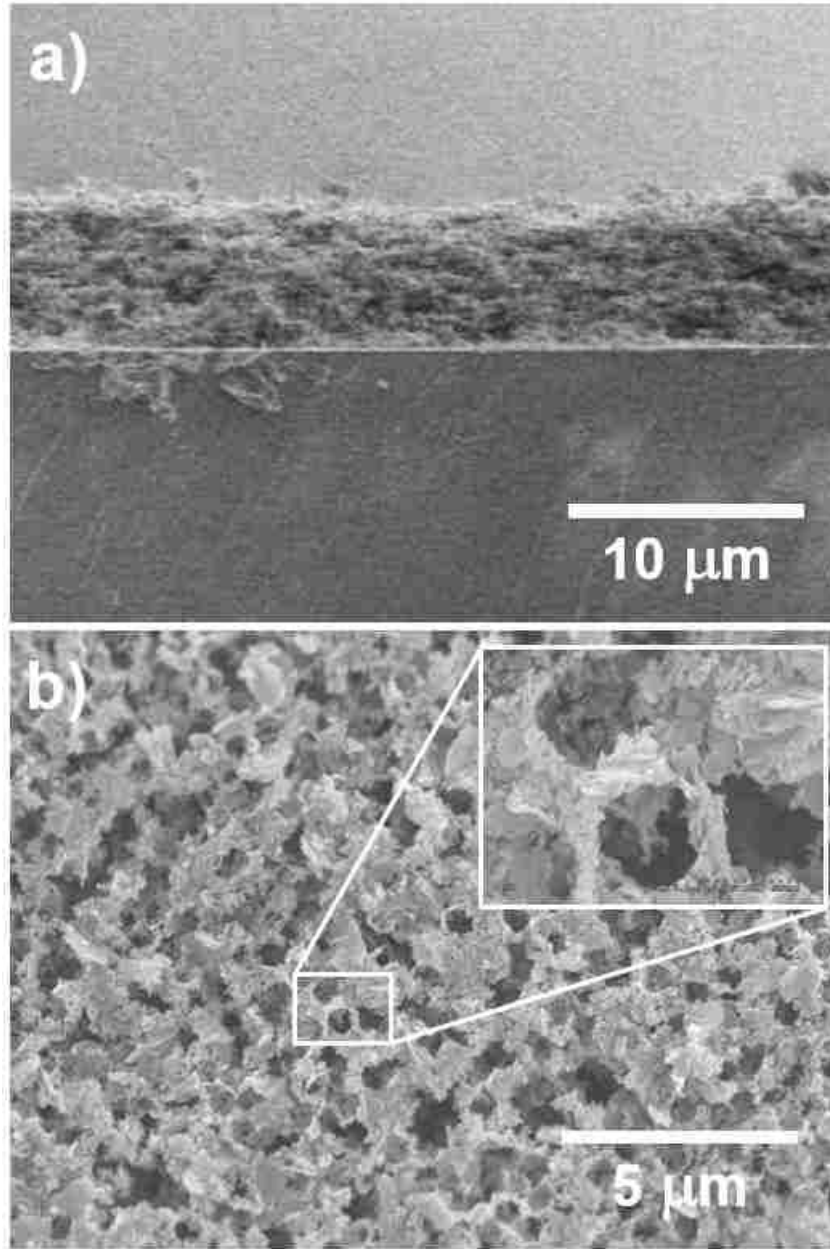
Figure 6.7: (a) Cross-sectional SEM image of 6-μm MgO layer deposited by the mixture of MgO and PS and (b) top-view SEM image showing randomly distributed pores throughout the whole samples.
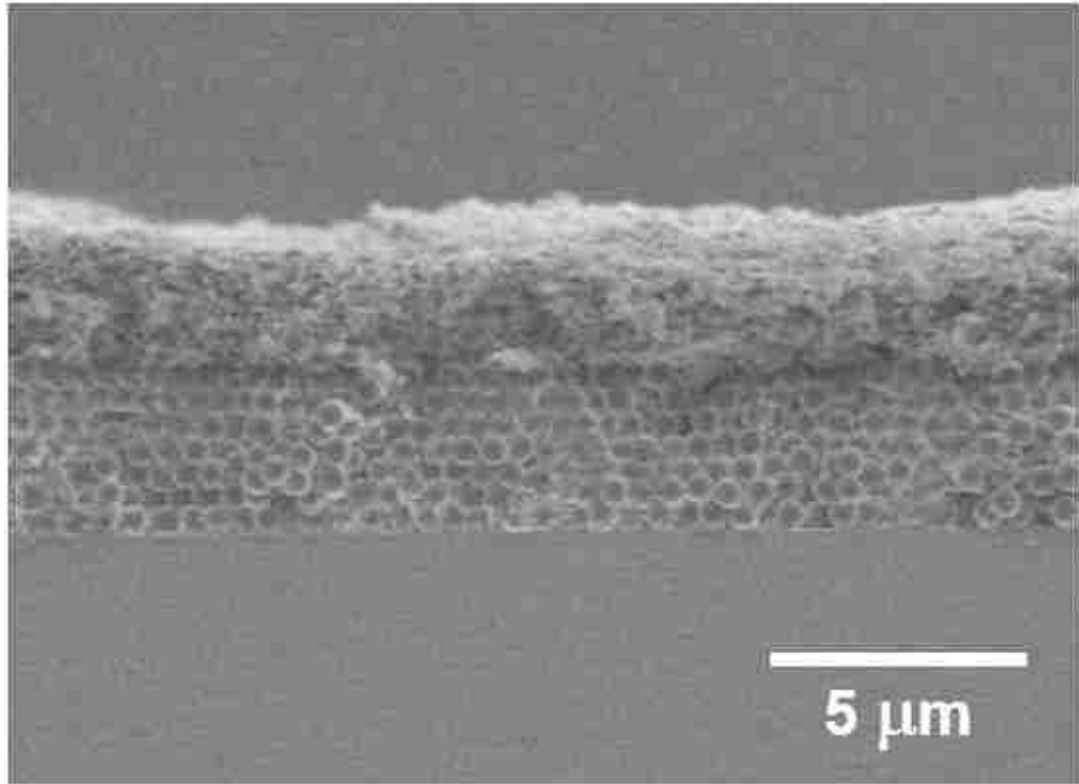
Figure 6.8: Cross-sectional SEM image showing MgO layer on top of a PS multilayer.

6.6 Conclusions

Vibration-assisted convective deposition is an advanced technique to assemble uniform SiO_2/PS microlens arrays with high microstructure order. These SiO_2/PS microlens arrays can be used in many applications including material engineering, biotechnology and energy-related applications. Here, we develop two methods to accurately manipulate PS thickness between 0-1 μm. First, oxygen reactive ion (plasma) etching can be used for decreasing PS thickness. The result shows that the thickness of PS linearly decreases with increasing plasma treatment time. Second, an increase in PS thickness can be performed by the additional deposition of PS suspension. The resulting PS thickness is dependent of deposition velocity and concentration of PS suspension. Moreover, we demonstrate a use of these SiO_2/PS microlens arrays for enhancing the light extraction efficiency of InGaN quantum-well light-emitting diodes (LEDs). After fabricating SiO_2/PS microlens arrays on top of mentioned LEDs, the light extraction efficiency is increased by 2-3 times depending on PS thickness. Besides, we present couple potential studies which are required vibration-assisted convective deposition in their processes.

Chapter 7

Summary and Future Outlook

7.1 Summary

Convective deposition is a promising technique to fabricate relatively large, well-ordered particles microstructure. This combines two phenomena where particles flow to the contact line of a meniscus as a result of the evaporative flux, then order through capillary forces. However, natural defects such as point defects, line defects, grain boundaries, and streaks can nucleate uncontrollably throughout the sample. This thesis focuses on the improvement of convective deposition to suppress undesirable instabilities and defects.

The application of lateral vibration of the substrate is significant process enhancement in convective deposition. This technique not only suppresses instabilities and defects but also increases formation rates of deposited particles. Besides, it significantly improves process robustness by allowing the deposition of monolayers under a wide range of deposition velocities. These enhancements are a result of the deformation of air-liquid interface during the deposition. This deformation create pressure variations within the thin film which significantly change the flow profile and

109

introduce lubrication forces into the system. In addition, this technique is applicable for many applications including enhancing the light extraction efficiency of InGaN quantum-well light-emitting diodes, fabrication of MgO membranes for battery separator layers and fabrication of complex materials such as Janus particles.

Particle surface charges and ionic strength of medium are important parameters which have never been taken into account in convective deposition. The addition of salt increases the ionic strength and reduces the thickness of the electric double layers, which leads to particle clusters formation during deposition. On the contrary, the addition of NaOH increases particle surface charges and gives extra electrostatic repulsion forces between particle-particle and particle-substrate. The result shows the expansion of monolayer deposition region especially on slower deposition velocity side.

Binary liquid phases of ethyl alcohol and water could lead to the Marangoni flows within convective deposition. Favored evaporation of ethyl alcohol drives surface tension gradients and results in the flow similar to the formation of "tears of wine". Optimum ethyl alcohol concentration for convective deposition is between 30-50 %V where monolayers deposition can take place at deposition velocity roughly 10 times faster than traditional convective deposition.

7.2 Future Outlook

The most significant challenge to researchers in this area is to scale up convective deposition process for industrial applications. Most of current researches in convective deposition use a small batch process (milliliter scale). Suspension stability is one of the major concerns since an agglomeration of colloidal particles will lead to a dramatic decrease in coating quality. In continuous process, a mixing equipment needs to be added to maintain well-dispersed suspension throughout a deposition process. An increase in electrostatic repulsion forces among particles (as discussed in Chapter 4) is another easy approach to improve suspension stability. In aqueous silica suspension, an addition of NaOH can increase particle surface charges resulting in an increase in electrostatic repulsion forces. However, this method cannot apply to other solvents or particle materials such as polystyrene. Furthermore, a life time of deposition blade needed to be evaluated.

Besides, the effect of Marangoni flows on convective deposition is moderately understood. Further investigation at low (less than 20 %V) and high concentration (more than 50 %V) of ethyl alcohol must be carried on. Especially at low concentration, we observed periodic wavelike patterns of deposited particles throughout the whole sample regardless of deposition velocity. To the best of our knowledge, the mechanism of this formation has never been reported. Perhaps studies allowing experimental particle tracking under confocal laser scanning microscopy can give further insight into the formation of these wavelike patterns. Additionally, current study on defect suppression is also necessary. An addition of surfactants can create the surface tension gradient within

the meniscus, resulting in reversal Marangoni flows back into bulk suspension. This study has shown a potential for streaking suppression.

Finally, our developed methods for the fabrication of uniform SiO_2/PS microlens arrays with controllable aspect ratios can be further utilized to create other functionalized colloidal materials such as hydrophobic-hydrophilic Janus particles.

Bibliography

Ackerson, Bruce J. 1990. "Shear Induced Order and Shear Processing of Model Hard Sphere Suspensions." *Journal of Rheology* 34 (4): 553–590.

Ackerson, Bruce J., and Noel A Clark. 1983. "Sheared Colloidal Suspensions." *Physica* 118A: 221–249.

Alvarez, Mar, James R. Friend, and Leslie Y. Yeo. 2008. "Surface Vibration Induced Spatial Ordering of Periodic Polymer Patterns on a Substrate." *Langmuir* 24 (19): 10629–10632.

An, X. Z., and A. B. Yu. 2013. "Analysis of the Forces in Ordered FCC Packings with Different Orientations." *Powder Technology* 248: 121–130.

Baikov, V. I., A. T. Listrov, and Z. A. Shabunina. 1982. "Stability of a Film Flowing down along an Oscillating Surface." *Journal of Engineering Physics* 43 (6): 1413–1418.

Benilov, E. S., and M. Chugunova. 2010. "Waves in Liquid Films on Vibrating Substrates." *Physical Review E - Statistical, Nonlinear, and Soft Matter Physics* 81 (3): 036302.

Bertozzi, Andrea L., and Michael P. Brenner. 1997. "Linear Stability And Transient Growth In Driven Contact Lines." *Physics of Fluids* 9 (3): 530–539.

Besseling, T. H., M. Hermes, A. Fortini, M. Dijkstra, A. Imhof, and A. van Blaaderen. 2012. "Oscillatory Shear-Induced 3D Crystalline Order in Colloidal Hard-Sphere Fluids." *Soft Matter* 8 (26): 6931–6939.

Bestehorn, Michael. 2013. "Laterally Extended Thin Liquid Films with Inertia under External Vibrations." *Physics of Fluids* 25 (11): 114106.

Biancaniello, Paul L., and John C. Crocker. 2006. "Line Optical Tweezers Instrument for Measuring Nanoscale Interactions and Kinetics." *Review of Scientific Instruments* 77 (11): 113702.

Bishop, Kyle J. M., Christopher E. Wilmer, Siowling Soh, and Bartosz A. Grzybowski. 2009. "Nanoscale Forces and Their Uses in Self-Assembly." *Small* 5 (14): 1600–1630.

Blaaderen, Alfons Van, Rene Ruel, and Pierre Wiltzius. 1997. "Template-Directed Colloidal Crystallization." *Nature* 385: 321–324.

Brady, John F., and Georges Bossis. 1985. "The Rheology of Concentrated Suspensions of Spheres in Simple Shear Flow by Numerical Simulation." *Journal of Fluid Mechanics* 155: 105-129.

Brewer, Damien D., Joshua Allen, Michael R. Miller, Juan M. De Santos, Satish Kumar, David J. Norris, Michael Tsapatsis, and L. E. Scriven. 2008. "Mechanistic Principles of Colloidal Crystal Growth by Evaporation-Induced Convective Steering." *Langmuir* 24 (23): 13683–13693.

Brzoska, J. B., N. Shahidzadeh, and F. Rondelez. 1992. "Evidence of a Transition Temperature for the Optimum Deposition of Grafted Monolayer Coatings." *Nature* 360 (6406): 719-721.

Chen, L. B., C. F. Zukoski, B. J. Ackerson, H. J. M. Hanley, G. C. Straty, J. Barker, and C. J. Glinka. 1992. "Structural Changes and Orientational Order in a Sheared Colloidal Suspension." *Physical Review Letters* 69 (4): 688–691.

Chen, L. B., M. K. Chow, B. J. Ackerson, and C. F. Zukoski. 1994. "Rheological and Microstructural Transitions in Colloidal Crystals." *Langmuir* 36 (25): 2817–2829.

Choi, Dae Geun, Hyung Kyun Yu, Se Gyu Jang, and Seung Man Yang. 2004. "Colloidal Lithographic Nanopatterning via Reactive Ion Etching." *Journal of the American Chemical Society* 126 (22): 7019–7025.

Cong, Chunxiao, William Chandra Junus, Zexiang Shen, and Ting Yu. 2009. "New Colloidal Lithographic Nanopatterns Fabricated by Combining Pre-Heating and Reactive Ion Etching." *Nanoscale Research Letters* 4 (11): 1324–1328.

Deegan, R. D., O. Bakajin, T. F. Dupont, G. Huber, S. R. Nagel, and T. A. Witten. 1997. "Capillary Flow as the Cause of Ring Stains from Dried Liquid Drops." *Nature* 389 (6653): 827–829.

Diao, J. J., J. B. Hutchison, Guanghong Luo, and M. E. Reeves. 2005. "Theoretical Analysis of Vertical Colloidal Deposition." *Journal of Chemical Physics* 122 (18): 184710.

Dimitrakopoulos, P., and J. J. L. Higdon. 1997. "Displacement of Fluid Droplets from Solid Surfaces in Low-Reynolds-Number Shear Flows." *Journal of Fluid Mechanics* 336: 351-378.

Dimitrov, Antony S., and Kuniaki Nagayama. 1995. "Steady-State Unidirectional Convective Assembling of Fine Particles into Two-Dimensional Arrays." *Chemical Physics Letters* 243: 462-468.

Dimitrov, Antony S., and Kuniaki Nagayama. 1996. "Continuous Convective Assembling of Fine Particles into Two-Dimensional Arrays on Solid Surfaces." *Langmuir* 12 (5): 1303–1311.

Dozier, W. D., and P. M. Chaikin. 1982. "Periodic Structures in Colloidal Crystals with Oscillatory Flow." *Journal de Physique* 43: 843–51.

Ee, Yik-Khoon, Ronald A. Arif, Nelson Tansu, Pisist Kumnorkaew, and James F. Gilchrist. 2007. "Enhancement of Light Extraction Efficiency of InGaN Quantum Wells Light Emitting Diodes Using SiO_2/polystyrene Microlens Arrays." *Applied Physics Letters* 91 (22): 221107.

Ghosh, Moniraj, Fengqiu Fan, and Kathleen J Stebe. 2007. "Spontaneous Pattern Formation by Dip Coating of Colloidal Suspensions on Homogeneous Surfaces." *Langmuir* 23 (4): 2180–2183.

Gifford, W. A., and L. E. Scriven. 1971. "On the Attraction of Floating Particles." *Chemical Engineering Science* 26 (3): 287–297.

Haes, Amanda J., Christy L. Haynes, and Richard P. Van Duyne. 2001. "Nanosphere Lithography: Self-Assembled Photonic and Magnetic Materials." *MRS Proceedings* 636.

Hamamoto, Yoshinori, John R. E. Christy, and Khellil Sefiane. 2012. "The Flow Characteristics of an Evaporating Ethanol Water Mixture Droplet on a Glass Substrate." *Journal of Thermal Science and Technology* 7 (3): 425–436.

Harris, Daniel J., Hua Hu, Jacinta C. Conrad, and Jennifer A. Lewis. 2007. "Patterning Colloidal Films via Evaporative Lithography." *Physical Review Letters* 98 (14): 148301.

Haw, M. D., W. C. K. Poon, and P. N. Pusey. 1998. "Direct Observation of Oscillatory-Shear-Induced Order in Colloidal Suspensions." *Physical Review E* 57 (6): 6859–6864.

Haynes, Christy L., and Richard P. Van Duyne. 2001. "Nanosphere Lithography: A Versatile Nanofabrication Tool for Studies of Size-Dependent Nanoparticle Optics." *Journal of Physical Chemistry B* 105 (24): 5599–5611.

Hayward, R. C., D. A. Saville, and I. A. Aksay. 2000. "Electrophoretic Assembly of Colloidal Crystals with Optically Tunable Micropatterns." *Nature* 404 (6773): 56–59.

Hoogenboom, J. P., C. Retif, E. de Bres, M. van de Boer, A. K. van Langen-Suurling, J. Romijn, and A. van Blaaderen. 2004. "Template-Induced Growth of Close-Packed and Non-Close-Packed Colloidal Crystals during Solvent Evaporation." *Nano Letters* 4 (2): 205–208.

Hosoi, A. E., and John W. M. Bush. 2001. "Evaporative Instabilities in Climbing Films." *Journal of Fluid Mechanics* 442: 217-239.

Iler, R. K. 1979. *The Chemistry of Silica: Solubility, Polymerization, Colloid and Surface Properties, and Biochemistry. John Wiley & Sons: New York.*

Im, S. H., Y. T. Lim, D. J. Suh, and O. O. Park. 2002. "Three-Dimensional Self-Assembly of Colloids at a Water-Air Interface: A Novel Technique for the Fabrication of Photonic Bandgap Crystals." *Advanced Materials* 14 (19): 1367–1369.

Innocenzi, Plinio, Luca Malfatti, Stefano Costacurta, Tongjit Kidchob, Massimo Piccinini, and Augusto Marcelli. 2008. "Evaporation of Ethanol and Ethanol-Water Mixtures Studied by Time-Resolved Infrared Spectroscopy." *Journal of Physical Chemistry A* 112 (29): 6512–6516.

Ji, Won Yang, In Sim Jae, Myoung An Ho, and Geun Kim Tae. 2011. "Fabrication of Nanometer-Scale Pillar Structures by Using Nanosphere Lithography." *Journal of the Korean Physical Society* 58 (42): 994-997.

Jiang, Peng, and Michael J. McFarland. 2004. "Large-Scale Fabrication of Wafer-Size Colloidal Crystals, Macroporous Polymers and Nanocomposites by Spin-Coating." *Journal of the American Chemical Society* 126 (42): 13778–13786.

Jiang, Peng, and Michael J. McFarland. 2005. "Wafer-Scale Periodic Nanohole Arrays Templated from Two-Dimensional Nonclose-Packed Colloidal Crystals." *Journal of the American Chemical Society* 127 (11): 3710–3711.

Jin, Chongjun, Martyn A. McLachlan, David W. McComb, Richard M. De La Rue, and Nigel P. Johnson. 2005. "Template-Assisted Growth of Nominally Cubic (100)-Oriented Three-Dimensional Crack-Free Photonic Crystals." *Nano Letters* 5 (12): 2646–2650.

Jin, Chongjun, Zhi Yuan Li, Martyn A. McLachlan, David W. McComb, Richard M. De La Rue, and Nigel P. Johnson. 2006. "Optical Properties of Tetragonal Photonic

Crystal Synthesized via Template-Assisted Self-Assembly." *Journal of Applied Physics* 99 (11): 116109.

Kataoka, De, and S. M. Troian. 1997. "A Theoretical Study of Instabilities at the Advancing Front of Thermally Driven Coating Films." *Journal of Colloid and Interface Science* 192 (2): 350–362.

Kazakova, O., M. Hanson, P. Blomqvist, and R. Wäppling. 2004. "Interplay between Shape and Magnetocrystalline Anisotropies in Patterned Bcc Fe/Co(001) Multilayers." *Physical Review B* 69 (9): 094408.

Kershner, Ryan J., Joseph W. Bullard, and Michael J. Cima. 2004. "The Role of Electrochemical Reactions during Electrophoretic Particle Deposition." *Journal of Colloid and Interface Science* 278 (1): 146–154.

Kim, Hyun Suk, Cheol Hee Lee, P. K. Sudeep, Todd Emrick, and Alfred J. Crosby. 2010. "Nanoparticle Stripes, Grids, and Ribbons Produced by Flow Coating." *Advanced Materials* 22 (41): 4600–4604.

Kleinert, Jairus, Sejong Kim, and Orlin D. Velev. 2010. "Electric-Field-Assisted Convective Assembly of Colloidal Crystal Coatings." *Langmuir* 26 (12): 10380–10385.

Koyama, K, N Yamaguchi, and T Miyasaka. 1994. "Antibody-Mediated Bacteriorhodopsin Orientation for Molecular Device Architectures." *Science* 265 (5173): 762–765.

Kralchevsky, Peter a, and Kuniaki Nagayama. 1994. "Capillary Forces between Colloidal Particles." *Langmuir* 10 (1): 23–36.

Kumnorkaew, Pisist, Yik Khoon Ee, Nelson Tansu, and James F. Gilchrist. 2008. "Investigation of the Deposition of Microsphere Monolayers for Fabrication of Microlens Arrays." *Langmuir* 24 (21): 12150–12157.

Kumnorkaew, Pisist, and James F. Gilchrist. 2009. "Effect of Nanoparticle Concentration on the Convective Deposition of Binary Suspensions." *Langmuir* 25 (11): 6070–6075.

Kumnorkaew, Pisist, Alexander L. Weldon, and James F. Gilchrist. 2010. "Matching Constituent Fluxes for Convective Deposition of Binary Suspensions." *Langmuir* 26 (4): 2401–2405.

Lee, Wonmok, Angel Chan, Michael A. Bevan, Jennifer A. Lewis, and Paul V. Braun. 2004. "Nanoparticle-Mediated Epitaxial Assembly of Colloidal Crystals on Patterned Substrates." *Langmuir* 20 (13): 5262–5270.

Li, Wen C., An H. Lu, Claudia Weidenthaler, and Ferdi Schüth. 2004. "Hard-Templating Pathway to Create Mesoporous Magnesium Oxide." *Chemistry of Materials* 16 (26): 5676–5681.

Li, Xiao Hang, Renbo Song, Yik Khoon Ee, Pisist Kumnorkaew, James F. Gilchrist, and Nelson Tansu. 2011. "Light Extraction Efficiency and Radiation Patterns of III-Nitride Light-Emitting Diodes with Colloidal Microlens Arrays with Various Aspect Ratios." *IEEE Photonics Journal* 3 (3): 489–499.

Meng, Linli, Hong Wei, Anthony Nagel, Benjamin J Wiley, L E Scriven, and David J Norris. 2006. "The Role of Thickness Transitions in Convective Assembly." *Nano Letters* 6 (10): 2249–2253.

Min, Younjin, Mustafa Akbulut, Kai Kristiansen, Yuval Golan, and Jacob Israelachvili. 2008. "The Role of Interparticle and External Forces in Nanoparticle Assembly." *Nature Materials* 7 (7): 527–538.

Muangnapoh, Tanyakorn, Alexander L. Weldon, and James F. Gilchrist. 2013. "Enhanced Colloidal Monolayer Assembly via Vibration-Assisted Convective Deposition." *Applied Physics Letters* 103 (18): 181603.

Or, A. C. 1997. "Finite-Wavelength Instability in a Horizontal Liquid Layer on an Oscillating Plane." *Journal of Fluid Mechanics* 335: 213–232.

Panine, P., T. Narayanan, J. Vermant, and J. Mewis. 2002. "Structure and Rheology during Shear-Induced Crystallization of a Latex Suspension." *Physical Review E* 66 (2): 022401.

Park, Sang Hyun, Dong Qin, and Younan Xia. 1998. "Crystallization of Mesoscale Particles over Large Areas." *Advanced Materials* 10 (13): 1028–1032.

Papirer, E. 2002. *Adsorption on Silica Surfaces (Surfactant Science). CRC Press: New York.*

Pawar, Amar B., and Ilona Kretzschmar. 2010. "Fabrication, Assembly, and Application of Patchy Particles." *Macromolecular Rapid Communications* 31 (2): 150–168.

Philp, Douglas, and J. Fraser Stoddart. 1996. "Self-Assembly in Natural and Unnatural Systems." *Angewandte Chemie* 35 (11): 1154–1196.

Pieranski, P., L. Strzelecki, and B. Pansu. 1983. "Thin Colloidal Crystals." *Physical Review Letters* 50 (12): 900–904.

Porter, J., I. Tinao, A. Laverón-Simavilla, and C. A. Lopez. 2012. "Pattern Selection in a Horizontally Vibrated Container." *Fluid Dynamics Research* 44 (6): 065501.

Prevo, Brian G., and Orlin D. Velev. 2004. "Controlled, Rapid Deposition of Structured Coatings from Micro- and Nanoparticle Suspensions." *Langmuir* 20 (6): 2099–2107.

Pusey, P. N, and W. van Megen. 1986. "Phase Behaviour of Concentrated Suspensions of Nearly Hard Colloidal Spheres." *Nature* 320: 340–342.

Rödner, Sandra C., Pär Wedin, and Lennart Bergström. 2002. "Effect of Electrolyte and Evaporation Rate on the Structural Features of Dried Silica Monolayer Films." *Langmuir* 18 (24): 9327–9333.

Rudenko, O. V., a. I. Korobov, B. a. Korshak, P. V. Lebedev-Stepanov, S. P. Molchanov, and M. V. Alfimov. 2010. "Self-Assembly of Colloidal-Particle Ensembles in an Acoustic Field." *Nanotechnologies in Russia* 5 (7-8): 469–473.

Ruhl, T., P. Spahn, and G.P. Hellmann. 2003. "Artificial Opals Prepared by Melt Compression." *Polymer* 44 (25): 7625–7634.

Sawada, Tsutomu, Yoshihisa Suzuki, Akiko Toyotama, and Nobuo Iyi. 2001. "Quick Fabrication of Gigantic Single-Crystalline Colloidal Crystals for Photonic Applications." *Japan Journal of Applied Physics* 40: L1226–28.

Sharma, Ashutosh. 1993. "Relationship of Thin Film Stability and Morphology to Macroscopic Parameters of Wetting in the Apolar and Polar Systems." *Langmuir* 28 (23): 861–869.

Sharma, Ashutosh. 1998. "Stability and Breakup of Thin Evaporating Water Films: Role of Hydrophobic Interaction." *Journal of Colloid and Interface Science* 199 (2): 212–214.

Shereda, Laura T., Ronald G. Larson, and Michael J. Solomon. 2010. "Boundary-Driven Colloidal Crystallization in Simple Shear Flow." *Physical Review Letters* 105 (22): 228302.

Shimmin, Robert G., Alexander J. DiMauro, and Paul V. Braun. 2006. "Slow Vertical Deposition of Colloidal Crystals: A Langmuir-Blodgett Process?" *Langmuir* 22 (15): 6507–6513.

Shklyaev, S., A. A. Alabuzhev, and M. Khenner. 2009. "Influence of a Longitudinal and Tilted Vibration on Stability and Dewetting of a Liquid Film." *Physical Review E - Statistical, Nonlinear, and Soft Matter Physics* 79 (5): 051603.

Sirota, E. B., H. D. Ou-Yang, S. K. Sinha, and P. M. Chaikin. 1989. "Complete Phase Diagram of a Charged Colloidal System: A Synchrotron X-Ray Scattering Study." *Physical Review Letters* 62 (13): 1524–1527.

Smoukov, Stoyan K., Sumit Gangwal, Manuel Marquez, and Orlin D. Velev. 2009. "Reconfigurable Responsive Structures Assembled from Magnetic Janus Particles." *Soft Matter* 5: 1285–1292.

Stancik, Edward J., Anne L. Hawkinson, Jan Vermant, and Gerald G. Fuller. 2004. "Dynamic Transitions and Oscillatory Melting of a Two-Dimensional Crystal Subjected to Shear Flow." *Journal of Rheology* 48 (1): 159–173.

Stebe, Kathleen J, Eric Lewandowski, and Moniraj Ghosh. 2009. "Oriented Assembly of Metamaterials." *Science* 325 (5937): 159–60.

Sun, Shouheng, C.B. Murray, Dieter Weller, Liesl Folks, and Andreas Moser. 2000. "Monodisperse FePt Nanoparticles and Ferromagnetic FePt Nanocrystal Superlattices." *Science* 287: 1989–1992.

Tanaka, Manabu, Naonobu Shimamoto, Takashi Tanii, Iwao Ohdomari, and Hiroyuki Nishide. 2006. "Packing of Submicrometer-Sized Polystyrene Particles within the Micrometer-Sized Recessed Patterns on Silicon Substrate." *Science and Technology of Advanced Materials* 7 (5): 451–455.

Tessier, P. M., O. D. Velev, A. T. Kalambur, A. M. Lenhoff, J. F. Rabolt, and E. W. Kaler. 2001. "Structured Metallic Films for Optical and Spectroscopic Applications via Colloidal Crystal Templating." *Advanced Materials* 13 (6): 396–400.

Tessier, Peter M., Orlin D. Velev, Anand T. Kalambur, John F. Rabolt, Abraham M. Lenhoff, and Eric W. Kaler. 2000. "Assembly of Gold Nanostructured Films Templated by Colloidal Crystals and Use in Surface-Enhanced Raman Spectroscopy_Supporting Information." *J. Am. Chem. Soc.* 122: 9554–9555.

Thomson, J. 1855. "On Certain Curious Motions Observable at the Surfaces of Wine and Other Alcoholic Liquors." *The London, Edinburgh and Dublin Philosophical Magazine and Journal of Science* 10: 330.

Troian, S. M., X. L. Wu, and S. A. Safran. 1989. "Fingering Instability in Thin Wetting Films." *Physical Review Letters* 62 (13): 1496-1499.

Van Blaaderen, Alfons, Jacob P. Hoogenboom, Dirk L. J. Vossen, Anand Yethiraj, Astrid van der Horst, Koen Visscher, and Marileen Dogterom. 2003. "Colloidal Epitaxy: Playing with the Boundary Conditions of Colloidal Crystallization." *Faraday Discussions* 123: 107–119.

Velev, O. D., and E. W. Kaler. 1999. "In Situ Assembly of Colloidal Particles into Miniaturized Biosensors." *Langmuir* 15 (11): 3693–3698.

Vella, Dominic, and L. Mahadevan. 2005. "The 'Cheerios Effect." *American Journal of Physics* 73: 817–825.

Vlasov, Yurii A., Xiang Zheng Bo, James C. Sturm, and David J. Norris. 2001. "On-Chip Natural Assembly of Silicon Photonic Bandgap Crystals." *Nature* 414: 289–293.

Wang, Bu, Alex L. Weldon, Pisist Kumnorkaew, Bu Xu, James F. Gilchrist, and Xuanhong Cheng. 2011. "Effect of Surface Nanotopography on Immunoaffinity Cell Capture in Microfluidic Devices." *Langmuir* 27 (17): 11229–11237.

Wei, Q.-H., D. M. Cupid, and X. L. Wu. 2000. "Controlled Assembly of Two-Dimensional Colloidal Crystals." *Applied Physics Letters* 77 (11): 1641-1643.

Weldon, Alexander L., Pisist Kumnorkaew, Bu Wang, Xuanhong Cheng, and James F. Gilchrist. 2012. "Fabrication of Macroporous Polymeric Membranes through Binary Convective Deposition." *ACS Applied Materials and Interfaces* 4 (9): 4532–4540.

Whitesides, George M., and Bartosz Grzybowski. 2002. "Self-Assembly at All Scales." *Science* 295 (5564): 2418–2421.

Woodcock, L.V. 1997. "Entropy Difference between the Face-Centred Cubic and Hexagonal Close-Packed Crystal Structures." *Nature* 385: 141–143.

Yamaki, Mariko, Junichi Higo, and Kuniaki Nagayama. 1995. "Size-Dependent Separation of Colloidal Particles In Two-Dimensional Convective Self-Assembly." *Langmuir* 11 (8): 2975–2978.

Yang, Zhengwen, Xueguang Huang, Sun Li, and Ji Zhou. 2009. "Photonic Bandgap and Photoluminescence in TbPO4 Inverse Opal with Coexistence of the (001) and (111) Orientations." *Journal of the American Ceramic Society* 92 (7): 1596–1598.

Yi, Dong Kee, Min Jun Kim, Linda Turner, Kenneth S. Breuer, and Dong Y. Kim. 2006. "Colloid Lithography-Induced Polydimethylsiloxane Microstructures and Their Application to Cell Patterning." *Biotechnology Letters* 28 (3): 169–173.

Yi, Dong Kee, Eun Mi Seo, and Dong Yu Kim. 2002. "Surface-Modulation-Controlled Three-Dimensional Colloidal Crystals." *Applied Physics Letters* 80 (2): 225–227.

Yih, Chia-Shun. 1968. "Instability of a Horizontal Layer of Viscoelastic Liquid on an Oscillating Plane." *Journal of Fluid Mechanics* 31 (4): 737–751.

Yin, Yadong, Zhi Yuan Li, and Younan Xia. 2003. "Template-Directed Growth of (100) -Oriented Colloidal Crystals." *Langmuir* 19 (100): 622–631.

Zeng, H. 2013. *Polymer Adhesion, Friction, and Lubrication. John Wiley & Sons: New Jersey*.

Zhang, J., A. Alsayed, K. H. Lin, S. Sanyal, F. Zhang, W.-J. Pao, V. S. K. Balagurusamy, P. A. Heiney, and A. G. Yodh. 2002. "Template-Directed Convective Assembly of Three-Dimensional Face-Centered-Cubic Colloidal Crystals." *Applied Physics Letters* 81 (17): 3176–3178.

Zhang, Yongjun, Shaopeng Wang, Mohammad Eghtedari, Massoud Motamedi, and Nicholas A. Kotov. 2005. "Inverted-Colloidal-Crystal Hydrogel Matrices as Three-Dimensional Cell Scaffolds." *Advanced Functional Materials* 15 (5): 725–731.

Zhang, Yongjun, Xianghe Wang, Yaxin Wang, Huilian Liu, and Jinghai Yang. 2008. "Ordered Nanostructures Array Fabricated by Nanosphere Lithography." *Journal of Alloys and Compounds* 452: 473–477.

Curriculum Vitae

Tanyakorn Muangnapoh

A. Biographical Information

Personal Details

Tanyakorn Muangnapoh

Department of Chemical and Biomolecular Engineering, Lehigh University

111 Research Drive, Iacocca Hall Bethlehem, PA 18015

E-mail: tam309@lehigh.edu, tmuangnapoh@gmail.com

Mobile: (+1) 610-393-0496

Education

2009 - Present

Doctor of Philosophy (Ph.D.) in Chemical Engineering

Department of Chemical and Biomolecular Engineering, Lehigh University, Pennsylvania, USA

Thesis: Convective Assembly of Colloidal Monolayers: Mechanical and Chemical Approaches

Advisor: Assoc. Prof. James F Gilchrist

2005 - 2008

Master of Engineering (M.Eng.) in Chemical Engineering

Department of Chemical Engineering, Faculty of Engineering, Chulalongkorn University, Bangkok, Thailand

Thesis: Synthesis of Gold Nanoparticles using pH Control and Ultrasonication

Advisor: Assoc. Prof. Tawatchai Charinpanitkul

2001 - 2005

Bachelor of Engineering (B.Eng.) in Chemical Engineering

Department of Chemical Engineering, Faculty of Engineering, Chulalongkorn University, Bangkok, Thailand

<u>Senior Project</u>: Improvement of Large-Scaled Recycling of Glass Fiber-Reinforced Plastic Sheets

Advisor: Assoc. Prof. Tawatchai Charinpanitkul

The project was collaborated with Siam Fiberglass Company Limited

Research Experience and Employment

2013-Present

Research Assistant in Department of Chemical Engineering, Lehigh University,

Pennsylvania, USA

Mentor: Assoc. Prof. James F Gilchrist

2008 - 2009

Research Assistant at Center of Excellence in Particle Technology, Faculty of Engineering,

Chulalongkorn University

Mentor: Assoc. Prof. Tawatchai Charinpanitkul

March 2004

Internship Program at PTT Public Company Limited, Thailand

Mentor: Dr. Wit Soontaranun

B. Publications and Presentations

Refereed Articles

4) K. Joshi*, <u>T. Muangnapoh</u>*, M. Stever, and J. F. Gilchrist, "Effect of ionic strength and surface charge on convective deposition," to be submitted (*co-first author)

3) M. Joy, <u>T. Muangnapoh</u>, M.A. Snyders, and J. F. Gilchrist, "Template-free fabrication of partially aligned (100) fcc thin film colloidal crystals," to be submitted

2) <u>T. Muangnapoh</u>, A. L.Weldon, and J. F. Gilchrist, "Enhanced colloidal monolayer assembly via vibration-assisted convective deposition," Applied Physics Letters 103 (2013), 181603.

1) <u>T. Muangnapoh</u>, N. Sano, S.I. Yusa, N. Viriya-Empikul, and T. Charinpanitkul, "Facile strategy for stability control of gold nanoparticles synthesized by aqueous reduction method," Current Applied Physics 10 (2010), 708-714.

<u>Contributed conference presentations</u>

12) <u>M. Joy</u>, T. Muangnapoh, M.A. Snyders, and J. F. Gilchrist, "Non-templated fabrication of partially aligned BCC thin film colloidal crystals," The Society of Rheology 86th Annual Meeting, October 2014, Philadelphia, Pennsylvania, USA

11) <u>T. Muangnapoh</u>, A. L.Weldon, M. Joy, and J. F. Gilchrist, "Vibration-Assisted Convective Deposition," The 88th ACS Colloid and Surface Science Symposium, June 2014, Philadelphia, Pennsylvania, USA

10) <u>T. Muangnapoh</u>, A. L.Weldon, P.Kumnorkaew, and J. F. Gilchrist, "Effect of lateral vibrations during convective deposition," American Physical Society Division of Fluid Dynamics, November 2013, Pittsburg, Pennsylvania, USA

9) <u>J. F. Gilchrist</u>, T. Muangnapoh, and A. L.Weldon, "Vibration-assisted convective assembly and deposition for monolayer particle coatings from suspension," Society of Rheology 84th Annual Meeting, February 2013, Pasadena, California, USA

8) A. Weldon, T. Muangnapoh, P. Kumnorkaew, and <u>J. F. Gilchrist</u>, "Convective Assembly for Nanostructured Optical and Biofunctional Coatings," 16th International Coating Science and Technology Symposium, September 2012, Ventura, Canada

7) <u>A. L.Weldon</u>, T. Muangnapoh, P.Kumnorkaew, and J. F. Gilchrist, "Capillary-Driven Convective Assembly of Colloidal Monolayers," American Physical Society Division of Fluid Dynamics, November 2011, Baltimore, Maryland, USA

6) <u>T. Muangnapoh</u>, A. L.Weldon, P.Kumnorkaew, and J. F. Gilchrist, "Vibration-Assisted Convective Deposition," American Physical Society Division of Fluid Dynamics, November 2011, Baltimore, Maryland, USA

5) T. Muangnapoh, A. L.Weldon, P.Kumnorkaew, and <u>J. F. Gilchrist</u>, "Assisted Convective Assembly of Colloidal Monolayers," American Institute of Chemical Engineers Annual Meeting, November 2011, Minneapolis, Minnesota, USA

4) A. L.Weldon, T. Muangnapoh, and J. F. Gilchrist, "Capillary-driven convective assembly of colloidal monolayers," The Society of Rheology 83rd Annual Meeting, October 2011, Cleveland, Ohio, USA

3) T. Muangnapoh, N. Viriya-empikul, T. Charinpanitkul, and N. Sano, "Size-controllable synthesis of gold nanoparticles by wet chemistry," Thailand Research Fund-Master Research Grants Congress II, April 2008, Pattaya, Thailand.

2) T. Muangnapoh, N. Viriya-empikul, T. Charinpanitkul, and N. Sano, "Effect of pH on stability of gold nanoparticles synthesized by aqueous reaction," Regional Symposium on Chemical Engineering (RSCE 2007), December 2007, Yogyakarta, Indonesia.

1) T. Charinpanitkul, T. Muangnapoh, N. Viriya-empikul, and N. Sano, "Stability control of gold nanoparticles synthesized by wet chemistry," The 5th Eco-Energy and Materials Science and Engineering Symposium (5th EMSES), November 2007, Pattaya, Thailand.

C. Honors and Awards

2008 - 2013

Full scholarship from Royal Thai Government scholarship for pursuing a Doctoral Degree in chemical engineering, concentrating in the field of nanotechnology

April 2008

Awarded "the Most Outstanding Presentation", at the 13th Research Progress Meeting, held by Center of Excellence in Particle Technology (CEPT),

2006 - 2007

Hyogo University Mobility in Asia and the Pacific Scholarship (HUMAP) for one year research experience in Hyogo University, Japan

March 2006

Awarded "the Most Outstanding Presentation", at the 9th Research Progress Meeting, held by Center of Excellence in Particle Technology (CEPT)

2005 - 2008

Full scholarship under Thailand Research Fund-Master Research Grants co-funding (TRF-MAG co-funding) program from Ministry of University Affairs, Thailand Research Fund and Chulalongkorn University

D. Extra-Curricular Activities

2014 - 2015

Graduate student advisor of Thai Student Association at Lehigh University

2013 - 2014

Treasurer of Chemical Engineering Graduate Student Association (ChEGA) at Lehigh University

2011 - 2012

President of Thai Student Association at Lehigh University

2010 - 2011

Vice President of Thai Student Association at Lehigh University

2004 - 2008

A member of Chemical Engineering's soccer team at Chulalongkorn University

2001- 2005

A member of Voluntary Chulalongkorn University Students Club

    - Teaching elementary course work for disabled people in Bangkok, Thailand

    - Constructing bridges for underprivileged people in rural areas of Thailand